Delft University of Technology

Instruments for seismic isolation

Improving performance of advanced displacement and inertial sensors for active suppression of seismic noise in Gravitational Wave detectors

P.N.G. de Gaay Fortman

TU Delft

Instruments for seismic isolation

Improving performance of advanced displacement and inertial sensors for active suppression of seismic noise in Gravitational Wave detectors

by

P.N.G. de Gaay Fortman

to obtain the degree of Master of Science
at the Delft University of Technology,
to be defended publicly on Tuesday November 1, 2019 at 11:00 AM.

Student number:	4736524	
Project duration:	September 1, 2018 – November 1, 2019	
Thesis committee:	Prof. dr. H. van der Graaf,	Nikhef and TU Delft, supervisor
	Dr. A. Bertolini,	Nikhef, supervisor
	Prof. dr. S. Stallinga,	TU Delft
	Dr. C. W. Hagen,	TU Delft
	Dr. B. Swinkels,	Nikhef

This thesis is confidential and cannot be made public until November 1, 2019.

TU Delft

Preface

Thankful for two inspiring and supportive mentors at Nikhef, Harry and Alessandro, from whom I have received a humbling amount of patient and enthusiastic guidance. Thankful for theoretical assistance from Eric, and experimental help from Boris. Lastly, thankful for general guidance from overseas from Joris, who introduced me to the fascinating subject of Gravitational Waves physics.

P.N.G. de Gaay Fortman
Amsterdam, October 2019

Abstract

Laser interferometric Gravitational Wave telescopes are limited in sensitivity by seismic noise in the low frequency region (below a 10 Hz). The aim of this research is to improve performance of an advanced displacement sensor and an ultra-low noise inertial sensor, that can help measuring and correcting for seismically induced motion of the GW detetctor's test masses.

In a Rasnik, light from a back-illuminated encoded ChessField mask is projected onto a pixel image sensor, and the relative position is tracked between mask and sensor. In past experiments, Rasnik was modelled to have resolution of below ~0.5 nm in X and Y, while RMS resolutions of ~25 nm were measured [1], a longstanding discrepancy central to this research. It was found that, analyzing spectral information of Rasnik response data, Rasnik did in fact reach its sub-nm modelled noise floor. A resolution floor of $A_n = 270$ pm/$\sqrt{\mathrm{Hz}}$ was measured, shown to be limited by SNR of the pixel content and white noise aliasing. What is more, with a different setup, an optical magnification trick was shown to result in RMS resolution gain.

For the forced-feedback accelerometer with interferometric readout, Heijningen [2] measured displacement sensitivities of up to 8 fm/$\sqrt{\mathrm{Hz}}$ above 30 Hz, while the instrument was modelled to be shot noise limited at 3 fm/$\sqrt{\mathrm{Hz}}$ - another discrepancy this research attempted to explain. A significant reduction of the thermal noise of the instrument's mechanics was achieved by re-designing the feedback actuator. After that, the accelerometer's performance was re-evaluated on a ultra-low vibration platform. A resolution of 50 fm/$\sqrt{\mathrm{Hz}}$ was measured, a factor 30 above the modelled shot noise. Sub-optimal relative intensity fluctuations in the laser, as well as laser frequency noise, were found to be responsible.

Contents

1

Introduction

Gravity is everywhere. Of the four fundamental physical forces, gravity is the most familiar and commonplace to people, but it is also the least understood. It is the weakest force of the four fundamental forces, but it is the driving force empowering the most luminous and extreme astronomical phenomena in our Universe. For humans, it enables so many minor activities of daily life that we are accustomed to its presence. Not many people have asked themselves why apples fall from trees, or why we cannot make a distinction between force from gravitational charge and from an accelerating frame. The ones who questioned these matters, entered a remarkably fundamental domain. Asking yourself what gravity is, will eventually lead you to addressing yourself rather philosophical questions. What is mass, and what are space and time in which the mass exists?

In 1687, Sir Isaac Newton published a book called The Mathematical Principles of Philosophy, better known as Principia, describing three laws of motion and a law of universal gravitation [3] . With his laws he verified Kepler's observations of elliptical planetary orbits (except for Mercury's orbits), and lay the foundation for the intuitive, still widely used classical Newtonian mechanics. Newton related force to acceleration and mass to gravitational charge, which he described to be instantaneous. Newton was awed by the equivalence of inertial mass and gravitational weight, but he could not explain it.

More than two hundred years later, these matters received Albert Einstein's attention. Based on the famous results of the first interferometer experiment by Michelson and Morley in 1887 - stating that light travels with the same velocity with respect to any moving observer [4] - Einstein wrote the Special Theory of Relativity, in which he concluded that space and time are intertwined [5]. After 10 years of hard effort, Einstein was able to include the presence of gravity into his theory, published in a set of papers in 1915-1918, coined the General Theory of Relativity (GR). In his theory, Einstein stated that the gravitational field of a massive body is actually defined by the curvature of the space-time metric around it. Other objects close to this body will move along the curved geodesics of space-time, see Figure 1.1. Movement along bend curvature results in what we observe as gravitational acceleration.

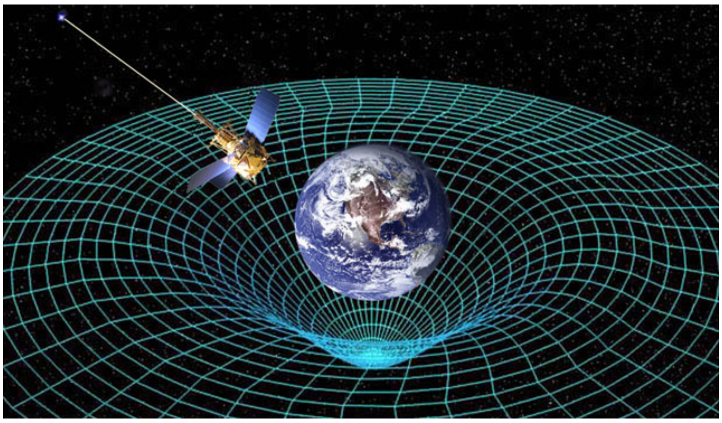

Figure 1.1: Mass bodies define their surrounding space-time geometry. Objects close to this body will follow the curvatures, experienced as gravitational acceleration. Credit: NASA.

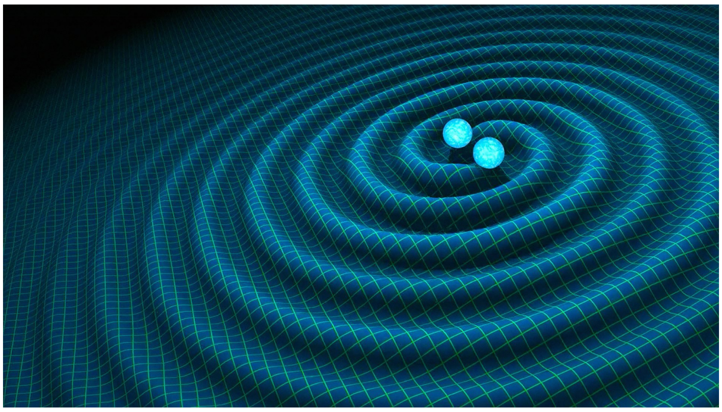

Figure 1.2: Two coalescing neutron stars, emitting GW radiation as ripples through space-time. Credit: R. Hurt/Caltech-JPL.

In this picture, Einstein explained the equivalence principle of inertial and gravitational force.

An astonishing conclusion of GR is that changes in space-time curvature resolve through the vacuum metric at the speed of light. Regarding this finding, Einstein stated that disruptions in the space-time metric should involve Gravitational Waves (GWs) emitted from the source of the disruption and he derived the wave equations describing their behaviour [6, 7]. GWs traverse the vacuum space-time metric like ripples, at the speed of light, thus closely resembling electromagnetic radiation. Their propagation through space-time is depicted in Figure 1.2 Their amplitudes of deforming the space-time metric were determined to be extremely small, and even GWs from the most intense astronomical events were expected to cause relative length changes in the order of $h \sim 10^{-23}$ [2]. Where h is called *strain*, the dimensionless amplitude for relative length changes induced by a GW.

The General Theory of Relativity was tested by Einstein himself in 1915, by accurately forecasting Mercury's deviating ellipses [8], and, more convincingly, by Sir Arthur Eddington in 1919, who showed that light rays followed a space-time curvature around an eclipsed sun [9]. However, at the time, Gravitational Waves remained a rather theoretical conjecture of GR. For a long period, Einstein even assumed that GWs were merely mathematical construct without physical meaning [10]. In the end, Einstein became convinced of the existence of GWs, but he still doubted that mankind would ever be able to create an instrument sensitive enough to measure them.

This challenge was first seriously accepted by Joseph Weber in the 1960s. Weber constructed multiple two meters long, half a meter in diameter, aluminum antennae. GWs with frequencies close to the longitudinal resonance frequency of the bars should harmonically excite them, and Weber assumed he could measure GW induced longitudinal changes with piezoelectric crystals [11]. In 1969, Weber said he detected GWs [12], sparking international interest and GW-enthusiasm. However, his results could not be verified by other scientists. Until 2009, improvements were made to the resonant antennae, leading to maximal strain sensitivities of below $h = 10^{-20}$ at $f = 850$ - 950 Hz [13]. Ultimately, the resonant bars never detected a Gravitational Wave and this endeavour was dropped.

The setback of the non-repeatability of Weber's experiment did not stop GW experimentalists to continue their efforts to find a GW. In the 1970s Rainier Weiss developed a method to measure GWs with a km arm interferometer, based on the conceptual framework of Felix Pirani, published in 1956 [10]. Weiss proposed that if the arms of an interferometer were sufficiently long, the space-time deformation of a passing GW would create enough strain h to cause a detectable change in the interference pattern. This method drew support from the community as a new promising approach to find GWs.

Based on Weiss' interferometer method, Weiss, together with theoretical physicist Kip Thorne and experimentalist Ron Drever (and in a later stadium Barry Barish), founded the US collaboration that completed the two LIGO detectors. In parallel, a French-Italian collaboration completed the Virgo detector in 2003 in Italy, and a British-German collaboration created GEO600, a R&D inclined GW observatory in Germany completed in 2002 [10]. In the meantime, prototype detectors in Japan, such as TAMA300 and CLIO, proved the feasibility of the first underground and cryogenically operated GW detector called KAGRA, which is expected to be in operation as of late 2019 [14]. Plans for third generation GW observatories, underground or even in space, are at advanced stages.

On 14 September 2015, after decades of persistent work, the GW communities' efforts were rewarded with a double observation of the two LIGO detectors. The detectors had observed the merging of two black holes. Consequently, Weiss, Thorne and Barish were awarded the Nobel prize for physics in 2016. Many observations have been made since, by both LIGO and Virgo, opening up a complete new window onto the Universe. Together with optical and neutrino telescopes, scientists are now able to observe (the same) astrophysical events through three different channels - this is called *multi-messenger astronomy*.

Immense scientific projects, such as the second generation telescopes LIGO, Virgo and KAGRA as well as the third generation telescopes that are yet to be build, can be justified by the contributions to physics they provide. With the GW strain sensitivities increasing with each new detector, and expansion of the observable spectrum, insights for theoretical physics, cosmology and astrophysics are gained based on their observations [15]. GWs contain a signature of information about the source that has created them, as well as the nature of the local space-time geometry of a source. It provides valuable insights on how mass and geometry behave in extreme conditions. Amaro-Seoane et al. [16] listed the following contributions for fundamental physics, astrophysics and cosmology.

For fundamental physics, GWs can test different theories of gravity that compete with that of Einstein. Moreover, (not yet observed) GWs emitted from black holes would tell us how gravity behaves at extreme circumstances. GWs might even contribute to string-theory, which expects that GWs traverse a different set of dimensions than the four-dimensional Universe that we perceive.

With electromagnetic (EM) telescopes, astrophysics has revealed the existence of supernovae (imploding-exploding giant starts), gamma-ray bursts (short-lived and extremely powerful gamma energy emitters) and radio pulsars (extremely dense objects rotating at radio frequency). These phenomena are believed to be situated in high gravity environments, and could possibly emit GWs besides the already measurable EM radiation. Multi-messenger astronomy could reveal mechanisms behind these processes.

EM telescopes can only see as far as to about 380,000 years after the Big Bang, when light was able to escape the extremely hot and dense environment. Optical telescopes cannot look back further into that Primordial Universe. However, as gravity existed in that period, third generation GW observatories might reveal a sort of stochastic background signal (much like the Cosmic Microwave Background) that contains information about the Primordial Universe. Another contribution to cosmology will be the use of compact binary GWs as standard candles: objects whose distance can be accurately retrieved from their luminosity. These GW candles, complemented with EM measurements, can be used to fit cosmological population models, from which it will, for instance, be possible to calculate dark matter and dark energy densities.

The above-mentioned are processes that scientists anticipated GWs would improve our understanding of. However, just as EM telescopes unravelled phenomena unimagined at the time, GW observations might reveal exotic processes in our Universe that no one could have ever conceived.

This thesis describes research performed on two sensor instruments that could be used in upgrades of second generation and in ground-based third generation GW observatories. They measure ground-induced acceleration or relative position and can be used to create feedback signals to reduce the motion of suspended parts of the interferometer detectors.

This chapter outlines the principles of Gravitational Waves and GW telescopes, in Sections 1.1 and 1.2. In Section 1.3 the relevance of the instruments for the low frequency band of GW interferometers is discussed. Research on both instruments is described in Chapter 2 (the relative position sensor) and Chapter 3 (the accelerometer). General conclusions are written in Chapter 4.

1.1. Gravitational waves

1.1.1. GR and the space-time perturbation

The GW derivations of this section are based on Einstein's famous 1918 article On Gravitational Waves [7]. From Einstein's Special Theory of Relativity the space-time distance ds between two arbitrary points is given as:

$$ds^2 = \eta_{\mu\nu} dx^\mu dx^\nu \tag{1.1}$$

The sub and superscripts on the right-hand side are shorthand vector representations from Einstein's summation convention, introduced to physics for notational brevity by Einstein, in 1916 [17]. The (x,y,z,t) coordinates are contained in the dx terms and $\eta_{\mu\nu}$ denotes the Minkowski Cartesian *flat* space-time metric:

$$\eta_{\mu\nu} = \begin{pmatrix} -1 & 0 & 0 & 0 \\ 0 & 1 & 0 & 0 \\ 0 & 0 & 1 & 0 \\ 0 & 0 & 0 & 1 \end{pmatrix} \tag{1.2}$$

To generalize Equation 1.1 to GR, the flat Minkowski space must be replaced by a matrix that contains curvature information, representing gravitation in space-time:

$$ds^2 = g_{\mu\nu} dx^\mu dx^\nu \tag{1.3}$$

All space-time geodesics are concealed in the $g_{\mu\nu}$ metric. According to GR, mass, energy and space-time curvature are related to each other via ten coupled and non-linear differential equations, the Einstein Field Equations (EFE).

$$G_{\mu\nu} = R_{\mu\nu} - \frac{1}{2} g_{\mu\nu} R = \frac{8\pi G}{c^4} T_{\mu\nu} \tag{1.4}$$

$G_{\mu\nu}$ is the Einstein tensor, containing space-time information. $R_{\mu\nu}$ is the Ricci curvature tensor and R is the Ricci scalar curvature, both describing metric contractions. G is Newton's gravitational constant, and $T_{\mu\nu}$ is the stress-energy tensor, containing mass, energy and momentum information of the source.

The EFE simplify to linear differential equations when only a minor linear perturbation to the Minkovski metric $\eta_{\mu\nu}$ of $g_{\mu\nu}$ is regarded:

$$g_{\mu\nu} = \eta_{\mu\nu} + \epsilon h_{\mu\nu} \tag{1.5}$$

And from a transverse traceless (TT) transformation, which defines the coordinates of Equation 1.4 by world lines of free-falling test masses [18], the EFE simplify to the form [2]:

$$\frac{8\pi G}{c^4} T_{\mu\nu} = -\frac{1}{2} \epsilon \Box h_{\mu\nu}^{TT} \tag{1.6}$$

with $\Box$ the Four space d'Alembertian operator, defined as:

$$\Box \equiv \frac{-1}{c^2} \frac{\partial^2}{\partial t^2} + \frac{\partial^2}{\partial x^i \partial x_i} \tag{1.7}$$

Far away from the source the stress-energy tensor $T_{\mu\nu}$ vanishes, and a three dimensional wave equation remains:

$$\left(\frac{-1}{c^2} \frac{\partial^2}{\partial t^2} + \frac{\partial^2}{\partial x^i \partial x_i} \right) h_{\mu\nu}^{TT} = 0 \tag{1.8}$$

the perturbation tensor $h_{\mu\nu}^{TT}$ can be expressed as a combination of two planar waves in x and y, if the wave is travelling in z. The two polarizations are expressed as:

$$h_{\mu\nu}^{TT}(t) = h_{+}^{TT}(t - z/c) + h_{\times}^{TT}(t - z/c) \tag{1.9}$$

Where the wave forms are contained in the orthogonal 4×4 matrices:

$$h_{+}^{TT} = \begin{pmatrix} 0 & 0 & 0 & 0 \\ 0 & h_{11} & 0 & 0 \\ 0 & 0 & -h_{11} & 0 \\ 0 & 0 & 0 & 0 \end{pmatrix} \qquad h_{\times}^{TT} = \begin{pmatrix} 0 & 0 & 0 & 0 \\ 0 & 0 & -h_{12} & 0 \\ 0 & h_{12} & 0 & 0 \\ 0 & 0 & 0 & 0 \end{pmatrix} \tag{1.10}$$

Their propagation through space-time are schematically depicted in Figure 1.3. The linear waveform perturbation $h_{\mu\nu}$ is called $strain$, and, for some astronomical sources, it can be measured by GW telescopes. The strain measurement contains signature information about the astronomical source that created the GW, such as distance, location, frequency and energy. The principles of measuring $h_{\mu\nu}$ are explained in short in Section 1.2.

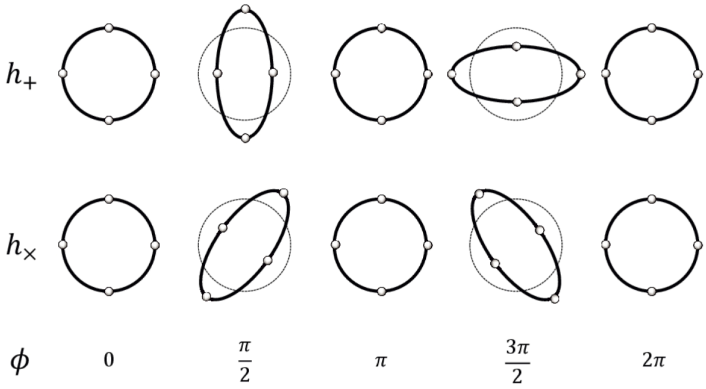

Figure 1.3: A passing GW travelling orthogonal to the plane displaces the four white points in space in two polarities, oriented at 45° with respect to each other. From [19].

1.1.2. Astronomical sources of Gravitational Waves

From a multipolar expansion of the stress-energy tensor $T_{\mu\nu}$, the way in which astrophysical sources generate a GW strain is described by [20]:

$$h_{jk}^{TT} = 2\frac{G}{rc^4}\ddot{Q}_{jk} \tag{1.11}$$

Gravitational waves are thus created from $\ddot{Q}_{jk}$, the second derivative of the gravitational quadrupole moment of an object. The distance from the source is denoted r. Different GW sources emit at different strain amplitudes at varying frequencies, see Figure 1.4. Currently, physicists maintain that there are four main sources that emit gravitational radiation: compact binaries, continuous wave sources, stochastic background radiation and core-collapse supernovae [16].

Compact binary coalescences Blackhole-blackhole (BH-BH), blackhole-neutron star (BH-NS) and neutron star-neutron star (NS-NS) inspirals and mergers are labelled *compact binary coalescences*. From the GW signature of a compact binary coalescence, the mass of a NS and the mass and spin of a BH can be derived [15]. From this, for instance the maximum mass of a NS could be derived and its equation-of-state constrained, an unresolved problem in theoretical physics [15, 16]. The distance range of observing compact binary coalescences increases with improved strain sensitivities of GW observatories.

A GW amplitude is determined from the ratio of a certain combination of binary masses and the luminosity distance. As chirp signals from NS-NS inspirals have measurable amplitudes of signals and masses, their precise luminosity distances can be inferred [16]. These luminosity distances could be utilized as standard candles, which are of importance for testing cosmological models [15].

From a GW signal, the redshift of a source cannot be determined, but with complementary information from optical telescopes, high-precision multi-messenger astronomy becomes possible. From this, coalescence rates as a function of redshift could be constructed, revealing knowledge on the history of cosmic compact object formation history [16]. What is more, star metallacity and massive stars evolutions can be constructed from multi-messenger astronomy [16].

Continuous wave sources Continuous sources typically last for a few weeks or years, have constant amplitude and slowly varying frequency. For instance, rapidly rotating non-axisymmetric neutron stars, either isolated (pulsars) or in binary systems, emit continuous GWs. Measuring at a certain strain sensitivity, spindown GW energy limits of pulsars can be derived [16].

Stochastic background Stochastic background GW radiation can be detected by the cross-correlation of at least two GW telescopes [16]. The stochastic background radiation can have two origins: cosmological and astrophysical. The cosmological background would be a relic of gravitational processes in the early Universe, but that could be masked by the astrophysical background radiation, produced by the forming of galaxies and stars (from binary NS, rotating NS with quadrupole moments and core-collapse supernovae). Detection of astrophysical background radiation would put constraint on physical properties of compact objects and redshift evolutions [16].

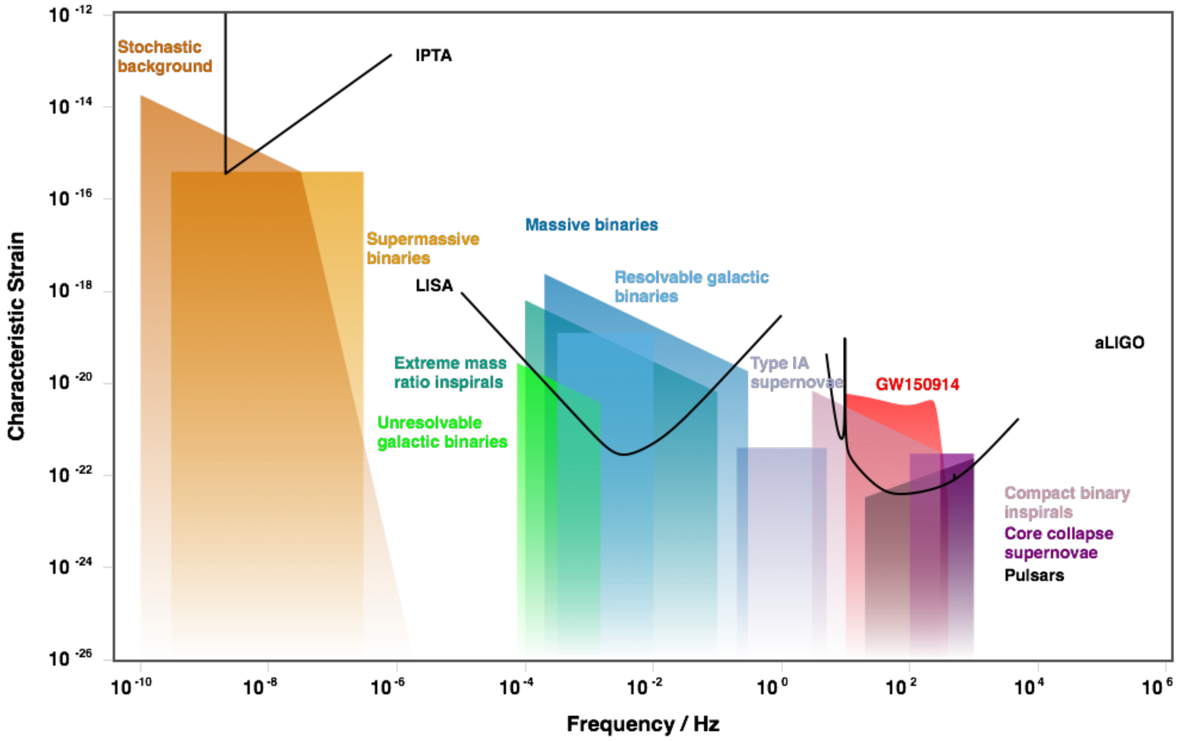

Figure 1.4: Ampltiude spectral density plot of typical strains for GW sources, and the IPTA, LISA and AdLIGO observatories. From [21].

Core-collapse supernovae Type II supernovae, the most energetic events in the Universe, are not fully understood by astrophysicists. A type II supernova is a phenomenon where the core of a massive star implodes from its own gravitational force, which is followed by an extreme shock-wave explosion of outer crusts. In theses processes, an excessive amount of neutrinos is released, but also GWs and EM radiation, making Type II supernovae excellent candidates for multi-messenger astronomy. From these observations, for instance, constraints could be deducted for the mass of neutrino's and gravitons [15].

Second generation telescopes could scan for core-collapse supernovae in the Milky way, and third generation telescopes will be able to look further. Most GW emission of core-collapse supernovae occurs at frequency range $f = 200$ - 1000 Hz, but also low frequency GW memory emission in 0-20 Hz is emitted in the remnants of the supernovae, possibly detectable by the third generation observatories [16].

And new sources? With ever advancing technology the twentieth century has been a golden era for astrophysics, with telescopes scanning the sky over the entire EM spectrum. As EM observations have revealed phenomena in the Universe that were not known when discovered, GW observations might also reveal never hypothesized phenomena.

1.2. Gravitational waves telescopes

1.2.1. A giant Michelson-Morley interferometer

The goal of a GW telescope is to observe a strain h, the relative displacement between two points in space, induced by a GW. In order to measure h, GW detectors track relative distances of freely-falling mirrors, or *test masses*. The distances are measured by means of a km scale Michelson-Morley interferometer, where difference in the travel time of light in the two arms is a measure of strain induced in the system, see Figure 1.5. The arms are typically a few km long for second generation telescopes, but by employing *Fabry-Pérot* cavities, the total travel distance of light in each arm is lengthened to around thousand km, as the telescope's sensitivity increases with light distance travelled. Resolution

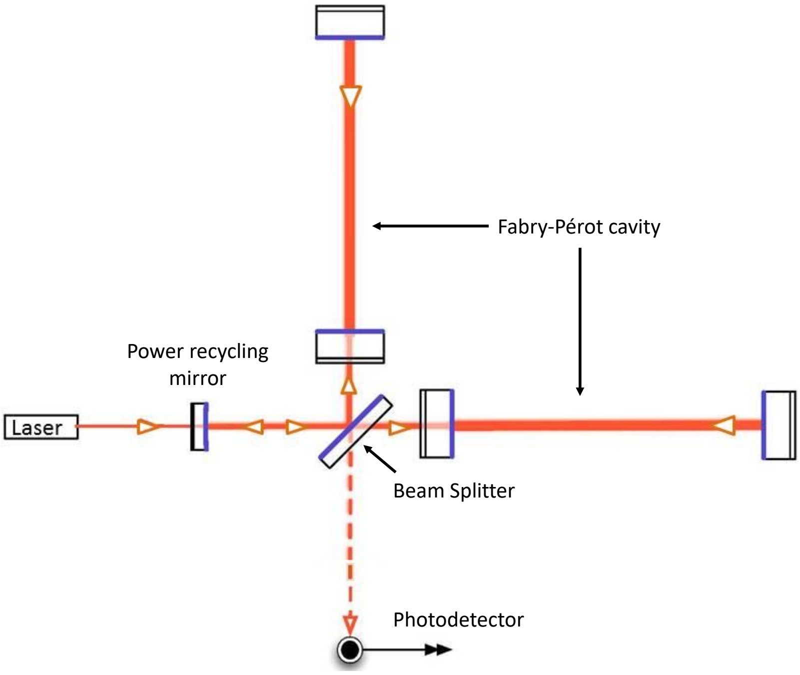

Figure 1.5: A schematic overview of a second generation interferometric Gravitational Waves telescope. Light from the laser passes the power recycling mirror and is split into two arms with Fabry-Pérot cavities, or light storage arms, that effectively lengthen the total distance travelled by the light to over 840 km for AdVirgo and 1100 km for AdLIGO. The output signal on the photodetector is proportional to the difference in phases of the light coming from both arms, and thus to strain from a passing GW that stretches the distance between test masses in one arm, and squeezes the distance in the other. Credit: LIGO.

of the interference pattern on the photodiode is enhanced by using a partially reflective mirror, called the *power recycling mirror*, placed between the laser and the beam splitter. A sizeable amount of the light that travels back to the laser is reflected back into the interferometer by the power recycling mirror, effectively boosting the power of the laser light to several kW. Many components of the setup, like the test masses, the photodiode and auxiliary optical tables, are suspended and in vacuum in order to attenuate seismic motion.

A strain $h(t)$ is sensed by a GW telescope as a minor perturbation of space-time made up of the two components [16]:

$$h(t) = F_{+}(\theta,\varphi,\phi)h_{+}(t) + F_{\times}(\theta,\varphi,\phi)h_{\times}(t) \tag{1.12}$$

where $F_{+}(\theta,\varphi,\phi)$ and $F_{\times}(\theta,\varphi,\phi)$ are antennae responses to the $+$ and $\times$ strain polarizations, depending on the polarization angle ϕ and the angles (θ,φ) that describe the location of the object in sky. Using multiple detectors, (θ,φ) and $h_{+}(t)$ and $h_{\times}(t)$ can be accurately derived from triangulation techniques [16].

Current second generation GW telescopes that are based on the principles described in this section, are the advanced Virgo (AdVirgo) detector in Italy, the two advanced LIGO (AdLIGO) detectors in Livingston and Hanford (US), the KAGRA detector in Japan and the GEO600 research and development facility in Germany. A new Indian based LIGO detector has been approved and will eventually join the GW observatory network as a fifth participant.

The two LIGO detectors and Virgo are currently the only observatories that have sufficient strain sensitivity to measure GWs. However, KAGRA, with similar strain sensitivities, is expected to join the O3 observation as of late 2019.

1.2.2. Strain sensitivity and sensitivity limitations

Strain sensitivity is the most important characteristic of a GW detector. This figure is generally depicted in a strain *Amplitude Spectral Density* (ASD) graph, telling the minimum h amplitude the detector is able to measure at a given frequency. Sensitivity curves for second and third generation telescopes are plotted in Figure 1.6. Strain sensitivity is directly proportional to the distance of the light travelled

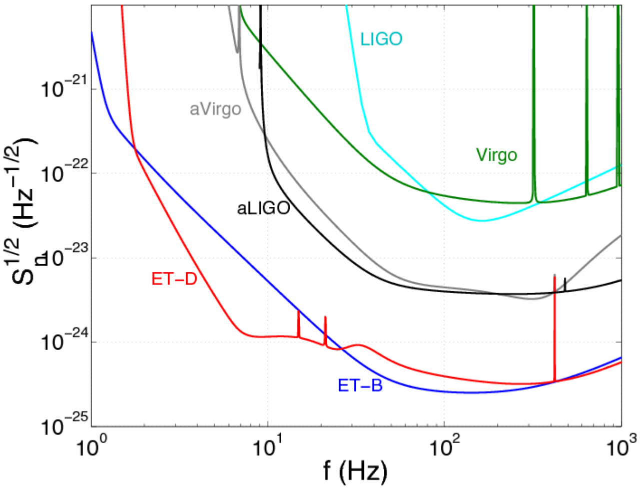

Figure 1.6: The strain ASDs of second generation telescopes (LIGO and Virgo) and their upgrades (AdLIGO and AdVirgo), as well as projected strain ASD scenarios for the third generation Einstein Telescope (ET). From [22].

through each arms' cavity.

Sensitivity of interferometric GW detectors are limited by three main sources of noise: seismic noise, quantum noise and thermal noise. Each noise source limits the detector in a different frequency band, see Figure 1.7.

Seismic noise As for a km scale GW interferometer, relative displacement measurements of below 10^{-18} m/$\sqrt{\text{Hz}}$ are required, whereas the ground can move with amplitudes of 10^{-7} m$\sqrt{\text{Hz}}$, the test masses are suspended with multiple stage pendula and spring systems in order to attenuate seismic motion. The isolation of seismic noise is the central theme of this research, and its principles are lined out in more detail in Section 1.3. Seismic noise becomes limiting at low frequency (below10 Hz).

Thermal noise A fundamental thermodynamic phenomenon is that energy in a system scales with the product $k_B T$, the Boltzmann constant times temperature. This thermal energy induces random Brownian motion of the atoms that make up the coating layer on the mirrors, or the suspension fiber of the test masses, adding a white noise contribution to the detector signal. As this noise scales with temperature, future GW observatories tend to operate their suspensions in cryogenic conditions. For the accelerometer instrument (described in Chapter 3), thermal noise limits the instrument's sensitivity at low frequency, and details of this noise source are elaborated on in Section 3.2.2. Typically, thermal noise is limiting at low and intermediate frequency (40 - 400 Hz).

Quantum noise For GW interferometers, quantum noise is the label for an ensemble of noise contributions that arise from the quantum nature of the light source and the photodetection process. Heisenberg's uncertainty principle constraints the measurement of physical quantities in two noise sources:

- **Radiation pressure noise** is induced by the radiation of the light source that causes momentum variations on the mirrors. Due to the statistical spread of the amount of photons, random momentum fluctuations are created.

- **Shot noise** is also a result of the quantum behaviour of a beam of photons. The random spread in their number N falling on the photodetector, creates a statistical error in the signal of $\sigma = \sqrt{N}$.

The two quantum noise sources are connected in such a way that increasing laser power would improve a GW detector's sensitivity at higher frequency due to an increase in the number of photons, but it would reduce sensitivity at lower frequency from an increased uncertainty in mirror momentum [2]. A technique called *squeezing* is invented to direct phase noise towards amplitude noise, lowering the shot noise at high frequency at the cost of increased radiation pressure noise at intermediate frequency. For second generation GW telescopes, radiation pressure noise contributes at intermediate frequencies and shot noise limits at frequencies above 400 Hz.

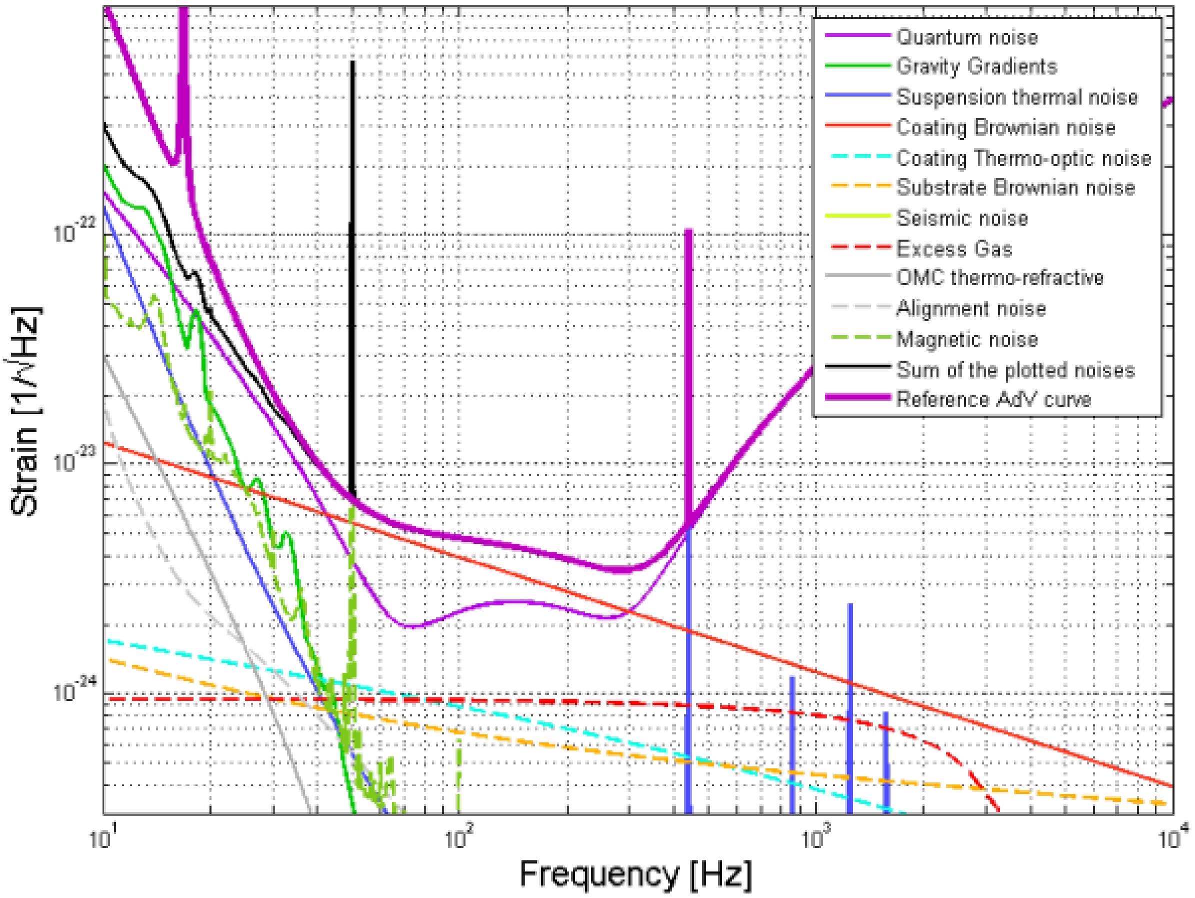

Figure 1.7: Noise contributions for advanced Virgo. From [23].

(a) Virgo - Pisa, Italy

(b) LIGO - Livingston, U.S.

(c) LIGO - Hanford, U.S.

Figure 1.8: Aerial views of second generation GW observatories currently measuring GWs. Credits: Virgo collaboration and Caltech/MIT/LIGO Lab.

1.2.3. Results and future plans

The first GW observation was made in September 2015, by the two LIGO detectors separately. It was the BH-BH merger GW150914. With this observation, a long standing unproved prediction by the General Theory of Relativity has been confirmed, leading to many scientific awards for contributors to GW physics, of which most notably the 2017 Nobel Prize in Physics.

The GW170817 NS-NS merger, detected in O2/2017 by Virgo and LIGO, was followed by EM observations of the aftermath of the merger by tens of EM telescopes, on Earth and in space, measuring across the EM spectrum. After a series of BH-BH mergers, this was the first NS-NS observation by GW telescopes, and it was also the first verification of GW emitting source of non-gravitational origins [24]. The GW170817 observation and subsequent EM detections were considered a breakthrough for an era of multi-messenger astronomy.

The Virgo and LIGO telescopes have been recently upgraded and are currently in the third GW observation run, O3/2019, that started on April 1, 2019, and saw a 50% sensitivity increase with respect to runs 1 and 2 [25]. The KAGRA telescope in Japan, the underground detector with test masses suspended in cryogenic conditions, is expected to join forces as of late 2019. During O3, a GW signal suspected to come from a BH-NS merger (S190814bv) has been observed for the first time [25]. However, Gomez et al. [25] could not rule out that the signal might come from other astrophysical sources than a NS-BH merger.

International Pulsar Timing Array A multi-telescope collaboration of multiple institutions tries to measure GW stochastic backgrounds emitted at very low frequency (10 - 1000 μHz) by combining measurements of change in distances of an array of about 30 pulsars [26]. In 2016, the GW background was constrained with a 2σ limit on $h_{background} = 1.7 \cdot 10^{-15}$ at a frequency of 1 yr^{-1} [26].

Third generation telescopes Two main GW third generation telescopes are the Laser Interferometer Space Antenna (LISA) and the Einstein Telescope (ET). The design of both observatories will deviate from the regular L-shaped GW interferometers of the second generation, as they will consist of a $60°$ triangular system with three nested detectors that are sensitive to both h polarizations (see Figure 1.9). Each detector in this configuration will comprise two interferometers. There is one considerable difference between the two telescopes: one will operate on three spacecrafts in Earth's orbit and one will be placed 100 m - 200 m underground.

The ET is a project of many European Union institutions, forecasted to be in operation in the 2030s. The ET will be located underground for the stringent seismic attenuation requirements at low frequency, and its test masses will be cooled to cryogenic temperatures for thermal noise reduction. To extent the sensitivity frequency band, the triangular shape is adopted where one of the interferometers in each nested detector is used for LF GW detections, and one for High-Frequency (HF) detections. The individual interferometers will have recycled light and optical cavities in both arms. The ET is expected to observe at 1 Hz - 10 kHz and to be about ten times more sensitive than the current advanced telescopes. [15, 27].

LISA is a European State Agency (ESA) funded project, aimed to be operational in the 2030s. Two of the independent interferometric configurations will observe different h polarizations, whereas the third will be used to characterize instrumental background noise, a so called *Sagnac* configuration.

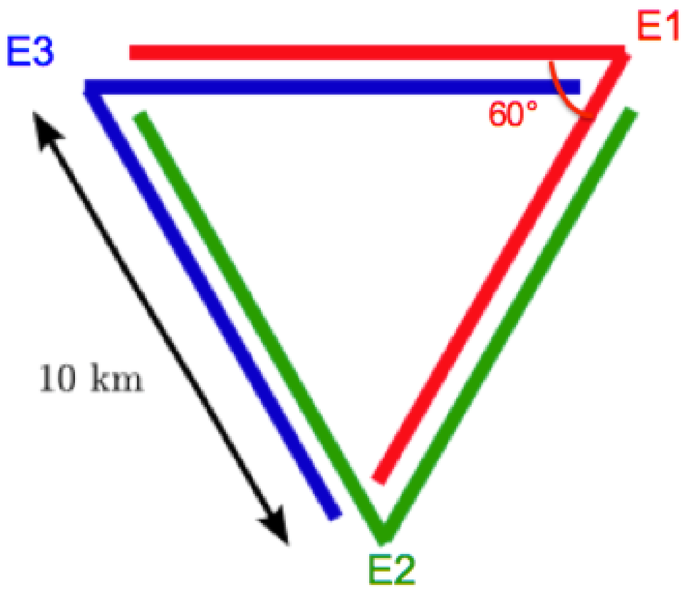

Figure 1.9: The 3-nested interferometers design of the ET. From [22].

Its sensitive frequency band is about 0.1 mHz - 0.1 Hz [28]. A Japanese counterpart to this project, DECIGO, with frequency band 0.1 - 10 Hz, is expected to be launched during late 2020s [29].

The extension of the observable GW frequency range, as well as improved sensitivities at already detectable frequencies, through the ET, LISA, and other telescopes, will allow GW astronomers to scan far deeper into the Universe and observe many more phenomena.

1.3. The Low Frequency band

1.3.1. Vibration isolation

The LF band (below 10 Hz), contains interesting GW sources, such as binary stars beyond the galaxy, merging binary neutron stars, stellar black holes in distant galaxies, LF core-collapse supernovae remnants, fast pulsars gravitational quadrupole moments, and possibly other sources (see Section 1.1.2 and specifically Figure 1.4). In this frequency region, seismic noise, coupling with optical components in the interferometer, is a dominant contributor to the noise budget of ground based observatories, such as AdVirgo and AdLIGO. To cope with this noise source, the detectors use a combined approach of active and passive vibration isolation of the test masses.

For a km scale GW interferometer, relative position measurements of below 10^{-18} m/$\sqrt{\text{Hz}}$ are required, whereas the ground can displace with amplitudes of up to 10^{-7} m/$\sqrt{\text{Hz}}$ at the micro-seismic peak (calculated from Figure 1.10). To filter ground amplitudes by over 11 orders of magnitude, the test masses are suspended with multiple stage pendula and spring systems in order to passively attenuate seismic motion above the natural frequencies of the suspensions.

To understand the mechanism of passive vibration attenuation, let's consider a simple damped harmonic oscillator, such as a mass suspended by means of a spring or a pendulum. Ground motion will accelerate the frame of the suspension, introducing a force into the system. From the proof mass' inertia, relative displacement is created between the frame and proof mass. The relative distance x_r is given as:

$$x_r(t) = x_p(t) - x_f(t) \tag{1.13}$$

where x_p is proof mass location and x_f is the frame location. For any suspended system, the response of x_p to a displacement x_f of the frame (due to ground motion) is in Fourier transforms [18]:

$$\frac{X_p}{X_f} = \frac{\omega_0^2}{\omega_0^2 - \omega^2 + i\frac{\omega\omega_0}{Q}} \tag{1.14}$$

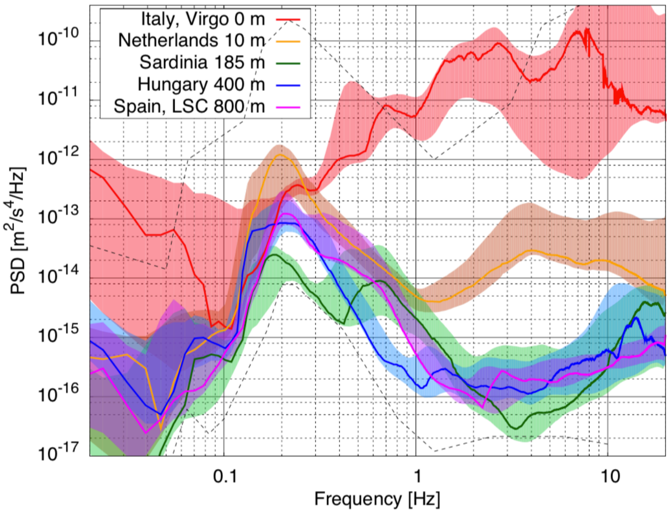

Figure 1.10: Power spectral density (PSD) plot of seismic noise at different sites and depths. In a PSD, the amplitudes of ground acceleration are squared. At about $f = 0.3$ Hz, a large peak is visible for each spectrum. This is the *microseismic peak* that results from waves collapsing on the continental crust. From [30].

where M is the mass of the suspension, ω is the angular frequency of the frame acceleration and ω_0 is the natural frequency of the suspension. Q is the quality factor, a measure of mechanical damping in the system (more on this in Chapter 2). In Figure 1.11 the transfer function of a $f_0 = 1$ and $Q = 10$ suspension is shown. It is clearly seen that, above the natural frequency, the response to ground motion reduces with f^{-2}, whereas ground motion below f_0 induce flat proof mass response. In this way, passive vibration isolators could be recognized as low pass filters for motion. Motions around the natural frequency f_0 are amplified.

The attenuation of a suspension above f_0 can be increased more dramatically by using a chain of N pendulums or springs. In this situation, the transfer function of Equation (1.14) will be proportional to f^{-2N} [15]. For instance, AdVirgo employs a $N = 6$ pendulum chain to suspend a test mass (the super-attenuator, depicted in Figure 1.12a), and this would attenuate ground motion with $\sim f^{-12}$ above f_0. A ground motion of 10^{-7} m/$\sqrt{\text{Hz}}$ at 10 Hz will be damped with 12 orders of magnitude to 10^{-19} m/$\sqrt{\text{Hz}}$, spanning the detector's isolation requirements for relative position measurements of $< 10^{-18}$ m/$\sqrt{\text{Hz}}$.

However, Figure 1.11 shows a resonance peak at f_0 for an attenuation system that consists of only one suspension. Obviously, such a resonance will be introduced for every extra suspension added to the system, creating 5 additional peaks for an AdVirgo $N = 6$ suspension chain. For this reason, on each suspension platform, AdVirgo combines the information from local sensors to actively damp the peak resonances with local actuators. Next to that, an important feature in AdVirgo's suspension design is that additional inverted pendula and anti-springs are assembled into the suspensions, lowering their natural frequencies [31].

In contrast, AdLIGO suspensions, as depicted in Figure 1.12b, are based on a more active isolation strategy. In general, active control is performed by means of a closed feedback loop, where a sensor's signals are sent to a controller that generates counter-signals to environmental disturbances, which are then sent to the actuator acting on the suspended mass. In a LIGO suspension, the first isolation stage is a pre-isolator stage (in blue in Figure 1.12b) that controls DC positioning and alignment via hydraulic actuators. Then, two Internal Seismic Isolation platforms (in grey in Figure 1.12b) provide two active stages of seismic isolation and pendulum-resonances damping for frequencies below 10 Hz, using low-noise inertial sensors. Finally, the four staged suspension cascade provides passive isolation for the mirrors above 10 Hz.

A combination of passive Virgo with active LIGO isolation is increasingly aimed for in future upgrades of second generation observatories, as well as in the Einstein Telescope [2, 27]. This results in the need for ever more sensitive displacement and inertial sensors.

1.3.2. Inertial and relative position sensors

Control of different suspension stages in GW detectors is done with signals from two sensors: inertial sensors and relative position (displacement) sensors. The main difference between the two is that inertial sensors measure absolute motion of the frame on which they are placed, whereas displacement

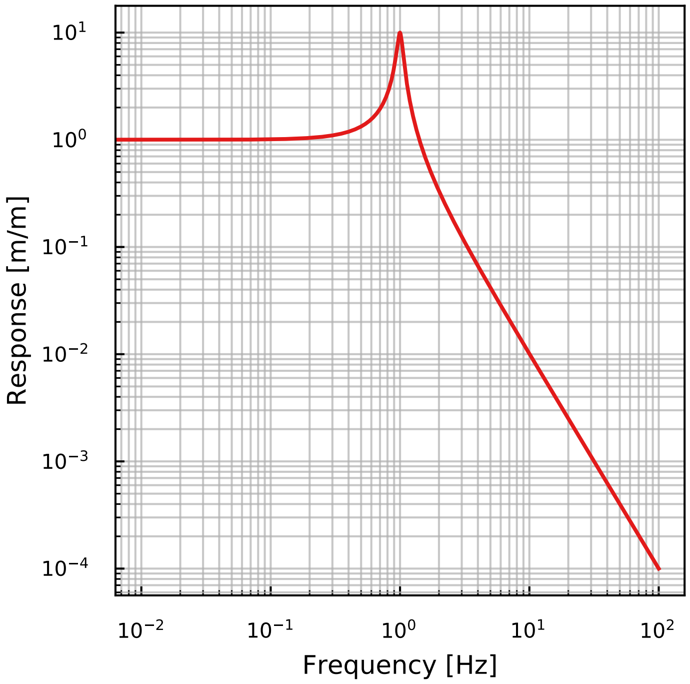

Figure 1.11: Modelled proof mass response to ground motion. In this example, the suspended proof mass ($M = 1$ kg) has natural frequency $f_0 = 1$ Hz and quality factor $Q = 10$.

sensors measure the relative position between two mechanical components.

Inertial sensors In essence, the physical concept of vibration isolation is the same for an inertial sensor, as it also consists of a frame and of a suspended mass. From the proof mass' inertia, a relative displacement is created between the frame and proof mass. By tracking relative distance x_r absolute frame acceleration can be derived from the forced transfer function H:

$$\frac{X_r}{F} = H = \frac{1}{M\left((\omega_0^2 - \omega^2) + i\frac{\omega\omega_0}{Q}\right)} \tag{1.15}$$

Equation (1.15) states that at a specific frequency ω $(= 2\pi f)$, the transfer function H maintains the amount of force F *transferred* to the relative displacement X_r in Fourier space. Inertial sensors have linear - or *flat* - response to frame acceleration below f_0. Thus, measuring X_r and translating that into a $\ddot{X_f}$ output, an *accelerometer* is obtained. Many accelerometers operate in closed feedback loop, where variations in measured X_r signals are processed by a controller, and sent to an actuator that acts on the proof mass. The feedback signal is used as sensor output. In this way, the flat response line is extended over a bandwidth as defined by the controller characteristics.

Inertial sensors that are often used in isolated stages of suspensions are geophones, as the Sercel L-4C, the Sercel L-22, and the GeoTech GS-13. In a geophone, a coil is wounded around a spring-suspended proof mass and permanent magnets are mounted on the frame, close to the coil end. If the coil moves with respect to the magnets as a result of proof mass inertia, an electromotive force is induced in the coil that scales with velocity of the coil [2]. The acceleration response to the velocity measurement is of the same shape as the line in Figure 1.11. The resolution of the most sensitive geophone, the GeoTech GS-13 is at below 100 fm/$\sqrt{\text{Hz}}$ from 20 Hz onwards.

Displacement sensors Displacement sensors measure the relative distance of one object with respect to another. Such sensors cannot distinguish from which of the objects comes the motion that creates the displacement. Therefore, these sensors are commonly not used for seismic measurements, but primarily for DC positioning and low frequency control.

A widely used position sensor is the Linear Variable Differential Transformer (LVDT) that works in a coil configuration where signals between the two components are transported via magnetic induction

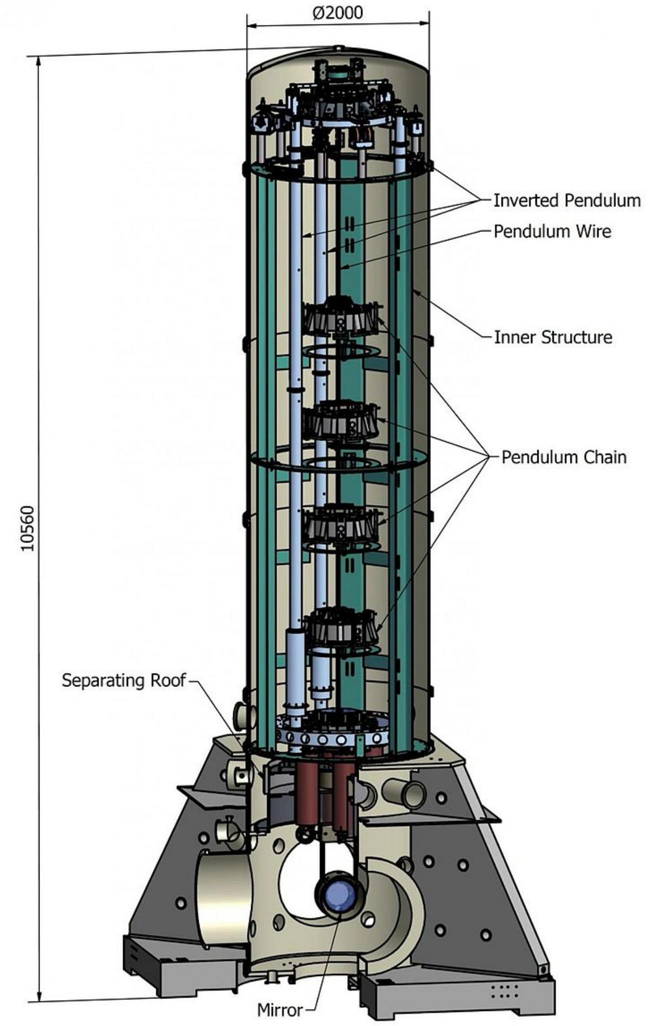

(a) 9 m long AdVirgo test mass suspension (CAD illustration). Credits: Virgo collaboration.

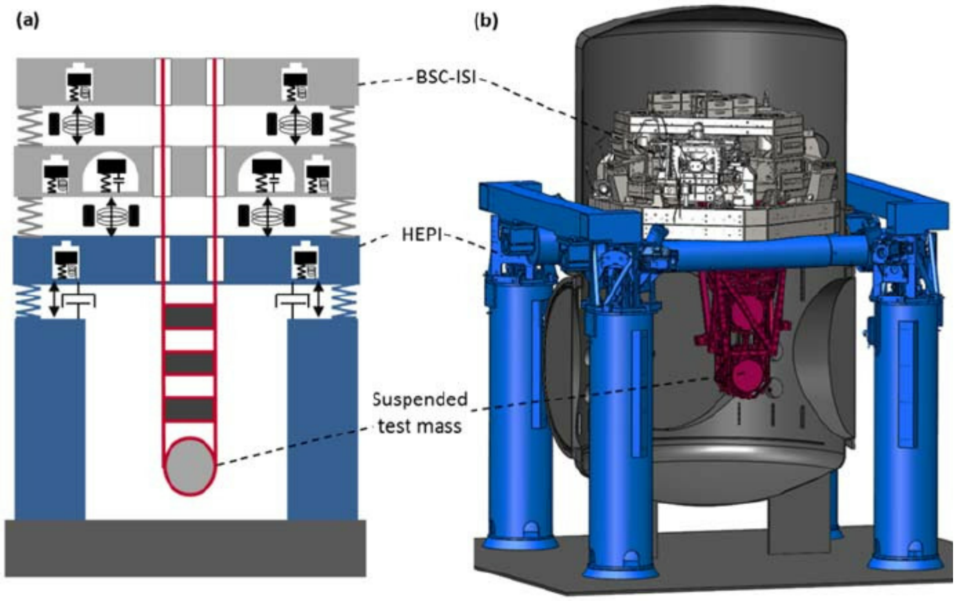

(b) Several m long AdLIGO test mass suspension. Schematic in (a) and CAD illustration in (b). From: [32].

Figure 1.12: Virgo and LIGO test mass vibration isolation strategies. The Virgo super attenuator depicted in (a) consists of a 6 stages pendulum chain and active inertial control is performed to damp their harmonics. The LIGO mirror is suspended by four much shorter pendulum stages, and seismic motion at low frequency is actively isolated via the two stage ISI platforms (in grey in the schematic), using low noise inertial sensors.

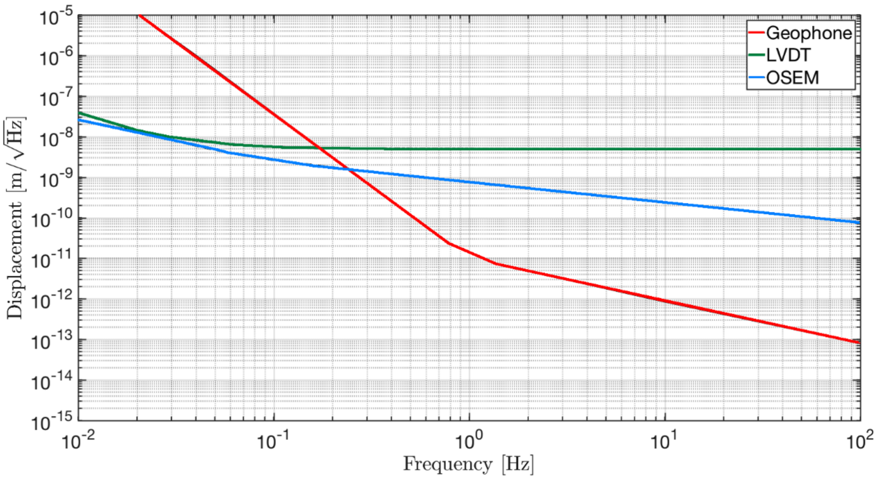

Figure 1.13: Sensitivity curves for three GW sensors, the LVDT, the OSEM and the Sercel L-4C. From [2].

[33]. The displacement noise of an LVDT is about 1 nm/$\sqrt{\mathrm{Hz}}$ over a range of about 8 mm [2]. A sensor in an environment quieter than the sensors self-noise would see its noise fed back into the system. Therefore, this sensor is mainly used for DC alignment measurements of top pre-isolator stages.

For angular alignment and active control of the mirror and of the penultimate suspension stage, so-called Optical Levers are used in GW detectors. For the penultimate suspension stage, a tiny mirror is fixed to the body of the suspended mass, while for the test mass simply the reflective coating is used. The components of the Optical Lever are placed outside the vacuum chamber. Light is sent with an angle to the target through a viewpor,t and the reflected beam is collected through another viewport on a Position Sensitive Detector. With a lever arm of the order of 1 m, noise leves of 1 nrad/$\sqrt{\mathrm{Hz}}$ ar typically achieved. Two rotational angles are calculated from position changes of the beam. The functions of the Optical Levers are: 1) damping the unwanted angular modes involving the mirror, 2) being able to set and recover the reference angular position of each mirror, and 3) keeping the interferometer aligned at the level of about 1 μrad rms or better for locking the laser. The higher the resolution of the Optical Lever, the more aggressive the rotational modes could be controlled, which would result in enhanced strain ASD at LF.

At LIGO a commonly used relative position sensor is the Optical Sensor and Electro-Magnetic actuator (OSEM). This integrated assembly consists of both a position sensor and an magnet-coil actuator. A shadow sensor, mounted on one component, follows the position of a flag mounted on the other. For feedback actuation, a magnet is attached to the flag that can be driven by a coil on the other component. The OSEM measures at below nm/$\sqrt{\mathrm{Hz}}$ over a large bandwidth, but has a dynamic range of only $\sim$ 1 mm [2, 34].

Sensitivity curves of commonly used sensors, the geophone L-4C and the two relative position sensors LVDT and OSEM are displayed in Figure 1.13. For actively damped suspended platforms, generally a combination of inertial and relative position sensors is employed. Drift control and static positioning (low frequency measurements) is performed by position sensors. Acceleration control is performed above a certain threshold frequency by inertial sensors.

This research has focused on improving resolution of an inertial sensor and a displacement sensor: the monolithic folded pendulum (FP) accelerometer and the CCD-Rasnik, both under development at the Nikhef institute. Their performance is compared to the currently in-use GW inertial and displacement sensors, to see whether they might be interesting alternatives for active control.

The monolithic folded pendulum accelerometer The monolithic FP accelerometer is a horizontal inertial sensor. *Folded* means that the mass is suspended by a combination of two pendulum legs, one regular and one inverted, see Figure 1.14. The legs are suspended via four thin flexures per pendulum leg. When the ground displaces, proof mass inertia is created, and the FP accelerometer tracks the relative position between proof mass and frame, by means of laser interferometer, see Figure 1.14. Operating the accelerometer in a closed feedback loop allows it to measure at full dynamic range, and to ensure a linear response over the full feedback bandwidth.

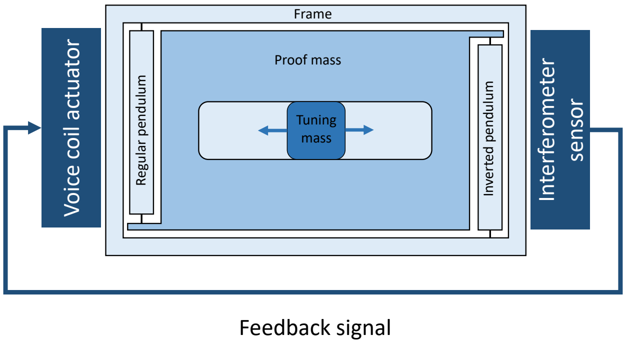

Figure 1.14: Schematic of the monolithic FP accelerometer operated in closed feedback loop, with a voice coil as actuator and an interferometer as readout sensor.

Previous research has measured a resolution of 8 fm/$\sqrt{\text{Hz}}$ from 30 Hz and onwards for the monolithic FP accelerometer, but this result was more than a factor two above its modelled noise floor [2]. Inspecting Figure 1.13, it is seen that, when this precision is achieved, the accelerometer would outperform the geophone L-4C by more than an order of magnitude at $f = 30$ - 100 Hz.

The CCD-Rasnik Rasnik has been operated in large volumes at CERN projects, measuring three point alignments (*sagitta*), for many years. It has proven a robust, easy to operate and inexpensive sensor that met the precision requirements of particle detector chambers' alignments.

A Rasnik system consists of three components. Light from a back-illuminated mask is projected by a lens onto an image sensor that records a sequence of images. From this sequence, a dedicated image analysis routine determines displacements of either of the aligned objects. Past experiments have shown that Rasnik systems typically had a time-integrated rms error of about 25 nm, while they were modelled to operate at sub nm precision [1]. In this research experiments were conducted to understand thid discrepancy and to improve Rasnik's performance, to show it's potential to operate as relative position sensor in GW experiments.

2

Rasnik

Rasnik is a three point alignment sensor originally developed for muon detectors. To determine the momentum of passing muons, a precise alignment of the muon detector chambers is required. The sagitta s of a passing muon is the distance from the center of the muon arc to the center of the base, i.e. the line connecting the two outer measured positions. From the sagitta of the muon, the radius of its path of motion is estimated, from which its momentum is determined. The error in measuring s is, among others, directly related to the alignment of the detectors. For this reason Rasnik was developed, to keep track of the sagitta of particle detectors and establish errors in alignment.

Rasnik - *Red Alignment System Nikhef* - has grown to be a successful project with a history of over 30 years of R&D and many applications [1]. Rasnik systems had been employed for monitoring alignment in the L3 muon chambers at LEP in the 1980s/90s and are still used extensively in the Atlas detector at LHC, since the 2000s. Besides, Rasnik has served many industrial applications. Over the years Rasnik has evolved to many different forms, such as RasDiff and RasClic [1], but the focus of this research was on the common CCD-Rasnik.

Rasnik can measure sagittas and/or displacement at high precision over an arbitrary large range. It is uncomplicated in design, cheap and easy to operate.

In the aforementioned experiments, Rasnik measures sagitta of three aligned components. By allowing only one component to move with respect to the other two, a relative displacement sensor is obtained. Based on this idea a new concept developed: to employ Rasnik as a displacement sensor in X and Y, by mounting two components to a common base plate and fixing the other component to an independently moving part. In past experiments, Rasnik systems have optimally been able to measure displacement (sagitta) with a RMS of about 30 nm, while they were modelled to measure at below nm RMS [1, 35]. The discrepancy between measurement and model is the verification of this research, because when its causes are found a Rasnik displacement sensor with sub nanometer-scale precision may be developed.

This chapter is devoted to find causes for the discrepancy between Rasnik's modelled noise floor and measured precision, and to improve Rasnik's displacement sensing precision. In Section 2.1 the principles of a Rasnik system are explained, and its sources of error are evaluated. The optimally achievable precision is calculated in Section 2.2, by means of a Cramér-Rao Lower Bound analysis. In Section 2.3 performances of different Rasnik systems are measured, and limitations on precision are discussed. Conclusions are stated in Section 2.4. Lastly, future applications of Rasnik as a relative position sensor for GW detectors are discussed in Section 2.5.

2.1. The Rasnik optical alignment system

2.1.1. Principle of operation

Rasnik's three components are the back-illuminated ChessField-coded mask, the lens and the pixel image sensor. Rasnik's optical axis is defined as the line from the center of the image sensor going through the center of the lens, pointing to the mask, see Figure 2.1. The mask defines the coordinate

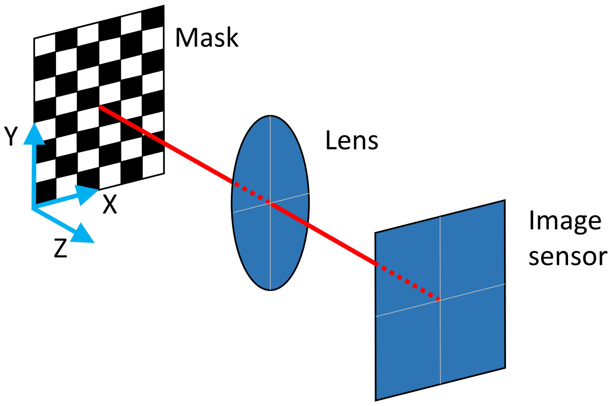

Figure 2.1: Light from a LED is diffused and back-illuminates the ChessField encoded mask, whose image is projected by a plano-convex singlet lens onto a pixel image sensor. The lens is centered between the mask and sensor for focused images. Image processing software tracks displacement of either of the aligned components, recorded as image shifts on the sensor. Rasnik's optical axis is depicted in red. Its crossing point with the below left corner of the mask defines the transversal coordinate system, indicated in light blue.

system, as X and Y responses are specified as the distance from the below left mask corner. When one of the aligned components moves in X or Y, the projected image will shift in this coordinate system, and image processing software creates a response to this displacement. Only a small section of the ChessField mask, close to the optical axis of Rasnik, is projected onto the sensor. The image processing software uniquely recognizes each section, resulting in the large X and Y measurement range of Rasnik, defined only by the size of the mask. The image processing software also determines rotation around Z of the mask or sensor (but not of the lens), and it calculates displacement in Z from the scales of the ChessField images. It is important to note that the image processing software cannot distinguish which of the aligned components moves, and that X, Y and Z displacement of the lens is equivalent to twice that displacement of the mask or cam.

2.1.2. Components of Rasnik

Figure 2.1 shows the three components of a Rasnik system: 1) the back-illuminated ChessField-coded mask, 2) the lens and 3) the image sensor. The image analysis software is not a physical component that could influence a measurement, and is therefore described separately in Section 2.1.3.

1) The back-illuminated ChessField mask The spatial reference of a Rasnik system is stored in the ChessField pattern of the mask, making it the essential and only precision defining element of Rasnik. The image processing software can decode the pattern to a position output in Cartesian coordinates. As this algorithm regards the periodicity of black-white transitions, H. Groenstege (Nikhef) invented the ChessField patterned mask to maximize the number of contours in X and Y. The ultimate precision of Rasnik thus increases with the number of squares in the ChessField pattern. However, the Modulation Transfer Function (MTF) - the ratio that tells how much contrast in the original object is retained by the image on the sensor - decreases as spatial frequency patterns increase, and a reduction in black-white ratio's translates into a reduced Rasnik resoluion. In this way, the MTF sets a maximal number of ChessField squares for which the projected image remains distinguishable.

The transversal coordinates X and Y are embedded in a *coarse* and *fine* position of the mask [1]. The coarse position is digitally encoded in every 9^{th} row and 9^{th} column of the ChessField, see 2.2b. Only a section of the full mask is projected, and these rows and columns contain information about which section that is.

The fine position information is embedded in all transversal black-white transitions of the image. Fitting an error function to intensity values of a row of pixels trespassing a black-white or white-black contour will provide a contour X position. The precision of determining this position is basically dependent on three factors: errors in mask contours, diffraction in the system and pixel noise in the image sensor. The ChessField square wave nature of all contour positions is analyzed by a Fourier analysis procedure, and its frequency and phase information determine the fine position (as explained in Section 2.1.3). The fine position defines the precision of Rasnik and it is combined with the coarse position to provide a final X and Y response output.

The X and Y output coordinates are determined from a point in the mask plane projected onto the sensor, see Figure 2.1. This point is the distance from the cross point of Rasnik's optical axis with

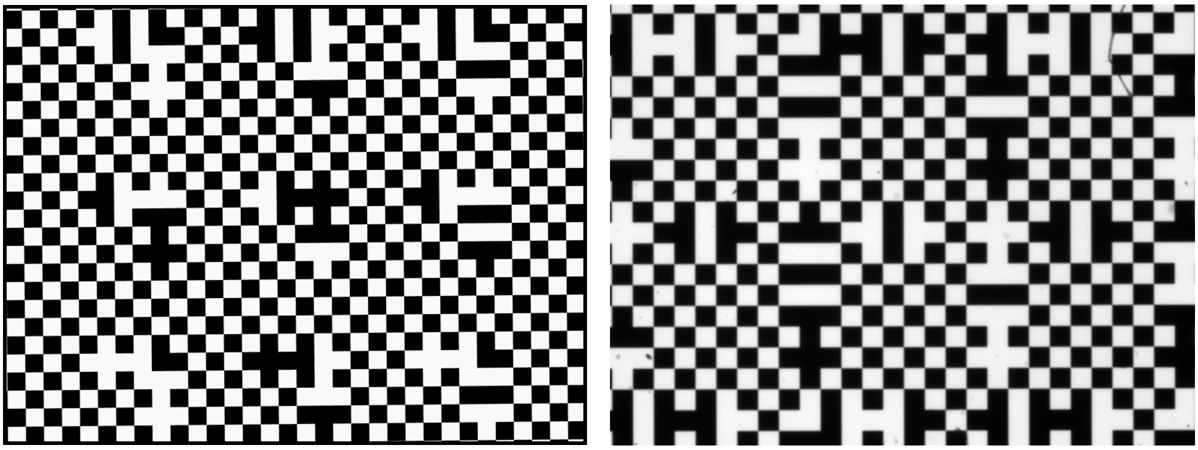

(a) A simulated ChessField image, with no diffraction and no pixel noise.

(b) A typical Rasnik image, taken with the MER image sensor.

Figure 2.2: A simulated ChessField image and a typical recorded Rasnik image. Both have pixel size $d_{pix} = 4.8$ μm and ChessField sizes of 120x120 μm. In (b) pixel noise is visible when zooming in, diffraction is seen at contour edges and minor irregularities are visible (for example the hair in the above right corner).

the mask's below left corner, with respect to the ChessField's horizontal and vertical axes. The mask orientation thus defines Rasnik's coordinate system, and consequently X and Y outputs are unaffected by relative rotation between the mask and pixel image sensor around the optical axis: rot(Z).

It is important to note that only a small section of the mask's pattern is projected onto the sensor. Therefore, as each section of the ChessField is uniquely identified by dedicated software coding, this results the arbitrary large detectable range over which the mask can move. This large range is typical for Rasnik systems, and is a main advantage over other displacement or alignment sensors. What is more, the contour precision is extremely fine (in the photo-lithographic industry, contours of a few micrometers can be drawn with precision of < 50 nm [1]. The mask is thus Rasnik's high precision component and defines the large dynamic range.

The back-illuminating light source should illuminate the mask homogeneously. This is usually achieved by using a LED that shines on an opaque Lambertian surface, which diffuses the light homogeneously. Any small intensity noises that are still emitted through the diffusor, are disregarded as the image analysis software exploits the periodicity of the ChessField pattern. A disadvantage of using a Lambertian surface is that only a fraction of the LED light's intensity is diffused towards the mask. The LED used for this research is the Luxeon Z, with color Royal Blue ($\lambda = 447.5$ nm with spectral half-width $\Delta\lambda_{1/2} = 20$ nm).

2) The lens For Rasniks, generally a plano-convex singlet spherical lens is used to project the mask image onto the sensor. The lens is centered between the object (the mask) and image (the sensor). Its focal length is $1/4^{th}$ of the object-image distance, creating a 1:1 scaled image. Displacement of the lens results in an image shift equivalent to twice the same displacement of the mask or sensor. Rotating the lens around its optical axis does not affect the image.

The size of the lens diameter, and thus aperture, affects diffraction, light yield, geometry and cost of a Rasnik system. A large diameter with aperture reduces image blurring from diffraction, and has a high light yield, reducing pixel noise and background light disturbances. However, a large diameter is more expensive, and it results in a large light beam space required and in a smaller Depth of Field (DOF). The DOF is the range in the optical axis Z in which the image is projected sharply, thus it determines the operating range for Z measurements. A too large diameter with aperture is undesirable as non-linearities, such as the pincushion effect (see Section 2.1.4), may become disturbing.

A typical Rasnik aperture is small: it is in the order of $f/25$ (a twenty-fifth of the focal length). As diffraction increases proportionally with decreasing aperture, diffraction from such a small aperture is expected to set a fundamental limit in image resolution. This makes a Rasnik diffraction limited system. Diffraction blurs contour edges and reduces black-white ratio's, as specified by the MTF. Together with pixel noise diffraction creates a limit in precision of determining contour positions.

By enlarging the image of the mask on the sensor, displacements of the mask will be enlarged. This can be done by placing the singlet lens closer to the mask, but optical aberrations are expected to distort images too much. Therefore, a new concept was developed: placing a microscopic objective lens near the mask. This instrument is called RasMic. The precision of RasMic, in terms of spatial resolution of the mask displacement, is expected to improve linearly with the magnification factor of the objective lens. RasMic's objective lens has large aperture to reduce diffraction and increase light strength. Displacement in Z cannot be measured though because image scaling is not proportional to object distance. A first characterization of a such a RasMic system is made in Section 2.3.2.

3) The image sensor As its name suggests, a CCD-Rasnik system uses a CCD pixel image sensor. However, also CMOS image sensor are used, which do not alter the system's operation principles but could mainly affect pixel noise. In fact, the sensors used for the characterization of RasMic (Section 2.3.2) are CMOS camera boards, taken out of Logitech C250 consumer webcams, with undefined pixel sizes (the C300 series is known to have pixel size $d_{pix} = 11.2$ μm though [35]). Also Pike-F100B CCD cameras with pixel size $d_{pix} = 7.4$ μm were used for RasMic measurements. The CMOS and Pike sensors used for RasMic have sample frequency of about $f_s = 30$ Hz. The Rasnik system described in Section 2.3.3 uses the Mercury MER-051-120GC sensor with pixel size $d_{pix} = 4.8$ μm and maximum sampling frequency $f_s = 120$ Hz. The theoretical performance calculations are also based on images taken with this camera.

The size of the pixels influence Rasnik's precision and an optimal pixel size exists to detect black-white transitions in diffraction limited ChessField images. The pixel noise, in combination with diffraction, determines the ultimate precision of Rasnik.

2.1.3. The image analysis algorithm

The projected ChessField images are recorded by a pixel image sensor and each image is analyzed by an image processing routine that creates a (X,Y,Z,rot(Z)) position output in the mask coordinate system (see Figure 2.1). To find the positions of contour edges, the first Rasnik routines employed gradient filters to the images and fitted lines over the gradients [36]. These routines' fitting results were imperiled by blurring, irregular illumination and unwanted artifacts in the image (such as dust spots or hairs) [37]. Therefore a replacing algorithm was developed, called FOAM (Fourier Analysis Method). The FOAM routine exploited the wave nature of the ChessField pattern, and was therefore largely unaffected by the blurring, irregular illumination or artifacts in the image, because these effects do not influence periodicity to a reasonable extent [37]. From the FOAM routine, finally the SOAP image analysis algorithm emerged, whose principles are equal to those of FOAM, but it includes new pattern recognition for the coarse codes. SOAP is the algorithm used for this research.

Like FOAM, SOAP computes a 2D Fourier Transform of the ChessField images, and deduces X, Y, Z and rot(Z) from frequency and phase information of the image in Fourier space [1, 37]. The SOAP routine broadly consists of the following steps:

- **The Fast Fourier Transform.** A two dimensional discrete Fourier transform is taken from the ChessField image, whose squares are found by fitting the convolution of a square wave in X with a square wave in Y. The FFT spectrum obtained by this calculation contains peaks with information on the average value of the ChessField pattern and its base frequency.

- **Locating the peaks and fitting.** Peaks in the FFT spectrum are located by fitting 2D Gaussians to the spectrum. From many fitted peaks, two primary peaks are selected based on similarity of their amplitudes. Together with their first harmonics, these determine the horizontal and vertical frequency of the ChessField image. The frequency is a measure of how many ChessField squares fit into the image on the sensor. From the frequencies, the sizes of the squares are determined and the optical magnification factor is derived: Z is calculated from this factor. Besides, rotation in time space equals that in Fourier space and thus rot(Z) can be determined.

- **Peak phases.** The complex phase of a Fourier transform is linearly dependent on the translation of an input function. Therefore, the X and Y shifts of an image can be computed from the phase information of the FFT peaks. First, the phases of the two primary peaks are resolved, and then they are matched with the expected phases of the harmonics. The precision at which the algorithm is able to determine these phases establishes its precision to provide its final X and Y responses.

To summarize, from the peak locations in the FFT spectrum, the horizontal and vertical frequencies of the ChessField image are determined, providing information to calculate Z and rot(Z). Phase information of the peaks is evaluated to find transversal shifts. Finally, in order to create a final X and Y output, this fine position information is combined with analysis of the digitally encoded coarse position rows and columns.

2.1.4. Sources of error

Rasnik's precision is defined by spatial resolution and linearity of the mask position/displacement. Spatial resolution is defined as the RMS with which Rasnik can detect an X and Y displacement (or sagitta), and linearity is the proportionality between a linearly moving mask and the subsequent response output. Diffraction, causing decreased black-white ratios and contour blurring, in combination with pixel noise of the pixel image sensor, limits Rasnik's spatial resolution. In this section, first, errors from density variations in the medium are discussed. Then, errors intrinsic to Rasnik components, which define Rasnik's ultimate precision, are treated. Finally, errors from thermal variations in Rasnik mounts are reviewed.

Density variations in air Locally in the medium, the density of the air (ρ_{air}) can show variations due to convection (thermal gradients) or air flows (pressure gradients). This creates local variations in the medium's index of refractin n which results in light rays in the image beam to follow distorted paths, creating shifts in the position of the projected image on the sensor.

When ρ_{air} fluctuates randomly in the medium through which Rasnik's light beam traverses, it results in a rapid shifting and distorting of projected images [35]. When no gas flows are present, density fluctuations could especially become significant close to heat dispersing components, such as the LED and pixel sensor [38]. Density gradients and air density fluctuations become increasingly disturbing when distances between Rasnik's aligned components, L, increase, because the light beam passes through a larger amount of air that facilitates these errors. The effect of density gradients increases with L^2, for instance [1]. In past measurements, a technique called ”thermal shielding” was used to suppress density variations, where aluminum cases shielded off air exchange between the light beam and surrounding environment [35]. This diminished thermal errors not completely however. Therefore, placing the system in a < 1 mbar vacuum environment, where the mean-free-path (*mfp*) is comparable to the beam diameter, is regarded sufficient to rule out gradients in ρ_{air}.

1) Errors from the back-illuminated ChessField mask For a low-cost CMOS webcam pixel sensor with a 3 mm x 2 mm image surface, contours with 100 μm distance will correspond to a total correlated contour length of about 60 mm in X and Y. This 60 mm contour edge is drawn with a precision of below 50 nm [1]. With pixel size of 6 μm, over 10^4 edges are sampled in one transversal direction and the measurement precision is enhanced by a factor of more than 100, thus to below 0.5 nm. This rough estimate of a simple CMOS webcam demonstrates the high potential precision of Rasnik. Note that the mask is the only precision-carrying component of Rasnik.

Noise in the electric circuit of the LED light cause it to be a non-homogeneous emitter. However, the resulting level variations in light intensity are assumed to be well below pixel noise.

2) Optical errors In a Rasnik image, contour sharpness and black-white ratios are reduced with respect to the object (the mask), as specified by the modulation transfer function (MTF). The spatial resolution of the projected image is therefore diffraction-limited. In a diffraction-limited image, there exists a maximum amount of focused contour edges in one image, halting a possibility to improve precision by reducing the ChessField squares' sizes.

Other optical aberrations - distortions that take place as a consequence of using real (not mathematically ideal) lenses - are spherical and chromatic aberration and the pincushion distortion.

Spherical aberration is the effect where light rays away from the optical axis is refracted more than light rays close to the axis, reducing image sharpness. This effect becomes significant for large apertures, and as Rasnik lenses have small aperture, spherical aberration is not expected to limit sharpness. Chromatic aberration is the phenomenon where the index of refraction of the lens surface depends on λ, causing the incoming light to be split into different wavelength components that are diffracted at different angles, also reducing image sharpness. The small colour spread in the used LED light ($\Delta\lambda/\lambda = 20$ nm / 475.5 nm $= 0.045$) cause this effect to be insignificant.

An effect that might cause systematic edge position deviations is the pincushion effect. This happens when a point of the object, far away from the optical axis, is magnified by the lens to a larger extent than a point close to the optical axis, resulting in a non-linear pincushion-like image. This could possibly reduce the linearity of Rasnik: on the edges of the image (where this effect is strongest) the distorted contours could be projected in turns outside and inside the image as the mask moves. This results in jumps in periodicity of the ChessField, providing X and Y responses above and below the line of linearity. The pincushion effect is expected to take place for Rasniks with larger aperture sizes, but even when the effect is apparent, it can be corrected for. Moreover, pincushion does not affect precision, because the non-linear pattern is still symmetric, which leaves the square wave form fit of the Fourier algorithm to still yield an averaged ChessField pattern.

3) Errors from the pixel sensor When photons fall on a pixel they create small photo-currents (i) and charge its capacitor over the integration time t_s, producing an output charge Q, expressed in number of electrons [e^-]. The input current is generated by two sources: photons and dark currents, so $i = i_{\mathrm{ph}} + i_{\mathrm{dc}}$. For each pixel, the transfer function of the input current to an output charge $Q(i)$ is defined as [39]:

$$Q(i) = \begin{cases} \frac{1}{q} i t_s e^- & \text{for } 0 < i < \frac{qQ_{\max}}{t_s} \\ Q_{\max} e^- & \text{for } i \geq \frac{qQ_{\max}}{t_s} \end{cases} \tag{2.1}$$

Where t_s is the exposure time and q the electron charge. The saturation point is reached when $i_{\max} = \frac{qQ_{\max}}{t_s}$, then $Q = Q_{\max}$. This max pixel charge is called the full well capacity (FWC) of the pixel - the amount of charge a pixel can hold before saturating. This leads to the definition of the dynamic range of a sensor: DN = $i_{\max}/i_{\min}$, the ratio of saturation input and the minimum detectable input.

Noise in the output charge stems from different sources. Three independent noise contributions are [39]:

- **Photon shot noise** - σ_{SN}. Shot noise is a quantum noise that originates in the Poisson distributed number of photons that hit the pixel during t_s, it increases square rootely with light input i_{ph}.

- **Read noise** - σ_r. Read noise is the combination of camera specific *readout noise*, *reset noise* and *quantization noise*. Readout noise is a result of the readout electronics of the image sensor, and reset noise represents the noise resulting from the resetting procedure of the pixel capacitor before an image measurement. Quantization noise is the error introduced by quantization in the ADC (analog-to-digital converter), and is dependent on the bit-depth of the image sensor; to reduce this noise source, a higher bit sensor should be used. Quantization rms noise is equal to $\sqrt{12}$ of a bit count. Importantly, readout noise sources are independent of the light input.

- **Fixed pattern noise (FPN)** - σ_{FPN}. FPN is the deviation from spatial variation in pixel outputs under uniform illumination. FPN consists of pixel-varying gains (photo-response non-uniformity - *PRNU*), and pixel-varying dark currents (dark signal non-uniformity -*DSNU*). Both are independent of i_{ph}, but dark currents depend on shutter time.

The total average noise of the above sources is $\sigma_{N_i} = \sqrt{\sigma_{SN}^2 + \sigma_r^2 + \sigma_{FPN}^2}$, or derived by [39] as:

$$\sigma_{N_i} = \sqrt{q(i_{\mathrm{ph}} + i_{\mathrm{dc}})t_s + \sigma_r^2} \tag{2.2}$$

Here, i_{dc} represents the signal from dark currents and σ_r^2 is the i_{ph}-independent read noise variance. The signal to noise ratio (SNR) is defined the ratio of the input current to the noise of the total input, $i_{\mathrm{ph}}/\sigma_{N_i}$:

$$\mathrm{SNR}(i_{\mathrm{ph}}) = \frac{i_{\mathrm{ph}} t_s}{\sqrt{q(i_{\mathrm{ph}} + i_{\mathrm{dc}})t_s + \sigma_r^2}} \tag{2.3}$$

Rasnik's spatial resolution is assumed to be directly dependent on the SNR, as its algorithm relies on black-white ratios of the pixels. Typically for pixel image sensors, at low i_{ph}, the SNR is dominated by dark currents and read noise (σ_r), while at high i_{ph} it is increasingly dominated by shot noise. As peak SNR occurs near saturation i_{max}, it is desired to have a high FWC sensor.

Equation (2.3) shows that the SNR consists an i_{ph}-dependent and an i_{ph}-independent part. The i_{ph}-dependent part displays the common $\sim N/\sqrt{N}$ behaviour for shot noise limited systems, as the number of photons N is directly related to the photo-current i_{ph}. The SNR increases linearly when only the i_{ph}-independent part is regarded.

Background light A high ratio between black and white in a Rasnik image is essential for optimal spatial resolution, because then the contours are more pronounced and the Fourier ChessField convolution procedure can be performed with less error. This means that the white squares should be as bright as possible and the dark squares as dim as possible. As Rasnik is a diffraction-limited system, the MTF sets a non-perfect black-white ratio, meaning that with increased input light intensity, the dark squares will also have increased pixel intensities - or background light. Light from the lab also adds to the background light, but its contribution is insignifcant.

Temperature gradients and drift Rasnik transversal measurements are not sensible to heating of one of the three components themselves. Variation in image scaling could occur when one of the components exchanges heat and expands or shrinks, but in principal, transversal shifts cannot result from a temperature variation in any of the Rasnik components themselves.

However, non-homogenieties of temperature in Rasnik's mechanics could create drift in the measured signal, negatively affecting Rasnik's linearity. Thermal variations in Rasnik mounts can be curtailed by operating Rasnik in a temperature controlled environment, and redirecting dispersed heat from the LED and sensor to outside the medium.

2.2. Theoretical performance

2.2.1. Cramér-Rao analysis and pixel noise

CRLB analysis calculation For any estimation of an unknown but determinable parameter, there exists a lower bound for the variance at which this parameter can be distinguished. This lower limit can be calculated, and it is known as the *Cramér-Rao lower bound* (CRLB). Determining the CRLB of a sequence of ChessField images provides a lower precision bound at which Rasnik can measure transversal shifts. This ultimate precision is a result of pixel noise from the sensor and gradient energy in the image.

Rasnik's precision concerns ability to detect shifts in X and Y of a sequence of images. Each image is an array of pixels (x_i, y_i) with a pixel intensity value $\hat{\mu}(x_i, y_i)$. For the 8-bit MER cam $\hat{\mu}$ can take the values $0 < \hat{\mu} < 255$.

The shifts are coordinate transformations, expressed as $x' = x - v_x$ and $y' = y - v_y$. Here, the unknown but to be estimated parameters are v_x and v_y. For a 2D shift estimator, the CRLB variance is expressed as [40]:

$$var(v_x) \geq \frac{\hat{\sigma}^2 \sum_S I_y^2}{det(\mathbf{T})} \qquad var(v_y) \geq \frac{\hat{\sigma}^2 \sum_S I_x^2}{det(\mathbf{T})} \tag{2.4}$$

Where $\hat{\sigma}^2$ is the variance of the pixel image noise of the sensor, $I_x = \frac{\partial I}{\partial x}$ and $I_y = \frac{\partial I}{\partial y}$ are the transversal gradients of an uncorrupted Rasnik image I over the region S of the image, and **T** is the gradient

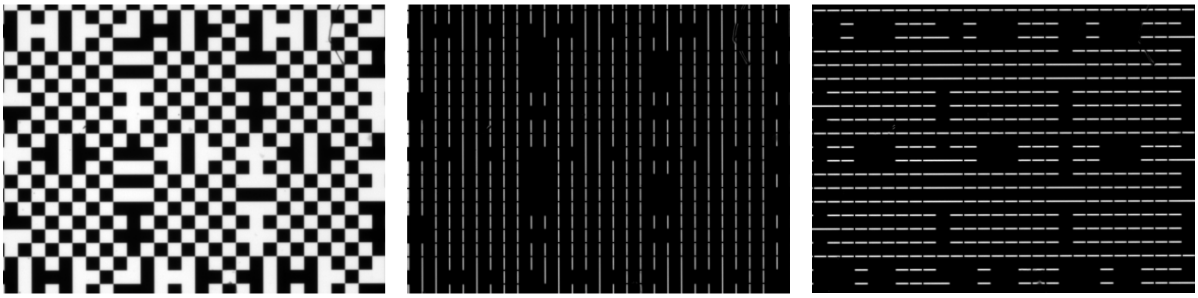

(a) A $N = 150$ averaged Rasnik image $\bar{I}$. (b) The horizontal gradient of $\bar{I}$ squared: I_x^2. (c) The vertical gradient of $\bar{I}$ squared: I_y^2.

Figure 2.3: (a) shows an approximation of an uncorrupted Rasnik image, $\bar{I}$: the average of $N = 150$ images. Horizontal and vertical squared gradients of $\bar{I}$ are depicted in (b) and (c), respectively.

structure tensor that is obtained from the Fisher matrix **F** by $\mathbf{T} = \hat{\sigma}^2\mathbf{F}$. The matrix **T** is expressed as [41]:

$$\mathbf{T} = \begin{bmatrix} \sum_S I_x^2 & \sum_S I_x I_y \\ \sum_S I_x I_y & \sum_S I_y^2 \end{bmatrix} \tag{2.5}$$

and the determinant of **T** is:

$$det(\mathbf{T}) = \Big[\sum_S I_x^2 \sum_S I_y^2 - \Big(\sum_S I_x I_y\Big)^2\Big] \tag{2.6}$$

where, in the case of the ChessField images, the cross-term is insignificant because the gradients are perpendicular: at pixel spots where I_x is large, I_y is approximately zero, and vice versa. By plugging Equation (2.6) (without cross-term) into Equation (2.4), the CRLB dependence on pixel noise and gradient energy reveals itself:

$$var(v_x) \geq \frac{\hat{\sigma}^2}{\sum_S I_x^2} \qquad\qquad var(v_y) \geq \frac{\hat{\sigma}^2}{\sum_S I_y^2} \tag{2.7}$$

Now it is clear that the standard deviation CRLB, $\sigma_{\text{CRLB,x}} = \sqrt{var(v_x)}$, is linearly dependent on the pixel noise of the image sensor, and inversely dependent on the gradient energy in the shift direction. Therefore, pixel noise $\hat{\sigma}$ is desired to be minimal whereas gradients are desired to be maximal. Pixel noise can be lowered by choosing a higher performance pixel image sensor. Gradient energy can be increased by increasing the number of ChessField squares in the image, and by increasing the amount of light falling on the sensor, as that will increase the difference between $\hat{\mu}_{\text{white}}$ and $\hat{\mu}_{\text{black}}$.

Gradients I_x and I_y are derived from an uncorrupted ChessField image I. Kea [37] provided an approximation to any I, with specific white-black intensities $\hat{\mu}_{\text{white}}$ and $\hat{\mu}_{\text{black}}$, by taking the mean of each pixel in an image sequence, resulting in an averaged image $\bar{I}$. An example of an averaged Rasnik image with its two squared gradients is given in Figure 2.3.

To calculate I_x and I_y from the image $\bar{I}$, the Numpy Gradient function is used. This function calculates the derivatives of the pixels by means of a second order approximation:

$$\hat{f}_i^{(1)} = \frac{f(x_{i+1}) - f(x_{i-1})}{2h} + \mathcal{O}(h^2) \tag{2.8}$$

Where f is the function of which the gradients are composed, which is in this case the measured pixel intensity $\hat{\mu}(x_i)$. The pixel index location is denoted as x_i and h is the pixel size of the sensor.

Pixel noise The analysis was performed on images taken with the MER camera, with pixel size $d_{\text{pix}} = 4.8$ μm. Four Rasnik image sequences were taken at different LED light intensities, in order to investigate the influence of the amount of light on the spatial resolution. The same experiment was repeated with the same camera with doubled pixel sizes $d_{\text{pix}} = 9.6$ μm (and thus four times less pixels)

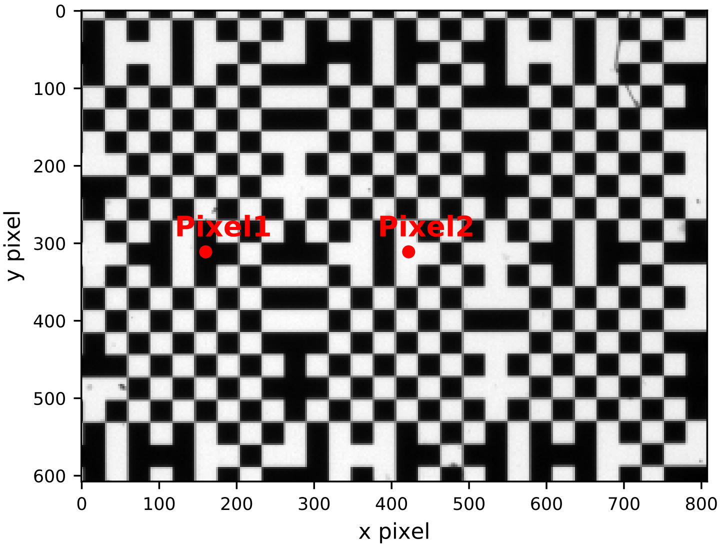

Figure 2.4: Two pixels on an averaged Rasnik image taken with $d_{\text{pix}} = 4.8\ \mu$m. Pixel1 is located at a black spot (170,276) and Pixel2 at a white spot (432,276). For the $d_{\text{pix}} = 9.6\ \mu$m images, pixel values were halved to obtain the same locations in the projected image.

Table 2.1: CRLB results for x and y translations for two pixel sizes of the image sensor.

LED current I	$d_{\text{pix}} = 9.6\ \mu m$		$d_{\text{pix}} = 4.8\ \mu m$	
	σ_x	σ_y	σ_x	σ_y
10 mA	1.2 nm	1.2 nm	0.55 nm	0.56 nm
20 mA	0.58 nm	0.60 nm	0.27 nm	0.28 nm
40 mA	0.42 nm	0.25 nm	0.12 nm	0.12 nm
80 mA	0.13 nm	0.13 nm	0.056 nm	0.058 nm

to explore how precision depends on pixel size. For both experiments, exposure time $t_s = 8$ ms, framerate $f_s = 120$ Hz, and each sequence contained $N = 150$ images.

To examine pixel noise, the pixel intensity $\hat{\mu}$ and its accessory pixel noise $\hat{\sigma}$ were determined at two pixel locations: one at a black spot and one at a white spot, see Figure 2.4. Histograms of measured $\hat{\mu}$'s at both pixels, for both d_{pix} sizes are displayed in Figure 2.5.

Figure 2.5 shows that pixel intensity $\hat{\mu}$ increases proportionally with LED current increase, as expected. What is more, looking at Figure 2.6, the shape of the SNR increase indicates that the pixel noise is shot noise dominated at high $\hat{\mu}$. Rembemer from Equation (2.3) that photon shot noise increases with the square root of the input light, whereas other noise sources from the CCD increase linearly with input light. Quantization rms noise is $1/\sqrt{12} = 0.3$ of a pixel pixel bin, which is a significant noise source at low light intensity, but contributes increasingly less at higher intensities. The contribution of other noise sources, as dark current noise, could not be estimated.

From Figure 2.5 it can be inferred that above $I_{\text{LED}} \approx 135$ mA, the white pixels will start to reach their maximum saturation values of $\hat{\mu} = 255$, and the ADCs of pixels could clip. Measuring above $I_{\text{LED}} \approx 135$ mA, a too large amount of signal will be lost, possibly resulting in non-linear responses, and measuring in these conditions should thus be avoided. At $I \approx 134$ mA, this Rasnik system is already operating at its exremes.

Finally, Figure 2.5 and 2.6 demonstrate that halved pixel sizes result in an approximately doubled $\hat{\sigma}$. This makes sense because halve d_{pix} results in $\frac{1}{4}^{\text{th}}$ input light and thus a doubled $\hat{\sigma}$.

Cramér-Rao analysis results To finally calculate the CRLB, the gradients I_x and I_y of an image, and the pixel image noise variance $\hat{\sigma}^2$ are required. I_x and I_y were determined from the averaged image sequences $\bar{I}$, see Figure 2.3. The pixel image variance $\hat{\sigma}^2$ was derived from the mean pixel intensities $\hat{\mu}_{\text{mean}}$ of each image in the N set of images, having an approximately constant value for each measurement of $\hat{\sigma} \sim 0.08$. The CRLB results are listed in Table 2.1 for $d_{pix} = 4.8\ \mu$m and $d_{pix} = 9.6\ \mu m$.

At $I = 80$ mA, the Cramér-Rao analysis sets a lower bound for a transversal translation of $\sigma_{\text{CRLB}} =$

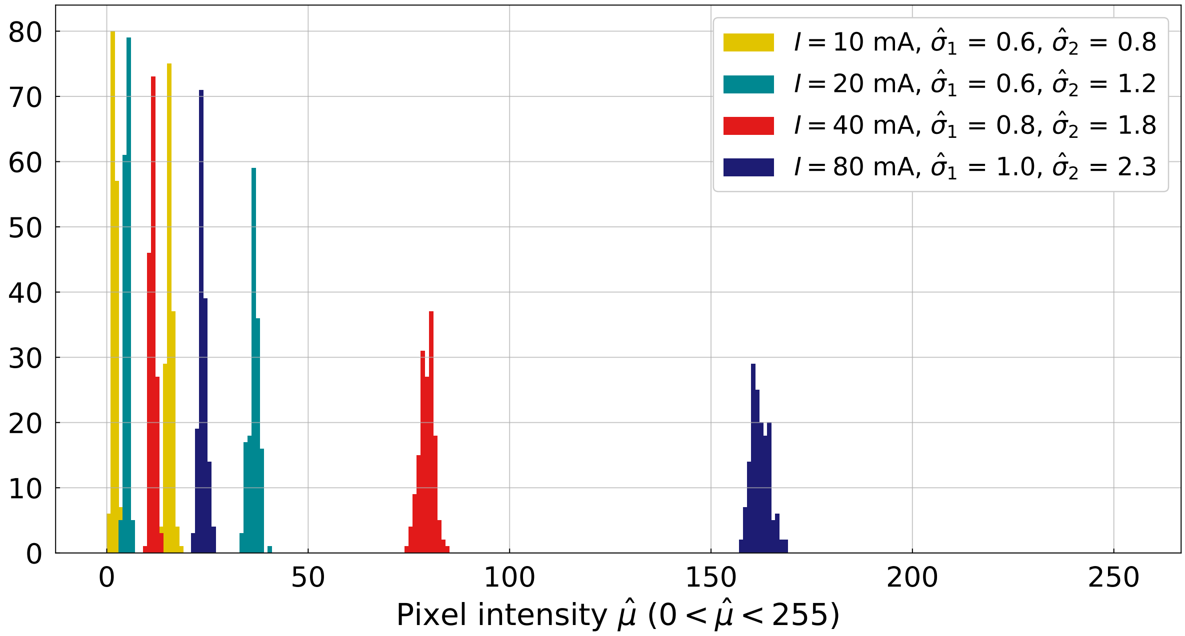

(a) Image sensor pixel size $d_{\text{pix}} = 4.8\ \mu$m

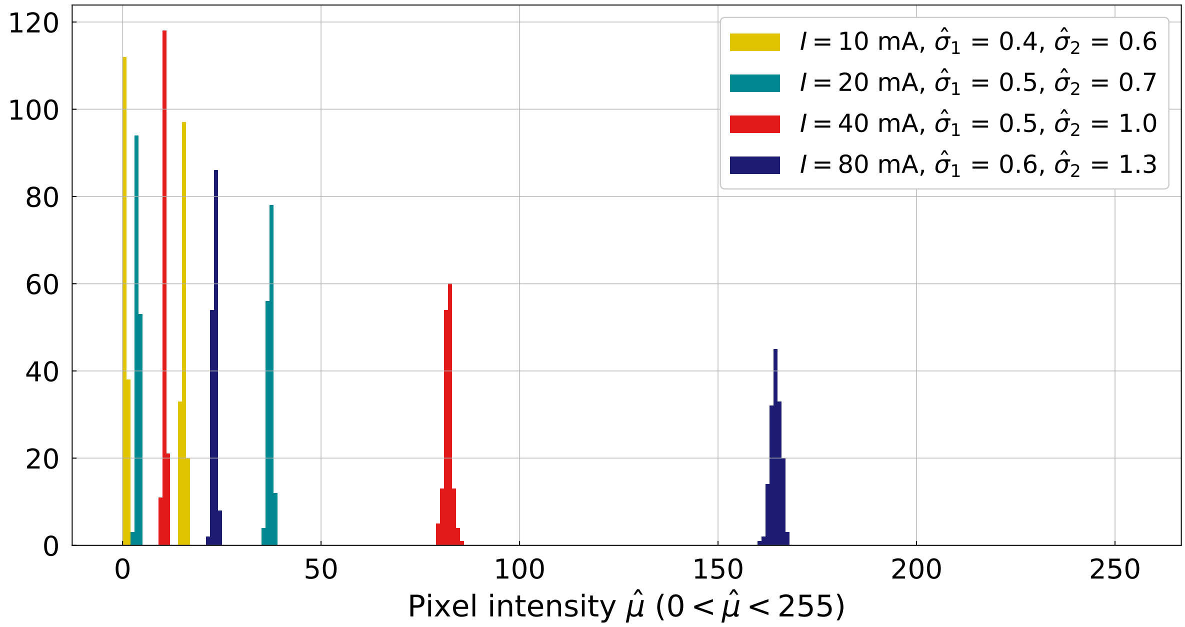

(b) Image sensor pixel size $d_{\text{pix}} = 9.6\ \mu$m

Figure 2.5: Intensities spectra for the MER sensor with two pixel size settings. The colours of the peaks are associated with the LED light intensity. The graphs show two intensity peaks per colour, one at the dark pixel spot (Pixel1), and one at the bright pixel spot (Pixel2), from Figure 2.4.

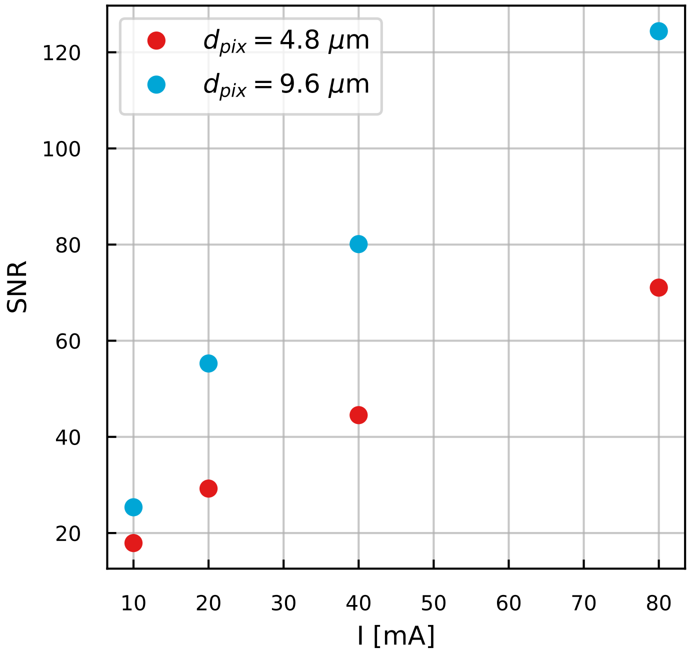

Figure 2.6: SNR's for the two pixel sizes at different LED light intensities, both calculated at Pixel2.

0.13 nm for $d_{\mathrm{pix}} = 9.6\ \mu m$. For $d_{\mathrm{pix}} = 4.8\ \mu m$, results are approximately halve for each measurement, like their SNRs (see Figure 2.6). Presumably, these values are slightly off reality, due to the approach to I with the averaged $\bar{I}$. The Python codes used for this Section are included in Appendix A.

2.3. Measured performance

2.3.1. Previous measurements

Rasnik performance has been studied with the SmallSpan setup [1]. In this setup, the back-illuminated mask (with ChessField squares sized 85 μm) was mounted on translational and rotational actuators, testing Rasnik responses to systematic mask displacements. The distance between the mask and sensor was 160 mm and placed in between was a plano-convex singlet lens with $f = 40$ mm and diameter diaphragm 2mm. The pixel image sensors used were the Logitech C250 and Pike F100B. Both sensors recorded X and Y positions of the mask with a resolution of 60 nm (RMS). This value is the RMS over the time range of the measurement; no spectrum was made to determine the noise ASD. What is more, other measurements of comparable Rasnik systems operating in vacuum, employing different image sensors, have never shown RMS values of below 25 nm [1].

2.3.2. RasMic

A new type of Rasnik system has been developed at Nikhef, called RasMic. In the RasMic design, the central lenswasis replaced with a microscopic objective lens with large aperture, placed near the mask. The large aperture ensured reduced diffraction and increased incoming light on the sensor. However, it possibly also introduces pincushion effects, see Section 2.1.4. As the objective lens enlarges the ChessField patterns, the precision in terms of mask displacement was expected to be improved by a factor equal to the magnification factor of the objective lens. In the first such prototype, a 20x objective was chosen and the performance was therefore expected to improve by a factor of 20: thus from a RMS value of 25 nm from past Rasnik measurements, to about 1.3 nm. The magnification can be selected arbitrarily - a lens with a higher magnification factor should improve precision further. A typical image of RasMic is displayed in Figure 2.7.

To investigate linearity, a Coupled-RasMic system was build from two RasMics. The Coupled-RasMic is a system that by design consists of two parallel coupled RasMic systems, RasMic-1 and RasMic-2, which have their three components mounted to a common base plate, see Figure 2.8. CAM responses from RasMic-1 and RasMic-2 are labelled CAM1 and CAM2. The masks of the two RasMics were glued

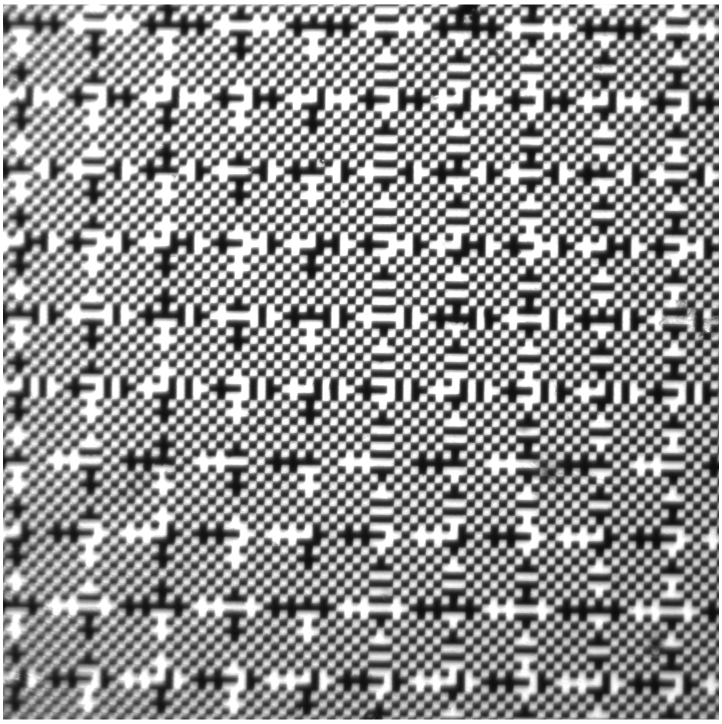

Figure 2.7: A typical RasMic image.

onto a common holder and were separated by a fixed distance of 54 mm. The holder enabled common displacement of the masks in X, perpendicular to the optical axes defined by the coupled objectives and pixel image sensors. The holder could be actuated by a dial gauge when the system was outside vacuum, or a piezo actuator when it was in vacuum. The common X displacement should result in the difference in X-responses of CAM1 and CAM2 to remain constant. The extent to which these subtracted responses remain constant is a measure of linearity of Coupled-RasMic. The common base plate also facilitated actuation in Z, the optical axis of the RasMic systems, in order to focus the images on the sensor.

Performance over a 4.5 mm range First, the Coupled-RasMic system's performance was measured over its full range, which is equal to the size of the masks. Measurements were performed outside vacuum, but an aluminum cover was placed over the complete setup to cover it from variations in the index of air. The masks were actuated in X and Z with a manual dial micrometer gauge operating on the holder. Over a range of 4.5 mm, response in X and Y was measured for each ΔX = 0.5 mm step increase in a 0.6 s time interval, at a maximal frame rate of 30 Hz. Results are depicted in Figure 2.9.

Straight lines ($y = \mathrm{a}x + \mathrm{b}$) were fitted through each set of 20 datapoints. The fits show that, using the dial gauges, the masks were actuated linearly with a precision of $(1 - 1/\mathrm{a}) \cdot 100\% \simeq 0.05\%$ over the full 4.5 mm range (about $2\ \mu$m over 4.5 mm). For both RasMic systems, the residual distances from the fit lines of the mean X-response values are displayed in Table 2.2. Subtracting the residuals of CAM1 and CAM2 should cancel out non-linear actuation by the dial gauge, and this difference is thus a measure of linearity of RasMic. From Table 2.2 it is calculated that the deviation from linearity of this system is about $0.28\ \mu$m per actuation ΔX. As the full experiment was conducted in over 10 minutes, the deviation from perfect linearity is possibly due to thermal drifting effects that typically present themselves in this timescale.

Looking at Figure 2.9 it can be seen that the Y-response lines are not horizontal, which means that the masks were mounted under an angle with respect to the direction of actuation. From the small angle approximation the angle is calculated as:

$$\theta \approx \frac{Y}{X_{act}} \tag{2.9}$$

where X and Y are RasMic's horizontal and vertical displacement responses to an actuation X$_{act}$ from the dial gauge, see Figure 2.10. Filling in the slope parameter of the Y-response from Figure 2.9, called

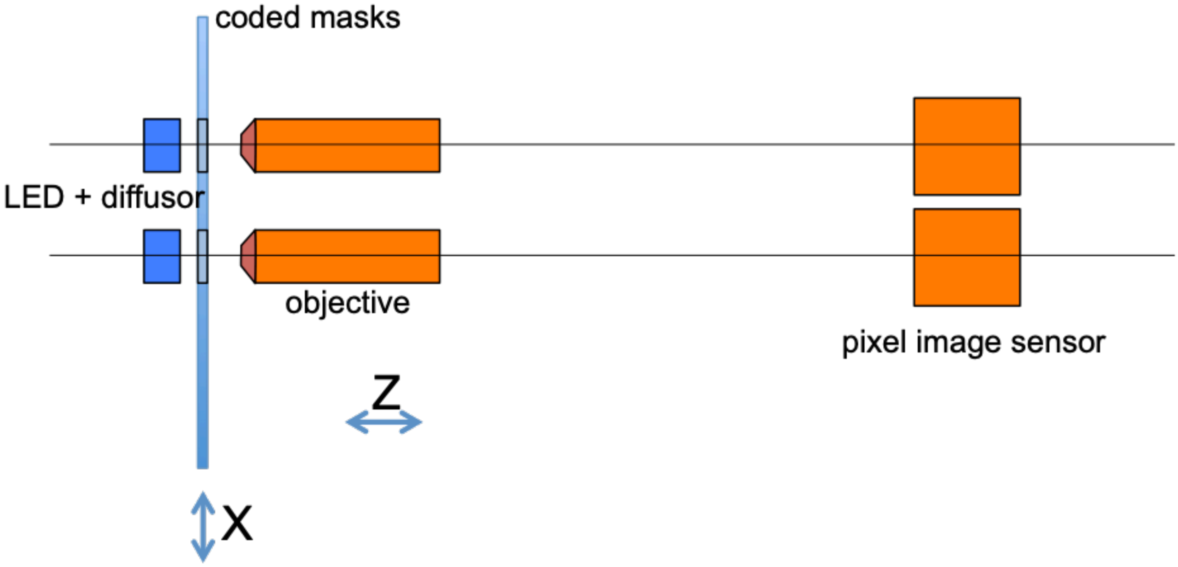

Figure 2.8: A schematic of the parallel coupled RasMic system. Light from two LEDs (StarLED-1W-BL) back-illuminate the chess-field masks, which are glued onto a common holder and separated by a distance of 54 mm. The masks have field squares of 4 μm drawn with 50 nm precision [1]. Microscope objectives (Newport M-20X) placed near the masks form 20 times enlarged images at 180 mm distance from the objectives. There, finally the sensors (Logitech C250) pick up the light and create pixel images of these enlarged mask projections. The light sources, objectives and sensors are mounted on a solid common holder. Image from [1].

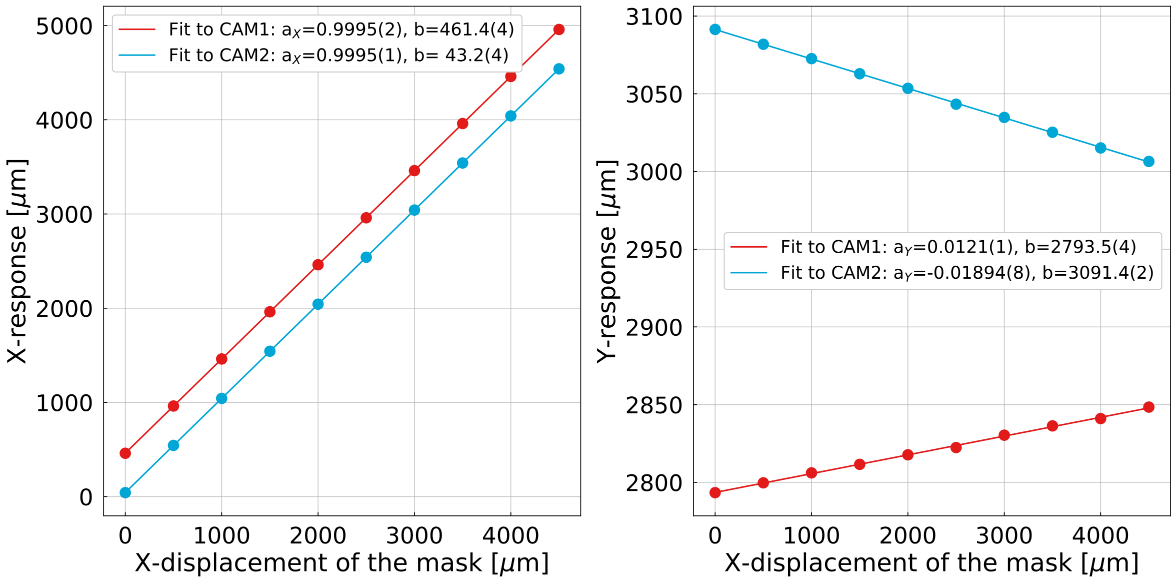

Figure 2.9: X and Y-responses of both RasMic systems to displacement in X with from the dial gauge. Each datapoint contains 20 measurements taken at $f_s = 30$ Hz, with a RMS of about σ = 2-5 nm over the time recording interval of 0.6 s. The slopes of the Y-responses indicate that the masks are mounted under a small angle with respect to the direction of actuation, see Figure 2.9.

Table 2.2: Mean X-response measurements of CAM1 and CAM2, and their residual distances from the fitted line in Figure 2.9. The whole experiment is conducted in 670 seconds, with each position derived from 20 measurements recorded at 30 Hz. The differences of the mean X measurements of Coupled-RasMic are listed in the fifth column. The standard deviation of this difference is $\sigma_{diff} = 0.28\ \mu$m

CAM1		CAM2		Difference
Mean X [μm]	Fit residual [μm]	Mean X [μm]	Fit residual [μm]	$\delta(X_1 - X_2)$
460.1	1.30	42.2	1.00	418.0
961.7	-0.53	543.6	-0.72	418.1
1461.0	-0.08	1042.6	0.01	418.4
1961.5	-0.83	1543.0	-0.67	418.4
2461.1	-0.68	2042.6	-0.50	418.5
2959.5	0.62	2541.0	0.83	418.5
3460.1	-0.19	3041.6	-0.04	418.5
3959.8	-0.15	3541.4	-0.03	418.4
4459.5	-0.13	4041.0	0.09	418.5
4958.5	0.67	4540.8	0.03	417.7

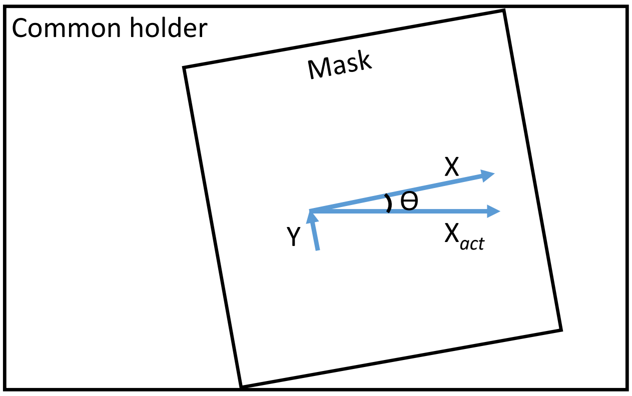

Figure 2.10: The mask under an angle θ with the actuation axis X_{act}.

a_Y, Equation 2.9 yields angles of 0.0121(1) rad and -0.01894(8) rad for CAM1 and CAM2 respectively, as indicated in Figure 2.9.

What is more, the squared sum of the estimated slopes, $M = \sqrt{a_X^2 + a_Y^2}$, represents the proportionality of a Rasnik response to a mechanical actuation X_{act}. The values M for both RasMics are expected to be equal at the level of precision of the scale of the masks, which is specified to deviate less than $5 \cdot 10^{-6}$ from unity [1], two orders of magnitude below the precision of the fits, making their similarity unvisible (see Table 2.3).

All in all, a 0.28 μm deviation from linearity per ΔX = 0.5 mm actuation is shown, which is a factor of $\sim 6 \cdot 10^{-5}$ with respect to the 4.5 mm range.

Performance over a 2 μm range in vacuum Air density variations assumingly deteriorate RasMic's spatial resolution. As the LEDs and sensors disperse heat while in operation, they could be creating local air density variations in RasMic's medium, besides the environmental convection flows, as discussed in Section 2.1.4. In order to investigate whether air density variations limit RasMic's precision, the system was placed in vacuum ($P < 1$ mbar).

Table 2.3: Slope values a_X and a_Y of both RasMic systems, from Figure 2.9, and their squared sums $M = \sqrt{a_X^2 + a_Y^2}$.

	a_X	a_Y	M
CAM1	0.9995(2)	0.0121(1)	0.9996(4)
CAM2	0.9995(1)	-0.01894(8)	0.9997(2)

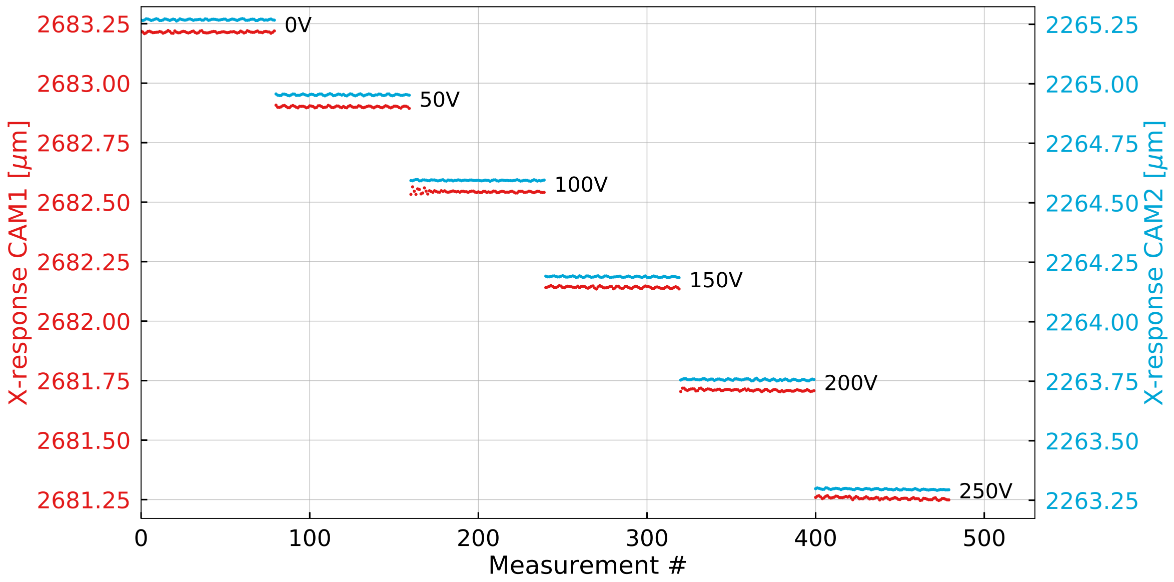

Figure 2.11: X-responses over a 2 μm range, from the RasMic system placed in vacuum. The common mask holder is actuated by a piezo with potential steps of 50V. For each position, 80 measurements were recorded, taking 2.4 s.

To facilitate remote actuation of the masks in vacuum, the dial gauges were replaced with piezo high voltage actuators (PiezoSystemJena HPSt1000/25-15/7). Here, one piezo actuator was used to displace the common holder in Z, in order to focus the RasMic images. This was necessary because the refractive index of air vanishes when the system is pumped down to vacuum, effectively decreasing the focal length of the objective. Actuation in X on the common holder was performed by another piezo, to which potential steps of 50 V were applied, ranging from 0 V to 250 V. As each 50 V potential step results in an actuation of somewhat less than 0.4 μm, a range of about 2 μm is encompassed, see Figure 2.11.

The measurements in Figure 2.11 have a RMS of $\sigma = $ 1.6-5 nm over the time recording interval of 2.4 s. Comparing this with the precision of RasMic in air (Section 2.3.2), significant RMS improvement from operating the RasMics in vacuum has not been shown.

The known non-linearity of the piezo actuator is demonstrated in Figure 2.12, where differences between measured positions vary evidently. In this figure, the sharp peaks in the 2 μm range denote the RasMic systems' high precision.

The linearity of Coupled-RasMic over the 2 μm range was investigated by subtracting X-responses of CAM1 and -2. The mean of each CAM1 peak from Figure 2.12a is subtracted from its CAM2 counterpart (Figure 2.12b). The results of these differences are displayed in Figure 2.13, showing a linearity of about 2 nm per step increase over the 2 μm range - a factor of 10^{-3}.

Thermal effects on linearity Figure 2.13 shows that subtracted X-responses of CAM1 and -2 increase with about $\Delta x = 14$ nm over the full measurement, which was recorded in about 122 seconds in total. The fact that subtracted X-responses of RasMic vary in time, as displayed in Figure 2.13, has raised the suspicion that thermal effects influence the linearity of the system. To study drifting effects, RasMic was placed in vacuum and data was acquired for 9 hours at 1 Hz, without any actuation in X. Results of this measurement are displayed in Figure 2.14. Over the whole measurement, 150 nm scale variations in X-response are visible and it is expected that this was caused by thermal gradients in the setup. However, no temperature measurement was done parallel to the drift measurement, and thus it cannot be concluded with complete certainty that the drifting results from thermal gradients in the mechanics. A strong indication supporting this assumption though is the steep decrease of the measured X-response at 05:45 AM, when heating radiators of Nikhef are switched on.

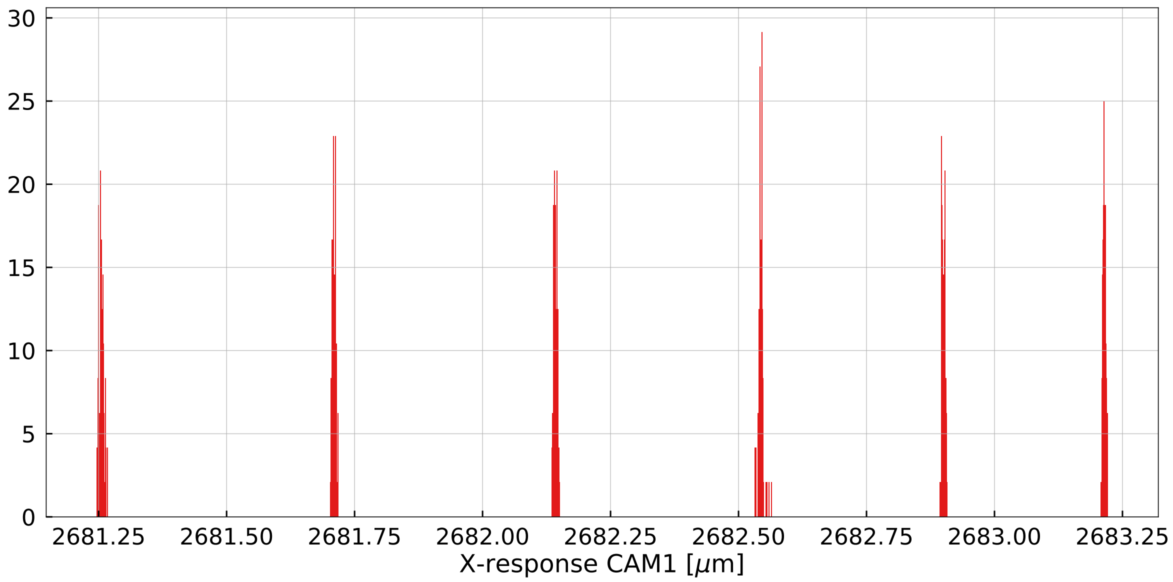

(a)

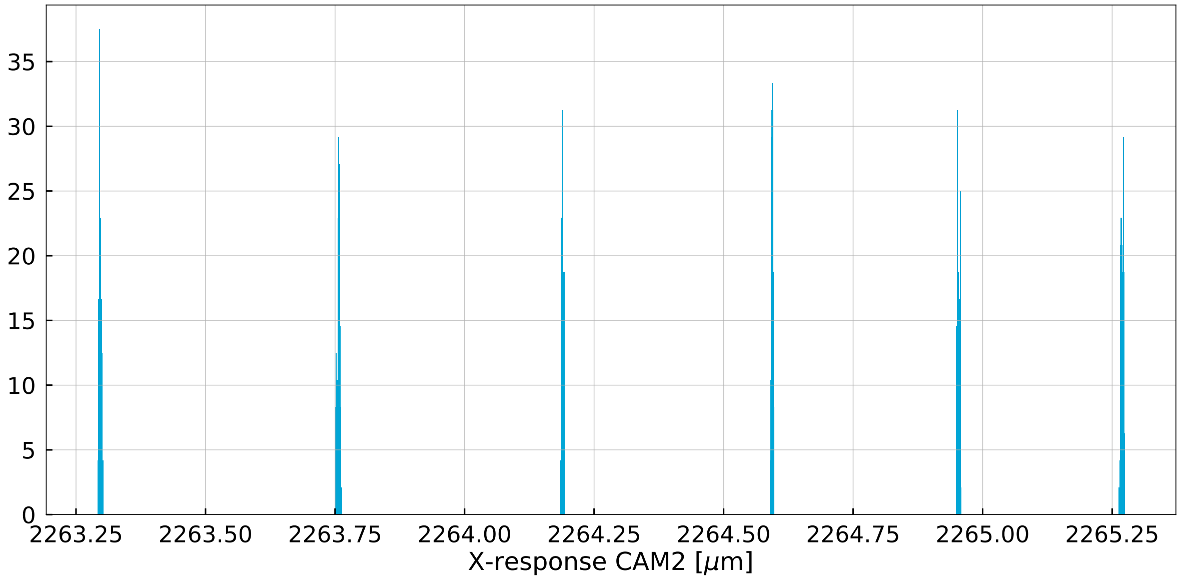

(b)

Figure 2.12: The X-response results of Figure 2.11, presented as histograms with CAM1 in (a) and CAM2 in (b). The sharp peaks comprise 80 measurements and highlight the precision of the RasMics over a 2 μm range. The known non-linearity of the piezo actuation becomes clear from the decreasing distances between measured X-responses, from left to right.

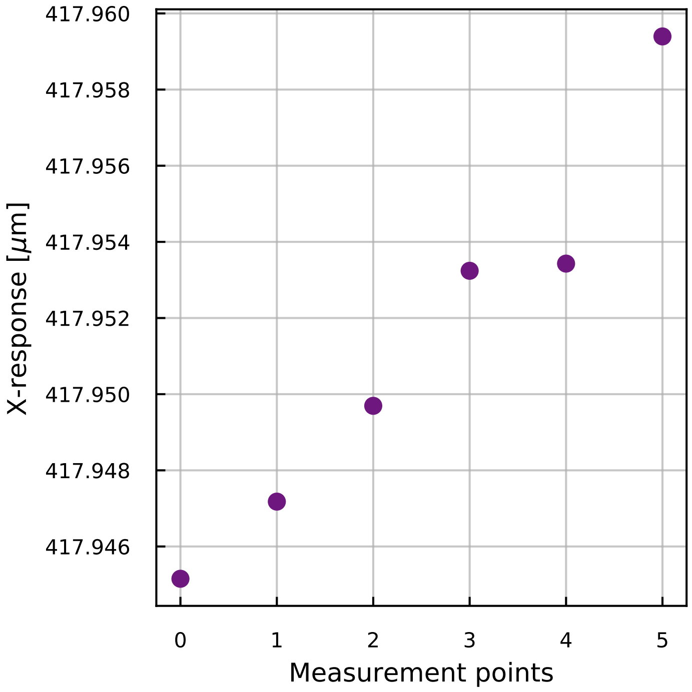

Figure 2.13: Difference in X-responses of the two RasMic systems - the mean of CAM1 minus the mean of CAM2.

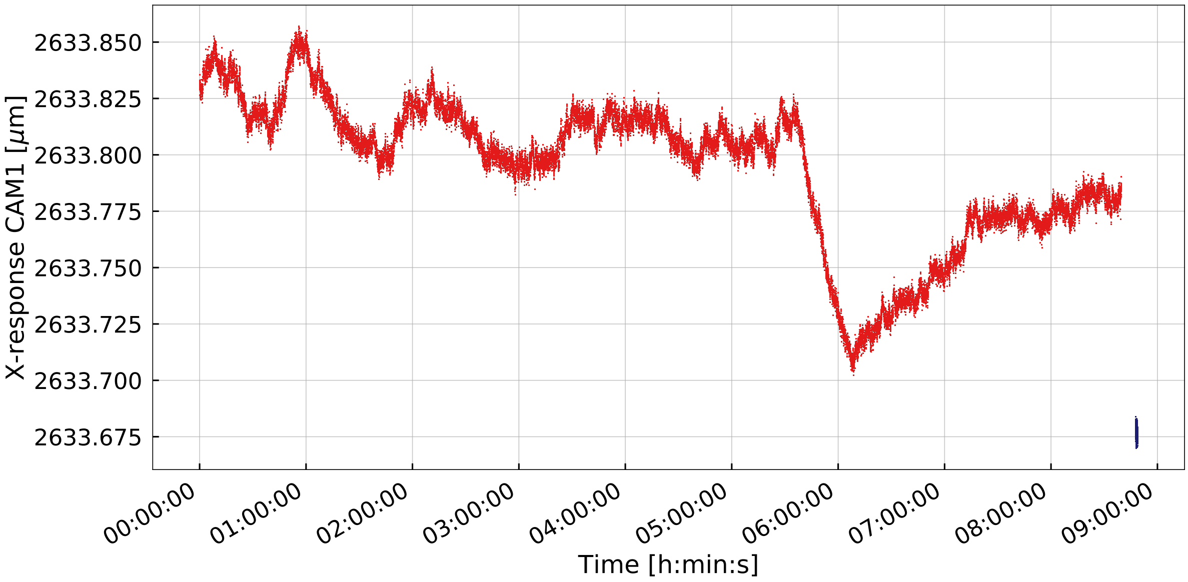

Figure 2.14: X-responses of CAM1 over a range of 9 hours at $f_s = 1$ Hz, without being actuated in X.

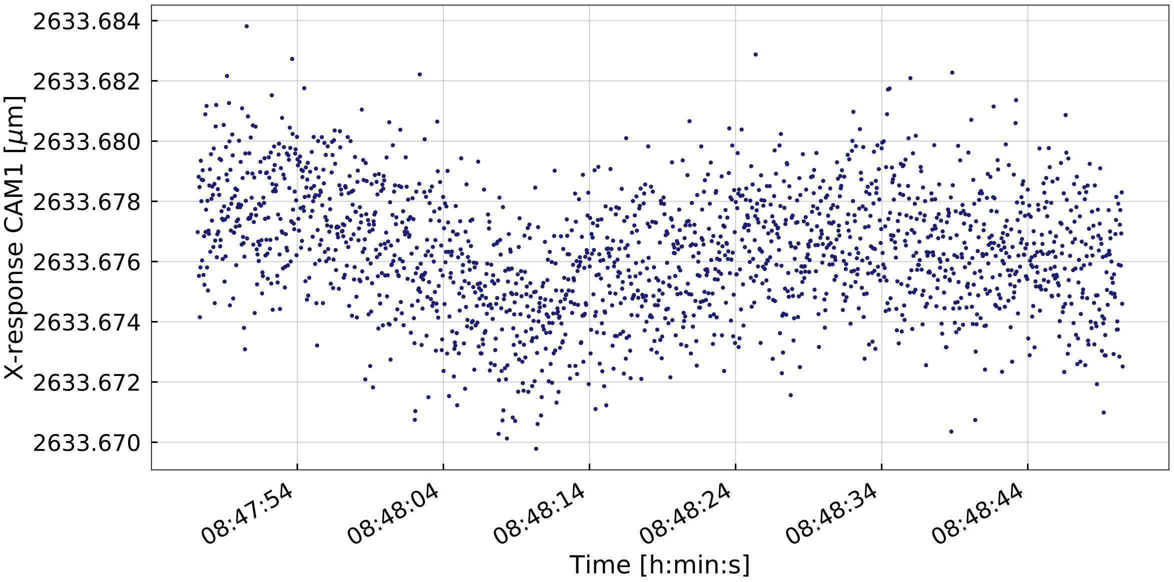

Figure 2.15: The below right corner of Figure 2.14, zoomed in. The 1900 data points are sampled at 30 Hz, recorded in 63.35 s. A histogram of this data is presented in Figure 2.16, and a frequency spectrum in Figure 2.17

The RasMic noise floor At 08:45 the 1 Hz experiment of the previous section was halted shortly (see Figure 2.14), after which measuring continued at a higher sampling frequency of 30 Hz. This part of the sequence is displayed zoomed-in in Figure 2.15, still showing a nm scale drift. A histogram was made of these final 1900 data points (where X-response variation is minimal), over a time interval of 63.35 s, and displayed in Figure 2.16.

The determined $\sigma = 2$ nm is the total, integrated standard deviation of the datapoints over the observable frequency band ($f = 0$ - 15 Hz). However, the instruments characteristic noise floor is determined by of frequency dependent, minimum detectable amplitudes $A_n(f)$:

$$RMS = \sqrt{\int_{f_1}^{f_2} |A_n(f)| df} \tag{2.10}$$

To measure the instrument's A_n's, an ASD plot is made of this data sequence by applying the Welch method to the data (using the scipy.signal.welch package in Python) [42]. This method is used to estimate the power of a signal at different frequencies (PSD).

In time domain, the approach first splits the data stream of the signal into k segments of N points, with a set overlap (usually 50% of N) and applies a window function to them (most commonly the *Hanning window* - a bell-shaped function that smooths out segments towards the edges). Then, in frequency domain, the FFTs of these segments are determined. At each segment k, its FFT Y_k, is calculated from the N long sequence of values y_n as:

$$Y_k = \sum_{n=0}^{N-1} y_n e^{-\frac{2\pi i}{N}kn} \tag{2.11}$$

which are then squared by the scipy.signal.welch function to obtain the PSD. As amplitudes are of interest to resolve RasMic's amplitude noise floor, the square root of data is taken. Results are depicted in Figure 2.17. For the code to determine a spectrum with Welch's method, see Appendix B.

Looking at Figure 2.17, a noise floor of about 450 pm/√Hz is observed. What is more, a small peak at around 5.5 Hz is visible, which might indicate some sort of mechanical coupling with a Rasnik component. Indeed, also inspecting Figure 2.11 from very close, minor oscillations in X-responses become visible. However, no parallel seismic measurement was performed to substantiate these suspicions.

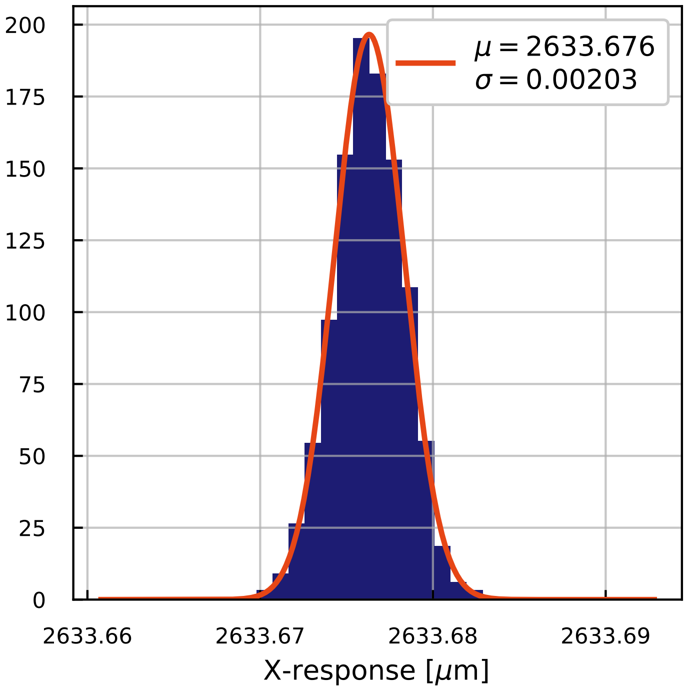

Figure 2.16: Histogram of the 1900 CAM1 X-responses displayed as blue dots in Figure 2.15. $\sigma = 2$ nm is the total standard deviation over a 63.35 s time range.

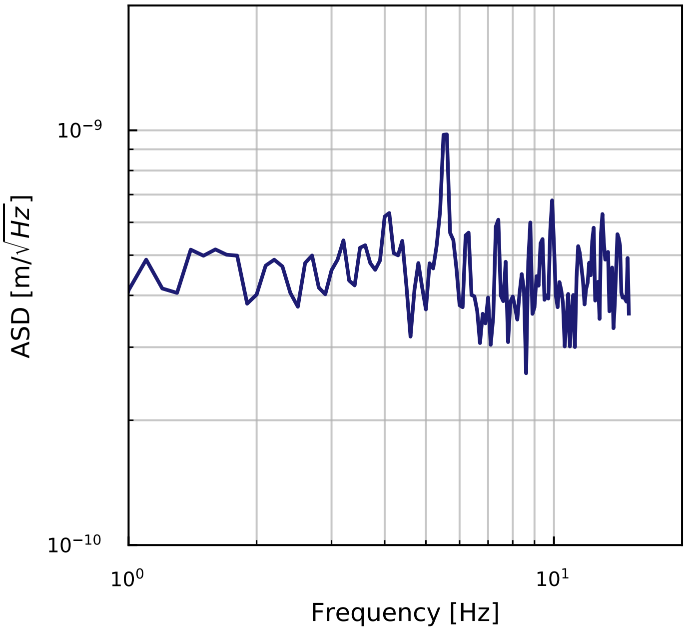

Figure 2.17: Spectrum of the RasMic data displayed in Figure 2.15, using Welch's method. With only 1900 datapoints, the FFT segments consisted of only $N = 95$ datapoints.

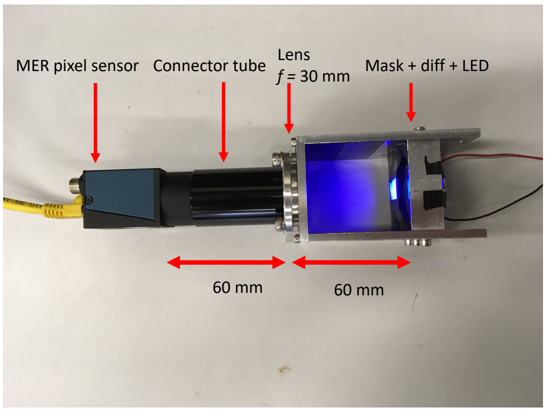

Figure 2.18: A compact, solid Rasnik system, with mask-lens and lens-cam distance of 60 mm. The LED used is the Luxeon Z, colour Royal Blue and the pizel image sensor is the CMOS MER-051-120GC. The focal length of the lens is 30 mm.

What is more, the 5.5 Hz peak might be deceiving due to *under-sampling* effects, as a result from the low sampling rate of the RasMic Cams ($f_s = 30$ Hz). Under-sampling arises when the frequency of interest is above the *Nyquist frequency*, the maximum observable frequency, which is half the sampling frequency of a sensor. Under-sampling occurs when the sensor's sampling frequency is not high enough to measure the signal, and the taken samples are indistinguishable from samples of a low-frequency alias of the high-frequency signal. The Nyquist frequency of RasMic was about 15 Hz, leaving every frequency above it to be measured as a deceiving low-frequency alias. To extend the observable frequency range, an image sensor with a higher sampling frequency of $f_s = 120$ Hz was used in following experiments.

2.3.3. Solid Rasnik

A new Rasnik construction was made that was 1) mechanically robust to counter mechanical couplings and 2) had a higher framerate to extend observable frequencies. The back-illuminated mask, lens and pixel image sensor were mounted solidly to a common frame, spanning about 120 mm. The sensor and lens were attached via a cylindrical tube for precise alignment and to provide cover for local variations in the medium's index of refraction. The mask was back-illuminated with a LED source that could handle currents of several hundred mA. The image sensor had pixel size $4.8\ \mu$m and max frame rate $f_s = 120$ Hz. As the MER camera cannot operate at f_s whilst using its smallest pixel size, it was set to use four merged pixels as one to create $d_{pix} = 9.6\ \mu$m pixels. A framerate of 120 Hz extended the observable spectrum from 15 Hz (of the RasMic experiments) to 60 Hz. A picture of this setup is depicted in Figure 2.18. Three experiments were conducted with this Rasnik, to acquire understanding for the effects of LED intensity, sampling frequency and density variations on the system. All results shown in this section are Rasnik X-responses; the Y-responses are highly similar.

Input light dependency of Rasnik resolution Rasnik is limited by diffraction and pixel noise. It is expected that Rasnik's spatial resolution increases with increased SNR, when black-white transitions are more pronounced. This should translate into improved Rasnik resolution from an increased amount of light falling onto the image sensor. This hypothesis was researched by taking ASD's of ~30 minute long Rasnik measurements at $f_s = 120$ Hz, at different input light strengths, as varied with current through the LED. The ASD's were calculated from Welch's method, see Section 2.3.2. In this experiment, the lens and mask are shielded with plastic covers to minimize density variations in the medium. Results are shown in Figure 2.19.

From Figure 2.19 it is confirmed that Rasnik operated at its pixel noise limit, and that spatial resolution was a direct consequence of the SNRs of the pixel content. As discussed in Section 2.1.4, the SNR of pixels is a consequence of different noise sources, depending or not on the amount of input light. A model that takes into account input light dependent and -independent noises is:

$$A_n = \sqrt{\frac{a}{I_{\text{LED}}} + \frac{b}{I_{\text{LED}}^2}} \tag{2.12}$$

because $I_{\text{LED}} \propto i_{\text{ph}}$. In this model, the parameter a is in units of [Am^2/Hz] and b in [A^{2}m^2/Hz]. The

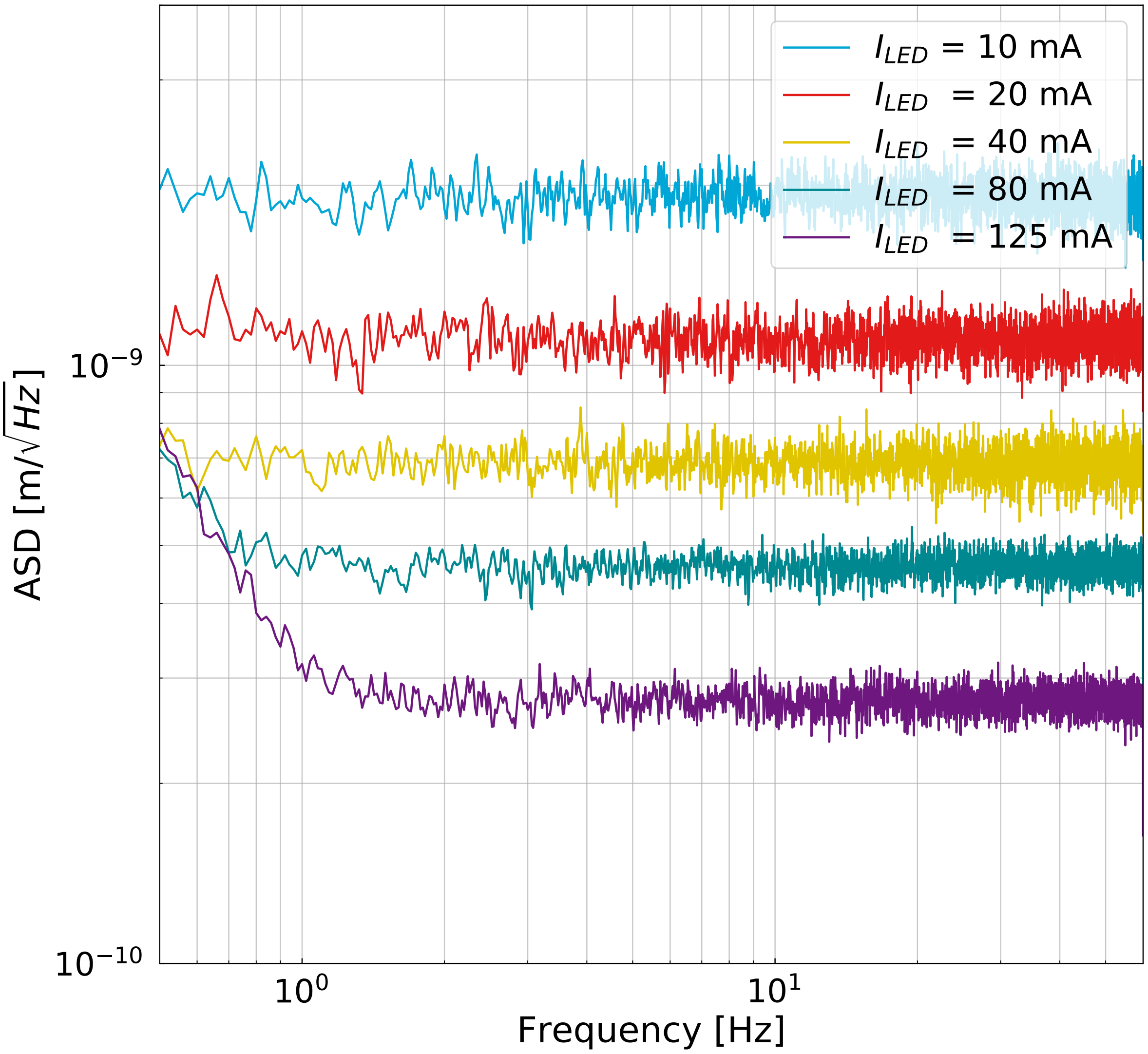

Figure 2.19: Noise resolutions at different LED light intensities. Above I = 140 mA, the white pixels are saturated ($\hat{\mu}$ = 255) and therefore measurements are taken at LED currents below this value.

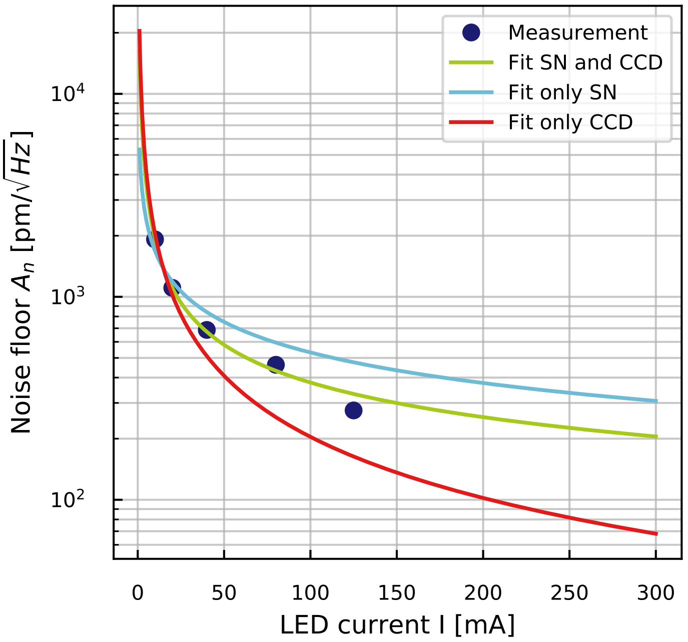

Figure 2.20: Noise floor versus input light, with three different functions fit to the datapoints. The red line takes into account only noise independent of input light (CCD noise), whereas the blue line takes into account only shot noise. The green line accounts for both these effects.

LED current I	Measured A_n	Modelled lower bound σ_x
10 mA	1.9 nm/√Hz	1.2 nm
20 mA	1.1 nm/√Hz	0.58 nm
40 mA	0.68 nm/√Hz	0.24 nm
80 mA	0.46 nm/√Hz	0.13 nm

Table 2.4: Measured and modelled Rasnik resolution.

factor $\frac{a}{I_{\text{LED}}}$ is the photon shot noise contribution and $\frac{b}{I^2_{\text{LED}}}$ represents all other noise sources from the CCD, which are independent of the light input. From Equation (2.12) it is seen that the shot noise contribution should become increasingly dominant for higher LED currents.

This model is fitted against measurements for different LED light intensities, see Figure 2.20, with $a = 1.2 \cdot 10^7$ Am^2/Hz and $b = 2.5 \cdot 10^8$ A^{2}m^2/Hz. The relative error on parameter a is 13.9% and on b 9.8%. For comparison, two extra cases were considered: one where $b = 0$ (only SN) and one where $a = 0$ (only CCD noise), see the red and blue lines in Figure 2.20. They have fit parameter errors of 16.2% and 14.0%, respectively. From these fits it seems that A_n is indeed a result of both shot noise - dependent on the input light - and CCD noise (read noise, quantization noise, dark current noise) - independent of the input light.

Figure 2.20 shows there is expectedly still significant room to lower A_n from higher input light intensities. For that reason, it is suggested that in following research on Rasnik performance, image sensors should be used with high FWC, enabling the possibility to increase the maximum number of photons per pixel, improving the SNR and thus resolution. Other suggestions to lower pixel noise contributions are: choosing a CCD with larger bit-depth to lower quantization noise, and cooling the pixel sensor to reduce thermally excited dark current noise.

Folding effects Noise measurements were also conducted in shielded configuration and at $I = 130$ mA, but with varying sensor framerates, see Figure 2.21. It is observed that spatial resolution improves with increasing sampling rates. This is explained by a digital effect called *folding*. With folding, the white noise above the Nyquist frequency is aliased (or *folded*) as white noise into the observable spectrum, adding layers of noise on top of A_n. By increasing f_s, the amount of folded white noise decreases and resolution is improved with a factor $\sqrt{f_s}$, see the green inversed square root line in Figure 2.21b. The best spatial resolution of 270 pm/√Hz is therefore measured at highest framerate $f_s = 120$ Hz.

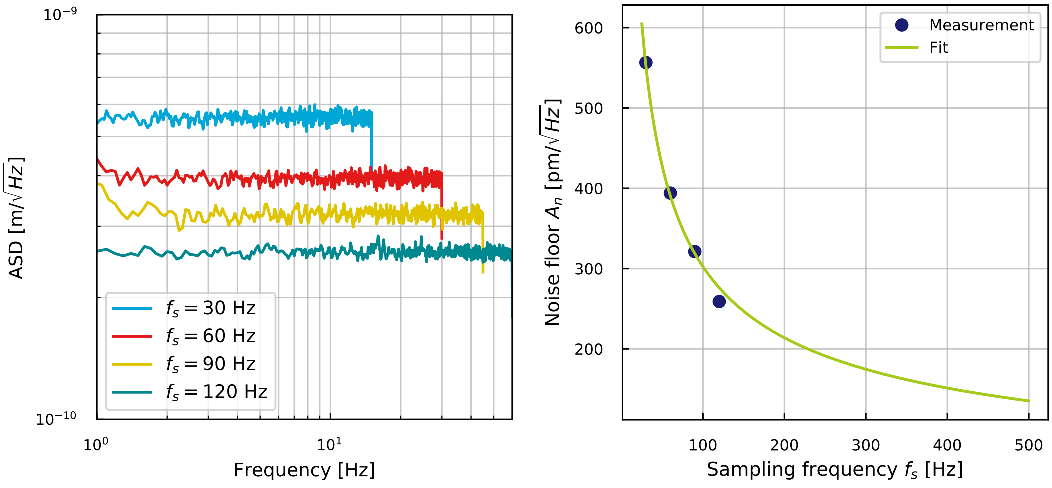

(a) Amplitude Spectral Densities

(b) Noise floor levels A_n

Figure 2.21: In a) a spectrum of Rasnik data sampled at different sampling frequencies f_s is shown, and b) depicts the noise floor A_n at increasing sampling rate f_s. An inversed square root is fitted to the datapoints with a relative error of 1.3%. All measurements were conducted in shielded setup with $I = 130$ mA.

For analog signals folding is prevented by using frequency cutoff filters before the signal is send to an ADC. However, as Rasnik signals are digital (the ADC is inside the pixel image sensor) frequency cutoffs are not straightforwardly applied. One solution would be to place an anti-aliasing filters are in front of the CCD [43]. Another, perhaps simpler, solution to exclude folded white noise is to use an image sensor with higher sampling frequency, improving resolution as indicated by Figure 2.21b.

Density variations in the medium and LF resolution In Section 2.3.2 it was noted that variations in the medium had no significant effect on the integrated RMS of RasMic data. However, data was taken in a short time interval and at low f_s, making their comparison not sound. Density variations are nonetheless expected to affect the Rasnik's amplitude noise floor A_n at low frequencies. Therefore, an experiment was conducted where one measurement was performed with the medium shielded with plastic covers, like in previous experiments, and one where no shielding was present. The results are displayed in Figure 2.22, where a clear difference in the time data is visible, with large irregularities and peaks for not shielded Rasnik X-responses. In frequency domain, these irregularities translate to an A_n increasingly reduced from $f = 11$ Hz to frequencies below, see Figure 2.23.

The shielded Rasnik spectrum in Figure 2.23 shows that below $f = 1$ Hz, resolution deteriorates drastically to about 30 nm/$\sqrt{\text{Hz}}$ below $f = 0.01$ Hz. This is expectedly partly due to non-perfect shielding of Rasnik. Still many gaps and splits allowed air from the laboratory's environment to enter the medium and create distortions in the direction of light. What is more, heat exchange between the sensor/LED and the medium possibly facilitates additional convection flows. Therefore, placing the setup in vacuum and in a temperature controlled laboratory environment, where density variations are minimized, Rasnik LF resolution is expected to increase. For such an experiment CCD image sensors should be used, as they disperse less heat than CMOS sensors, and heat from the LED and sensor should be redirected towards outside the medium. These measures could eliminate density variations and enable enhanced resolution also at low frequencies. What is more, the drifts observed in the RasMic 9 hour experiment in vacuum, shown in Figure 2.14 in Section 2.3.2, indicate that also thermal heating of mechanics might be responsible for LF resolution reduction.

2.4. Conclusions

Compared with previous research, a new way of interpreting spatial resolution from a Rasnik measurement was established. Instead of taking the standard deviation of a set of Rasnik X-responses, which expresses the RMS integrated over the time interval of the measurement, a spectral density plot was construed in which the flat line represented the Rasnik white noise floor. This explained the discrep-

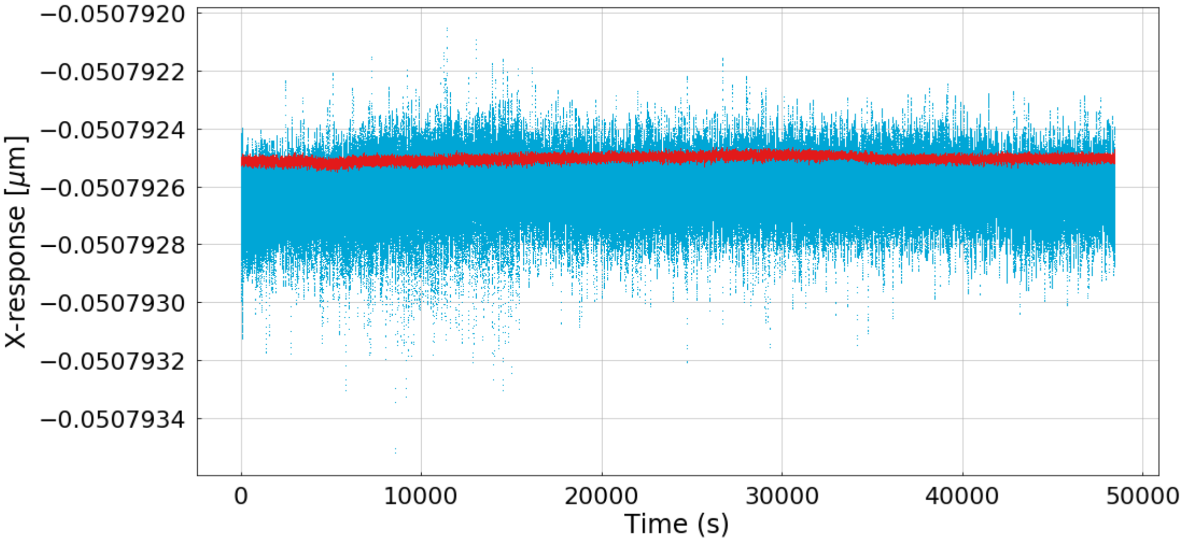

Figure 2.22: X-response datapoints of a shielded (red) and not shielded (blue) Rasnik, clearly revealing light path distortions in the medium. Images were recorded with $I_{\mathrm{LED}} = 135$ mA.

Figure 2.23: Spectrum of the data from Figure 2.22, for a shielded Rasnik and a not shielded Rasnik. To gain LF spectral resolution, data was taken at $f_s = 120$ Hz for about 15 hours, and sample lengths of 833 seconds were taken for the ASD.

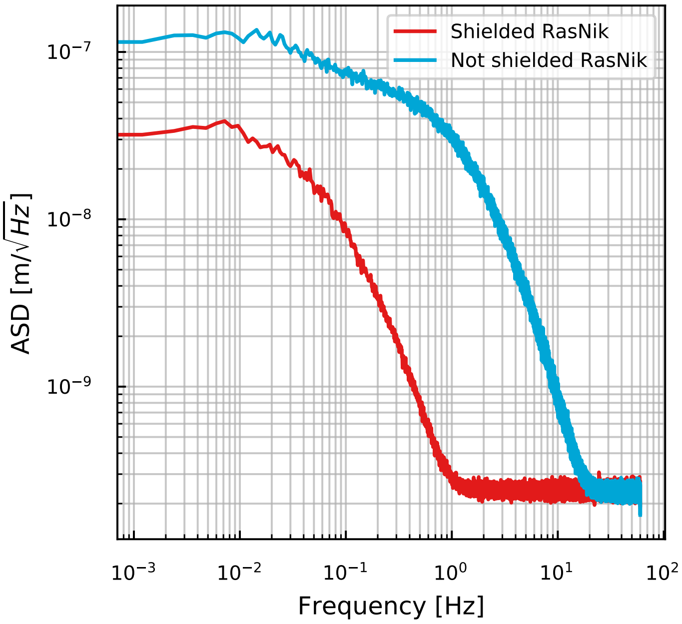

ancy between the CRLB modelled noise levels and the ~ 25 nm noise resolutions obtained in previous experiments. These measurements were in fact resolutions of Rasnik, integrated over the entire observable frequency band, where at lower frequencies influences from the environment induce noise far above the resolution floor. This way of interpreting data was only established after RasMic experiments were conducted, and only one spectrum of (a small sample of) RasMic data could be taken.

The RasMic experiments showed that high RMS precision of $\sigma =$ 2-5 nm can be obtained over an arbitrary large range (4.5 mm in this case). What is more, the 20x enlarged RasMic images showed RMS improvement of indeed about a factor 20 with respect to previous Rasnik experiments. The free resolution gain from optical magnification thus remains an attractive prospective, and research on a small and robust RasMic system (comparable to the Solid Rasnik) with varying magnification objectives, could indeed reveal improved spectral resolution floors.

Coupled-RasMic revealed that RasMic's linearity, which was established to be about 280 nm over a 4.5 mm range, and a few nm over 2μm range, was possibly reduced by thermal effects in the mechanics. This is not an intrinsic defunct of the system and can be countered by placing the setup in temperature controlled environment, where heat from the LED and image sensor is isolated.

Experiments with the $f_s = 120$ Hz Solid Rasnik showed that Rasnik is, as expected, pixel noise limited. More profoundly, the pixel noise is presumably dominated by shot noise at high input light intensities. A maximal resolution of $A_n = 270$ pm/$\sqrt{\text{Hz}}$ is achieved above 1 Hz. Gaining resolution from more light halted though when the light pixels in the ChessField squares reached their maximum values of $\hat{\mu} = 255$ (which should be avoided). For that reason, in future Rasnik research it is advised to employ CCD sensors with high FWC, that need a larger amount of photons before their maximum saturation point is reached. Moreover, the CCD of choice should also have higher bit-depth to lower quantization noise.

Distortions in the light path due to density fluctuations in the medium were shown to cause shifting images on the sensor, and create distorted Rasnik X- and Y-responses. Especially at frequencies below $\sim$ 10 Hz, these distortions were responsible for heavily deteriorated resolution. With a simple plastic cover, this effect was significantly reduced at $f =$ 1-10 Hz. However, it is expected that the ASD noise floor can become flat also at below 1 Hz in a vacuum setup with a low-heat dispersing CCD sensor. The dispersed heat from LED and sensor should be guided to outside Rasnik's medium.

In Section 2.2.1 a precision lower bound $\sigma_{CRLB} = 0.13$ nm for Rasnik was calculated for a sequence of images taken at $f_s = 120$ Hz and $I = 80$ mA. The measured resolution of Rasnik at these parameters was determined to be $A_n = 0.46$ nm/$\sqrt{\text{Hz}}$, close to the model, but still somewhat less than a factor 3 off, possibly due to the fact that the perfect, non-corrupted image I, was approached by an averaged image $\bar{I}$ in the model.

Lastly, the aliasing of white noise from above the Nyquist frequency was shown to reduce resolution. Because of *folding*, the measured lower noise floor of $A_n = 270$ pm/$\sqrt{\text{Hz}}$ is therefore not the intrinsic lower bound of Rasnik. Folding can simply be coped with by using a sensor with a higher framerate f_s, or using a anti-aliasing filter in front of the CCD.

To conclude, a spatial resolution of $A_n = 270$ pm/$\sqrt{\text{Hz}}$ above $f = 1$ Hz was obtained with Rasnik. The measured spatial resolutions were close, but still a bit above value the modelled performance, based on the Cramér Rao analysis, possibly due to an estimation in the model. Using a high FWC, large bit-depth, high framerate CCD image sensor in vacuum, penetrating 100 pm/$\sqrt{\text{Hz}}$ resolution seems highly feasible. Further enhancing reslution by using a microscopic objective with 100-400x enlargement, Rasnik should reach pm/$\sqrt{\text{Hz}}$ resolution at large frequency range (from 0.01 Hz to several hundred Hz) and with an arbitrary large dynamic range.

2.5. Future plans

High performance CCD-Rasnik The possibility of approaching pm/$\sqrt{\text{Hz}}$ noise levels cause Rasnik to be a promising GW sensor in different applications. However, before any application is made with Rasnik for GW experiments, first it is planned to reach the pm/$\sqrt{\text{Hz}}$ resolution in the laboratory. Therefore, resolution and linearity experiments are planned for a Rasnik system in vacuum, with a high FWC, high framerate, large bit-depth CCD image sensor, and a strong microscopic objective as lens.

RasTilt: a tiltmeter for LF control One application of Rasnik as a displacement sensor is to use it in a tiltmeter. This concept is called RasTilt. Tiltmeters complement accelerometers for low frequency active feedback control of the suspensions in GW detectors. The readout sensors of tiltmeters under study are often interferometers [44], which could reach pm/$\sqrt{\mathrm{Hz}}$ resolution, but are renown for complicated alignment and are relatively expensive. Therefore, at the moment, as a tiltmeter readout a Rasnik cannot surpass an interferometer in noise, but developing a tiltmeter with Rasniks would be considerably simpler and cheaper.

Rasnik as Optical Lever for angular control Using a Rasnik system as Optical Lever for active control of the mirror angular suspension modes is promising. With Rasnik resolution measured in this research, angular measurements could already be done more than an order of magnitude preciser than the Optical Levers currently employed at GW detectors, with nrad/$\sqrt{\mathrm{Hz}}$ over 2 m arm span. With higher precision sensors angular control can be done more aggressively. Thus, when few pm/$\sqrt{\mathrm{Hz}}$ resolution is reached, angular control can be done far more aggressively, lowering GW detector's angular modes noise at LF significantly.

3

The monolithic folded pendulum accelerometer

As second generation GW interferometers have gained sensitivity and low-frequency detections, which demand high precision feedback mechanisms, have become increasingly interesting, better performing custom made inertial sensors are under development, as the monolithic folded pendulum (FP) accelerometer at Nikhef [2, 45].

The FP mechanical model was first proposed in 1993 by Blair et al. [46]. The geometry of this model was a *Watt-linkage*, invented by James D Watt in 1873 [47]. By making a Watt-linkage under gravitational restoring force, Blair et al. [46] invented the pendulum-anti-pendulum combination for LF vibration isolation. Bertolini et al. [45] adjusted the invention to an inertial sensor, the mechanics of which was carved out from a single piece of high-strength low-creep metallic alloy, reaching nanometer rms noise integrated over a 0.01-150 Hz frequency band [45]. The mechanics of this device departed from the Watt-linkage geometry by placing the legs closer to each other. This instrument is the first in line of the FP accelerometers. Improvements have been made ever since, both to the mechanics and to the readout. For instance, Acernese et al. [48] mapped the mechanics of the FP accelerometer with the goal of making it attractive for in field applications.

In efforts to combine Virgo-style passive damping with LIGO-style active damping in the multi-stage suspensions for Virgo upgrades and for the future Einstein Telescope, improvements to the FP accelerometer led to the latest published results that show displacement sensitivities of up to $8 \cdot 10^{-15}$ m/$\sqrt{\text{Hz}}$ from 30 Hz and onwards [2]. However, such a figure is still a factor of 3 above the sensor's modelled performance and it can thus be improved even further.

A sizeable part of this research consisted in thoroughly investigating the thermal noise of the instrument's mechanics, which limits sensitivity at low frequencies. After that, the accelerometer's performance was re-evaluated by testing it on the ultra-low vibration isolation platform available at the institute [49].

Section 3.1 deliberates on the mechanics and operation principles of the accelerometer. Then, in Section 3.2 thermal noise in the instrument from different damping mechanisms is evaluated by measuring quality factors. A newly designed feedback actuator is modelled in Section 3.3 and the consequent improvement with respect to thermal noise is discussed. The interferometer readout part is discussed in Section 3.4, where also approaches to fully diminish laser intensity fluctuations are elaborated on, in order to attempt to reach the shot noise limit. In Section 3.5 the accelerometer feedback loop is characterized and final noise measurements at the vibration isolation platform are discussed.

3.1. Accelerometer mechanics

3.1.1. Mechanical model

A rough model to solve the kinematics of the FP accelerometer is sketched in Figure 3.1. A simple pendulum of mass m_1 and length l_1 is connected via a massless rigid beam to an inverted pendulum

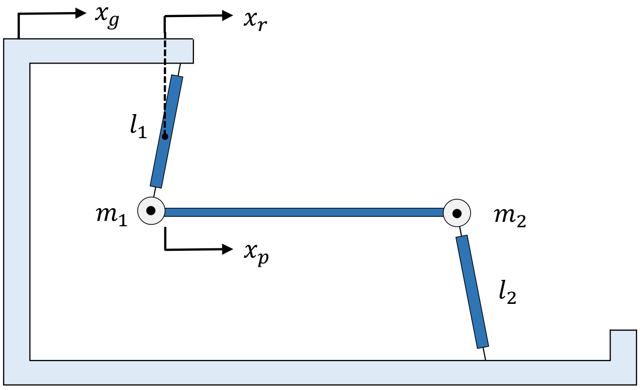

Figure 3.1: Crude mechanical model of the accelerometer, where the center of mass depends on the pendulum masses.

(IP), that suspends a mass m_2 with a leg of length l_2. Both pendula arms are assumed massless and rigid, and connected via flexures.

The restoring force on the pendulum is given by Hooke's Law:

$$F_r = -kx \tag{3.1}$$

It is a sum of both the gravitational restoring force and the elastic restoring force from the flexures: $k = k_g + k_{el}$. As the flexures are very thin, the main restoring force is gravitational. From a small angle approximation the gravitational spring constant is given as:

$$k_g = m_1 g/l_1 - m_2 g/l_2 \tag{3.2}$$

and the natural frequency of the system follows from $\omega_0 = \sqrt{k/M}$, where $M = m_1 + m_2$:

$$\omega_0 = \sqrt{\frac{m_1 g/l_1 - m_2 g/l_2}{M} + \frac{k_{el}}{M}} \tag{3.3}$$

Now it becomes clear that k can be tuned to arbitrary low values by redistributing the center of mass (COM) and leg lengths such that the first term in the square root nearly cancels the second. The oscillator remains stable when:

$$m_1/l_1 - m_2/l_2 \geq -k_{el}/g \tag{3.4}$$

which is in fact $k_g \geq -k_{el}$, or $k \geq 0$. This makes sense because a negative k would result in a positive - and thus *non restoring* - force in Equation (3.1), making the pendulum instable.

This model is a crude approximation of reality: it only validly describes a real FP when equivalent masses and lengths are used to take into account the mass distribution and the moment of inertia of both pendula arms. A more accurate model is derived by Liu et al. [50] from the systems Lagrangian, taking also into account the pendula arms' masses and moments of inertia. The resulting natural frequency of this model essentially says the same though: it can be tuned by redistributing weights between the two pendula arms.

Next to the restoring force, viscous damping forces act on the proof mass. This damping is often described as energy dissipation from collision with air molecules, hence the term *viscous*. But more generally, it accounts for damping forces that are proportional and opposite to velocity:

$$F_{viscous} = -c\dot{x} \tag{3.5}$$

Equating the restoring force F_r, the viscous force $F_{viscous}$ and a harmonic exciting force $F_{harmonic}$ gives:

$$F_{tot} = F_r + F_{viscous} + F_{harmonic} \tag{3.6}$$

which results in the general equation of motion of a viscously damped oscillator:

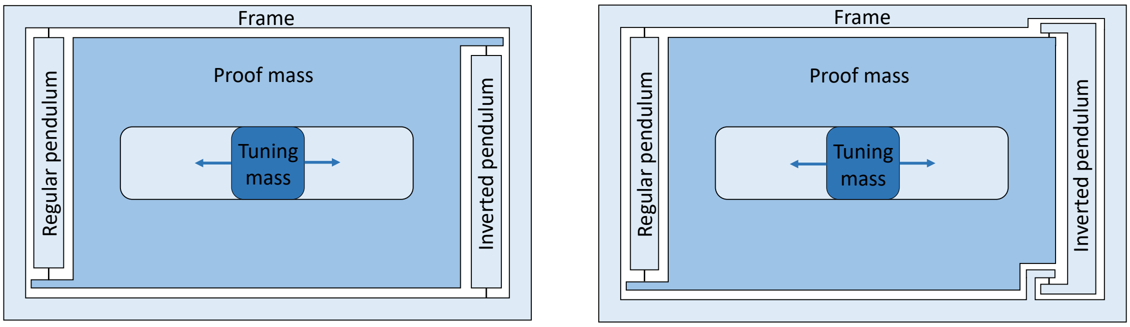

(a) The titanium accelerometer design

(b) The aluminum accelerometer design

Figure 3.2: Mechanical design of the titanium and aluminum FP accelerometer.

$$M\ddot{x_p} + kx_p + c\dot{x_p} = fe^{i\omega t} \tag{3.7}$$

where M is the suspended mass, c the velocity damping term, k the spring stiffness and ω the angular frequency of excitation.

Velocity damping is however not the only mechanism to damp an oscillator. Damping from internal friction, or *structural damping*, in the suspension often becomes significant when the oscillator operates in vacuum. Internal friction causes the material to continue to stretch after its initial response to an external force. From the application of external stress, the material spring regions are not stretched elastically and do not follow Hooke's Law: $F = -k\delta x$. It has become *anelastic*. The departure from elastic stretching in a material causes dissipation of energy. To describe structural damping, an imaginary term is added to the spring constant, resulting in a spring model where:

$$F_{spring} = -k(1+i\phi)\delta x \tag{3.8}$$

Here, ϕ is the structural loss angle, the degree of anelasticity of the spring material. ϕ is a measure of the fraction of energy loss per cycle from internal friction. If the spring constant is now replaced as $k \rightarrow k(1+i\phi)$ in the viscous equation of motion (Equation (3.7)), one finds the general equation of motion of a viscously and structurally damped harmonic oscillator:

$$M\ddot{x_p} + k(1+i\phi)x_p + c\dot{x_p} = fe^{i\omega t} \tag{3.9}$$

Mechanisms that induce viscous and structural damping are described in Section 3.2.1.

3.1.2. Material and design characteristics

The mechanical design of aluminum is comparable with that of the first FP accelerometer invented: the proof mass is suspended from the IP leg, and the IP leg is suspended from the frame, see Figure **??**. The IP flexures are thus under tension, like the regular pendulum ones. However, frequency modes resulting from this design, between $f = 80$ - 100 Hz, were distorting the response of the accelerometer in closed-loop and limiting the achievable gain of the control [2]. For that reason, a new design was conceived that reduced the arms' masses, increasing their natural frequencies, which would result in an extended operable bandwidth for the feedback loop. This was mainly achieved by replacing the IP arm with an arm equal to the regular pendulum arm, but with flexures under compression (see Figure 3.2a).

Besides, the new design was fabricated from titanium. As the resistivity of titanium is about 36 times less than the resistivity of aluminum, it was originally conjectured that using this material would diminish eddy current damping (a damping effect that results from local current rings being generated in a metal due to a moving magnet nearby. This phenomenon is more extensively discussed in Section 3.2.1). However, from Section 3.3.4 it will become clear that a main advantage of the titanium design is that its proof mass is heavier, as the material is denser than aluminum.

Both FP accelerometers are suspended via four pairs of co-axial flex joints. The instruments are carved out of a single block of metal. This is done to avoid shear effects at contact surfaces of separate materials, possibly generating hysteresis and structural energy dissipation [45]. The monolithic

Table 3.1: Material and design parameters

Parameter	Symbol	Titanium *Ti6Al4V*	Aluminum *AW7075-T6*
Naked natural frequency	f_0	0.42 Hz	0.47 Hz
Proof mass	M_{proof}	0.68 kg	0.5 kg
Pendulum leg mass	m_p	0.005 kg	0.004/0.012 kg
Pendulum leg length	l_p	50 mm	60/65 mm
Flexure length	l_f	3.3 mm	4.5 mm
Flexure width	w	6 mm	8.8 mm
Flexure thickness	t	0.08 mm	0.1 mm
Density	ρ	4400 kg m^{-3}	2620 kg m^{-3}
Youngs modulus	E	$113 \cdot 10^9$ kg m^{-1} s^2	$71 \cdot 10^9$ kg m^{-1} s^2
Spec. heat cap. (volumetric)	c_s	$2.5 \cdot 10^6$ J m^{-3} K^{-1}	$2.3 \cdot 10^6$ J m^{-3} K^{-1}
Electrical resistivity	ρ_e	$1.71 \cdot 10^{-6}$ Ω m	$5.22 \cdot 10^{-8}$ Ω m
Thermal conductivity	κ	7.2 W m^{-1} K^{-1}	116 W m^{-1} K^{-1}
Lin. coeff. of thermal expansion	α	$8.9 \cdot 10^{-6}$ K^{-1}	$2.2 \cdot 10^{-5}$ K^{-1}

design and machining also results in lower thermal sensitivity and reduced directional cross-talk due to misalignments between mechanical components typical in composite structures [45].

Mechanical design and material characteristics of the titanium and aluminum accelerometer are listed in Table 3.1. The effective proof mass used for calculations on both accelerometers is approached as $M = M_{\mathrm{proof}} + m_{\mathrm{added}} + m_p/2$, and the effective pendulum leg lenght as $l = l_p + l_f/2$.

3.2. Thermal noise and the quality factor

3.2.1. The quality factor

An important property of a pendulum is its quality factor Q. This property is associated with energy dissipation mechanisms that damp the pendulum. Q is defined as the ratio between the energy stored in the resonator and the energy lost during one full oscillation. This means that a high Q oscillator loses a small amount of energy per cycle, and consequently dies out with a long decay time. The relationship between Q and the decay time τ is given as [18]:

$$Q = \frac{\omega_0}{2}\tau \tag{3.10}$$

The total quality factor is related to viscous and structural Q as:

$$\frac{1}{Q_{tot}} = \frac{1}{Q_{viscous}} + \frac{1}{Q_{structural}} \tag{3.11}$$

where Q is related to the viscous damping coefficient in Equation (3.5) by [18]:

$$Q_{viscous} = \frac{M\omega_0}{c} \tag{3.12}$$

Damping forces that result in the viscous quality factor are drag, squeezed film damping, eddy current damping and electromagnetic induction damping. *Drag* is the resistance from air due to gas molecules colliding with the moving object. *Squeezed film damping* is caused by energy dissipating air flows created when the gap between two parallel plates is reduced, and the gas inside the film is squeezed [51]. *Eddy currents* are local current loops, induced in a conductive material when a magnet is moving nearby. Kinetic energy is used for this and consequently damping occurs. *Electromagnetic induction damping* arises inside a voice coil, where the moving magnet induces currents that acquire energy to push through the resistance of the coil windings, dissipating kinetic energy of the pendulum.

In Section 3.1.1 it is described that there are two restoring forces acting on a swinging pendulum: the gravitational force and the elastic force. Energy dissipation from these forces solely results from the departure of the spring material from elastic stretching: anelasticity. Gravity, on the other hand, is lossless. The ratio between elastic energy, being partially dissipated, and the total energy in the system, is the dilution factor [52]:

$$\gamma = \frac{E_{el}}{E_{el} + E_g} \tag{3.13}$$

which can be equivalently expressed in spring constants k, to which energy relates linearly. The quality factor of a structurally damped pendulum is the inverse of the structural loss angle ϕ times the dilution factor [52]:

$$Q_{structural} = \frac{1}{\phi}\frac{k_{el} + k_{grav}}{k_{el}} \tag{3.14}$$

and the total spring constant is $k_{el} + k_{grav} = M\omega_0^2$, so:

$$Q_{structural} = \frac{1}{\phi}\frac{M\omega_0^2}{k_{el}} \tag{3.15}$$

Straightforwardly, the dilution factor is thus expressed as:

$$\gamma = \frac{k_{el}}{M\omega_0^2} \tag{3.16}$$

The elastic stiffness k_{el} of the FP is the sum of the rotational stiffness of all 8 flexures of length l_f, divided by the squared effective pendulum leg length l:

$$k_{el} = 8\frac{EI}{l_f}\frac{1}{l^2} \tag{3.17}$$

where E is Youngs modulus and I the cross-sectional moment of inertia of the flexure:

$$I = \frac{wt^3}{12} \tag{3.18}$$

with w and t the width and thickness of the flexure. Plugging this into Equation (3.17) provides the total elastic stiffness of the FP:

$$k_{el} = \frac{2Ewt^3}{3l_f}\frac{1}{l^2} \tag{3.19}$$

The elastic spring constant thus scales with flexure thickness to the third power. And the smaller the elastic damping constant becomes, the higher Q will be (see Equation (3.15)), providing the reason to aim for thinnest flexures possible. The thickness t of the flexure is limited by two factors: the machining capabilities and the material strength. The two 'newest' FP accelerometers used in this research are limited by machining capabilities.

Thermo-elastic damping Among the causes of internal friction damping, most of which are connected to the dynamics of the dislocations in the crystalline structure at microscopic level [53], only one is determined by material properties: *thermal-elastic damping*. Thermo-elastic (TE) damping occurs in flexures when they are bend, compressing the side of the flexure to witch the bending is directed, and stretching the other side. A flow of heat is generated as the compressed side heats and the stretched side cools, in order to restore equilibrium in the flexure. This reduces the elastic restoring force as this force relaxes to a smaller equilibrium value [54]. The *Standard anelastic solid* model of Zener describes a relaxation process that predicts a frequency dependent loss angle ϕ as [53]:

$$\phi = \Delta\frac{\omega\tau'}{1 + \omega^2\tau'^2} \tag{3.20}$$

Δ the *relaxation strength* and τ' the *relaxation time* of the flexure. The latter is defined as:

Table 3.2: Modelled dilution factors and thermo-elastic damping parameters for the FP accelerometers.

Parameter	Symbol	Titanium	Aluminum
Dilution factor	γ	1.3	1.7
TE loss angle	ϕ_{TE}	$1.2 \cdot 10^{-6}$	$4.6 \cdot 10^{-7}$
TE quality factor	Q_{TE}	$6.7 \cdot 10^{5}$	$1.3 \cdot 10^{6}$

$$\tau' = \frac{1}{2\pi f_0'} \tag{3.21}$$

where f_0' is the characteristic frequency of a flexure, for a ribbon geometry given by [54]:

$$f_0' = \frac{\pi}{2}\frac{D}{t^2} \tag{3.22}$$

with t flexure thickness and D the diffusion constant, $D = \kappa / c_s$, the ratio between thermal conductivity and specific heat (per unit volume). The relaxation strength of TE damping is given as [53]:

$$\Delta = \frac{E\alpha^2 T}{c_s} \tag{3.23}$$

where α is the linear coefficient of thermal expansion and T the (room) temperature in K. With all parameters as listed in Table 3.1 the loss angle from TE damping is determined for the flexures in the titanium and aluminum FP accelerometers. The Q from TE damping is calculated by plugging Equation (3.23) and Equation (3.21) into Equation (3.20), at $\omega = \omega_0$. The dilution factors are also calculated by inserting Equation (3.19) into Equation (3.16). The results are listed in Table 3.2. Despite having larger proof mass, the titanium dilution factor is smaller because its flexures are both thinner and smaller.

The modelled TE quality factors are part of the total structural damping picture, to which many other factors contribute:

$$\frac{1}{Q_{tot}} = \frac{1}{Q_{TE}} + \frac{1}{Q_{Other}} \tag{3.24}$$

Therefore, having calculated Q_{TE}, only the upper limit of the total quality factor is determined.

3.2.2. Thermal noise

In a viscously damped pendulum system, the random Brownian motion of the thermal bath of molecules around the test mass create a fundamental limit to which the suspended mass can remain at rest. This noise limit is called *thermal noise*. The particles exert a macroscopic force on the test mass given as [54]:

$$F_{th} = \sqrt{4k_B T c} \tag{3.25}$$

with k_B the Boltzmann constant. Adding this force to the viscous equation of motion (Equation (3.7)), and solving in Fourier space, yields a power spectrum of the noise as [2, 54]:

$$x^2_{viscous}(\omega) = \frac{k_B T c}{M^2(\omega_0^2 - \omega^2)^2 + \omega^2 c^2} \tag{3.26}$$

However, according to the fluctutation-dissipation theorem, any dissipation in a system always result to Brownian like fluctuations [54, 55]. Therefore, the structural thermal noise force can be described as:

$$F_{th} = \sqrt{4k_B T \frac{k\phi}{\omega}} \tag{3.27}$$

Adding this force to the structural equation of motion, Equation (3.9) with $c = \frac{k\phi}{\omega}$, the power spectral density of structural thermal noise is obtained, again by solving in Fourier space [54]:

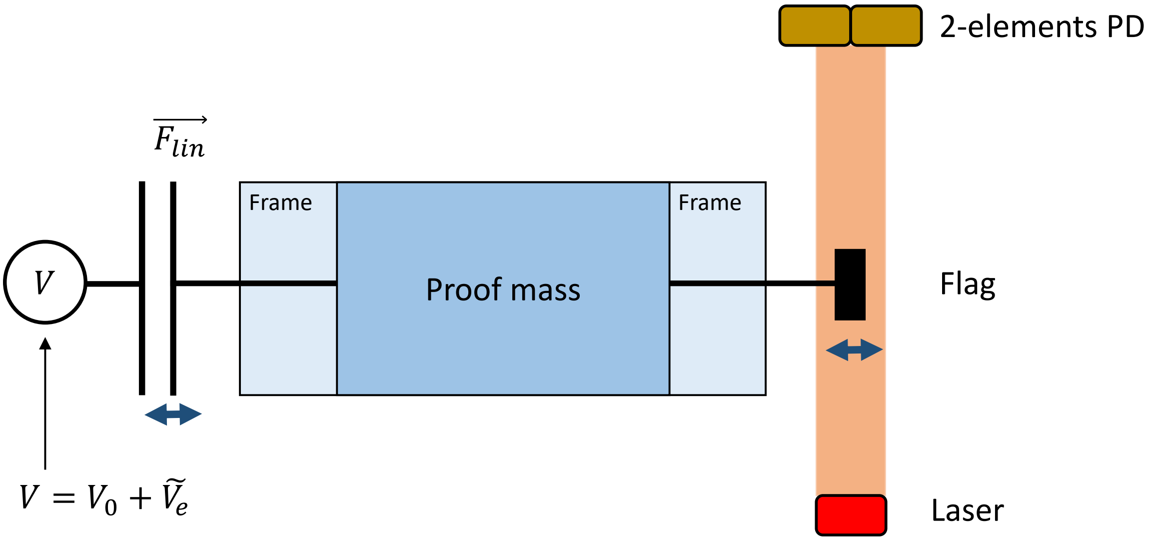

Figure 3.3: Experimental setup to measure decay times of the accelerometer, as viewed from above. On the left side the proof mass is actuated by a parallel plate capacitor, resulting in an oscillating flag on the right side, blocking light to each element of the PD in turns.

$$x^2_{structural}(\omega) = \frac{4k_B T\omega_0^2\phi}{M\omega\left((\omega_0^2-\omega^2)^2+\omega_0^4\phi^2\right)} \tag{3.28}$$

3.2.3. Q of an aluminum and titanium accelerometer at varying pressure

In order to characterize the mechanics of the titanium and aluminum accelerometers, the quality factor of both is measured when in naked configuration. "Naked" means that there is nothing attached to the proof mass that might introduce additional losses. The accelerometers' natural frequencies are tuned upwards in order to move away from the micro-seismic peak at about $f = 0.2$ Hz. The titanium accelerometer's natural frequency is tuned up to $f_0 = 0.86$ Hz, and the aluminum is tuned up to $f_0 = 0.72$ Hz.

Proof mass actuation is depicted schematically on the left hand side of Figure 3.3. The proof mass was actuated by means of a parallel plate capacitor driven by a high voltage amplifier. The HV amplifier output was the sum of a DC bias $V_0 = 200$ V and of a sinewave signal $\tilde{V_e} = V_e\sin(2\pi f_e t)$, with frequency f_e close to the resonance of the accelerometer. In this way the force from the actuator included a term F_{lin} linear with respect to V_e according to:

$$F_{lin} \sim \frac{\epsilon S V_0}{d} V_e \sin(2\pi f_e t) \tag{3.29}$$

where ϵ is the electrical permittivity, S the plates' surface and and d the distance between the plates.

An AC signal from a function generator was delivered to the HV amplifier at frequencies around f_0. It varied in strength, because at around $P = 1$ mbar the circumstances are convenient for electrons to discharge through the air. In this region the breakdown voltage for charge to cross the capacitor becomes lower [56]. Thus to evade breakdown, lower voltages needed to be applied.

A flag was mounted to the proof mass of the accelerometer and its position was read out by means of a shadow sensor consisting of a laser and a two-elements photodiode (PD). Each element was loaded with a 5 kΩ resistor to convert the photocurrent to voltage. In a signal pre-amplifier (SR560), the two signals from the two-elements PD were band-passed at $f = 0.3$ - 3 Hz and subtracted by means of a differential pre-amplifier (SR560), providing the signal used for decay time measurements.

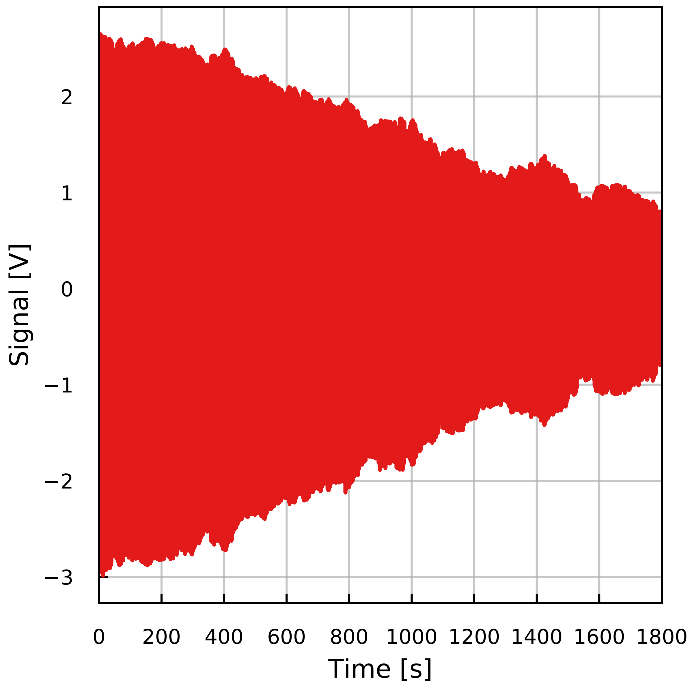

Figure 3.4: A noisy decay time measurement.

The measurements were performed in different pressure regions to verify different damping contributions. The low pressure region ($P < 10^{-3}$ mbar) is most relevant since the accelerometer is meant to be used in high vacuum. To measure Q at different pressures, the accelerometer is placed in a vacuum chamber in which the pressure can be changed from 1 atm to 10^{-5} mbar.

The first decay time measurements in high vacuum were noisy, see Figure 3.4. The accelerometers have high Q, meaning that seismic vibrations are easily transferred to proof mass motion in the vicinity of the natural frequency. The proof mass was thus getting small kicks from the environment, extending the decay time.

To better reject environmental disturbances at the accelerometer resonance, a different readout scheme was used, where a Lock-In Amplifier (SR830) synchronized the function generator signal (driving the actuator) with the output signal, as retrieved from the PDs via the signal amplifier. The amplitude of the output signal at the phase of the function generator (f_e) is tracked, thereby curtailing the effect of seismic noise at frequencies away from f_e. The driving frequency is different from the natural frequency of the signal f_0, and so the Lock-In provides an oscillating signal at a frequency of f_0 minus f_e. The decay of the peaks is the decay of the accelerometer signal amplitude.

Data from the Lock-In Amplifier is taken for up to 1 hour at low pressure regions. In regions above 10^{-1} mbar, the decay time is so small that it is not worthwhile to track amplitudes with the Lock-In. Here, the signal used for the τ-measurement came directly from the signal amplifier. Both approaches display harmonic decaying sine-waves (note, though, that the frequency of the data from the Lock-In is not the natural frequency of the accelerometer), from which the decay time τ is evaluated by fitting both an amplitude envelope and a harmonic sine to the data. The mean of these two fits is taken as the result for τ. The σ's of both fitting methods are typically less than 0.5%. Two examples of such measurements are depicted in figure 3.5.

Having measured τ, Q can be calculated from Equation (3.10). Although the errors of the fits of a measurements might be small, the results of quality factor measurements can vary largely, especially in the low pressure region (up to about 40%). This is because the measurements were performed in a noisy environment, where the oscillating proof mass could still pick up energy from the shaking ground, despite using the Lock-In Amplifier to reject environmental disturbances. A quieter experimental environment would have improved the accuracy of this measurement, but was not at disposal. Therefore, multiple Q measurements were required for one pressure point in order to obtain statistically substantiated data. In the low pressure region of $P < 10^{-3}$ mbar, about 5 measurements per datapoint were

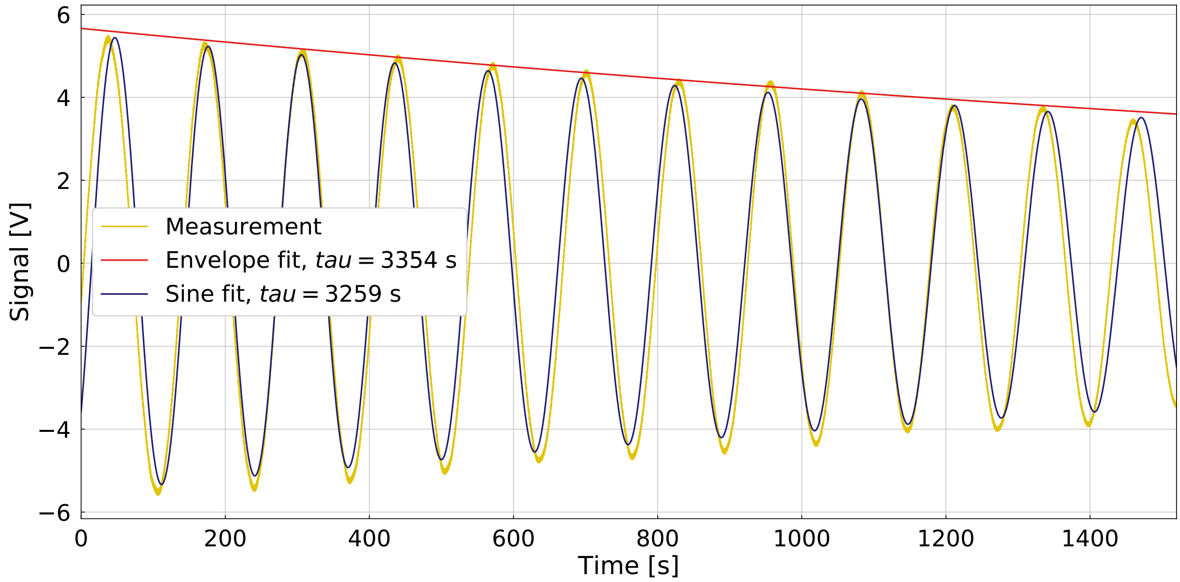

(a) Q measurement at $P = 1.8 \cdot 10^{-5}$ mbar

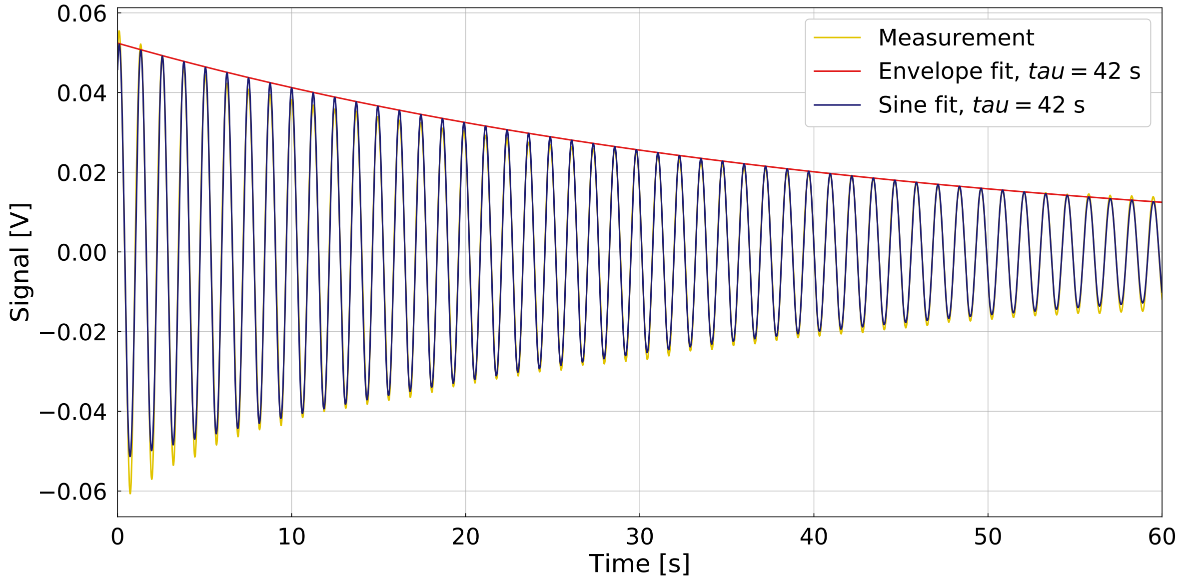

(b) Q measurement at $P = 3.7$ mbar

Figure 3.5: Decay time measurements of titanium. (a) At $P = 1.8 \cdot 10^{-5}$ mbar, where the Lock-In Amplifier was used and (b) at $P = 3.7$ mbar where the signal was read out directly. Errors on both fits are less than 0.5%.

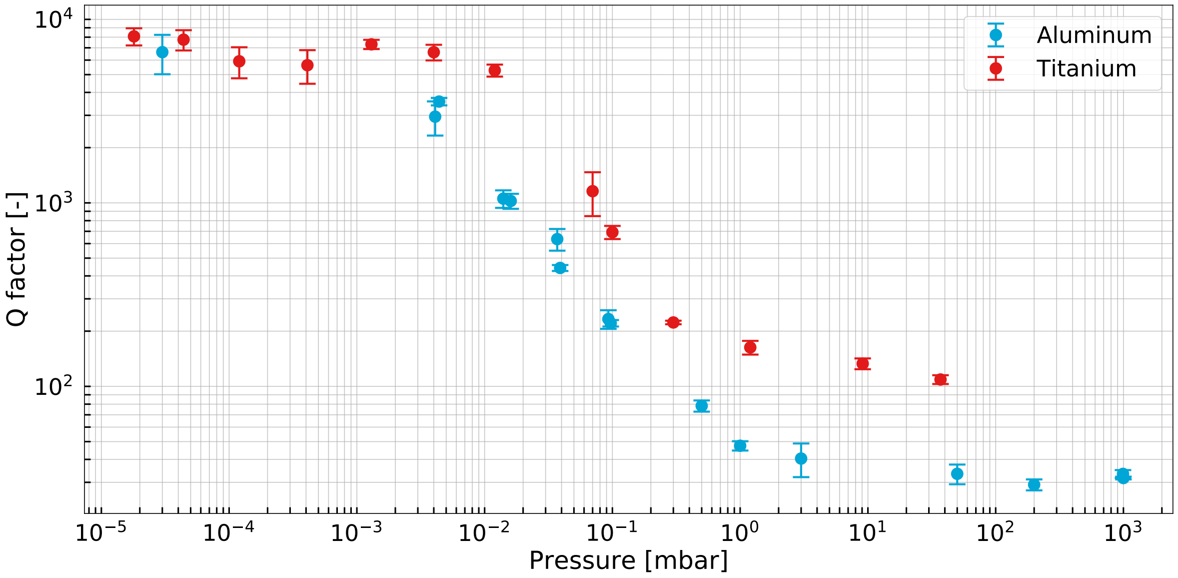

Figure 3.6: The quality factor of both the titanium and aluminum accelerometer in naked configuration. Below $P = 10^{-3}$ mbar Q is determined not to vary significantly, and is solely a result of internal friction mechanisms. In the intermediate area Q is dictated by structural damping and increasingly viscous damping, at increasing P. In the high pressure region the quality factor is a consequence of drag and squeezed film damping.

Table 3.3: Quality factors and loss angles at low pressure (below 10^{-3} mbar).

Parameter	Symbol	Titanium	Aluminum
Quality factor	Q	6900(2200)	6900(1000)
Loss angle	ϕ	$\sim 1.1 \cdot 10^{-4}$	$\sim 8.5 \cdot 10^{-5}$
Measurements	#	19	4

taken. As only acceleration could be injected into the accelerometer by the ground (no deceleration), these Q's are regarded upper limits of the true quality factors. The results of the naked configuration quality factor experiment are displayed in Figure 3.6.

At low pressure, air molecules creating viscous forces are absent, and only structural damping occurs. This reference measurement estimates the ultimate limit that could be reached with the two devices. The averaged quality factors are displayed in Table 3.3, showing large statistical spread: both lie within each others regions of error. The loss angles ϕ differ for both accelerometers, due to different dilution factors γ, see Table 3.2 in Section 3.2.1.

In the intermediate region, at about $10^{-3} < P < 1$ mbar, the mean free paths of the air molecules become increasingly smaller than the gap between the pendulum leg and frame, allowing more air to enter this gap. As the velocity of the molecules (which cause viscous damping) increases quadratically with the pressure, the quality factor falls of with a straight line in the logarithmic scale of Figure 3.6.

From about $P = 10^0$ mbar the quality factor hardly reduces from higher pressures. Besides, in the viscously damped regimes, at intermediate and high pressure, the aluminum accelerometer shows lower Q's than titanium. This is explained by the fact that the IP design of the aluminum accelerometer has more surface that moves to and from the frame and proof mass, resulting in more drag and squeezed film damping. Possibly, also the lower natural frequency of the aluminum accelerometer is partly responsible for this difference.

3.2.4. Tests with the old design feedback actuator

In naked configuration the quality factor of both accelerometers was estimated at $Q \approx 6900$, see Table 3.3. Subsequently, the feedback actuator that actuates the proof mass in closed loop was mounted to the accelerometer, in order to investigate to what extent this would lower the quality factor.

(a) The old feedback actuator design, with the coil mounted to the proof mass. The dark blue shape surrounding the coil displays the ferromagnetic case.

(b) The new feedback actuator design, with the coil mounted to the frame. The magnets lay in a case, inserted from from outside and kept in place with a screw cap.

Figure 3.7: Two designs for the feedback actuator actuator.

The feedback actuator at disposal was the same as the feedback actuator used in previous research [2]. This feedback actuator consisted of a magne, mounted to the frame of the accelerometer, and a coil surrounding the magnet, mounted to the moving proof mass, see Figure 3.7a. Next to that, a ferromagnetic iron yoke surrounded the magnet and coil, guiding the magnetic field flux in such a way that the field was perpendicular to the coil in the gap between the magnet and yoke, making the actuator very linear over a large position range. The yoke had the secondary effect of containing the magnetic flux, reducing the effect of eddy current damping. The coil was made from a 50 μm diameter wire, with the goal of reducing the stiffness of the connection between frame and the proof mass.

Previous research, using this feedback actuator configuration with a similar accelerometer, measured a quality factor as low as $Q = 40$ in high vacuum [2]. Two factors were suspected that could have been responsible for this low Q: eddy current damping and rubbing of coil lead wire against surfaces within the coil case.

For the titanium accelerometer, the extent of eddy current damping is inspected by measuring Q with the feedback actuator mounted, but without the coil attached (and thus no lead wire rubbing). For this measurement the titanium accelerometer was used at low pressure. The quality factor measured was about $Q = 1.09(4) \cdot 10^4$, which is comparable with the naked configuration quality factor measurements. Thus, the titanium accelerometer did not show eddy current damping as expected.

Subsequently, the effect of lead wire rubbing was researched by simply mounting the complete feedback actuator to the titanium accelerometer. The measurement showed that with the full feedback actuator mounted, the quality factor of the titanium accelerometer again was as low as $Q = 58$. That is a reduction of about 115 times compared with average Q values measured in naked configuration. As eddy currents had an insignificant damping effect for the titanium accelerometer, this damping could only arise from lead wire rubbing. To conclude, the lead wires rubbing on the feedback actuator case were responsible for the vastly reduced Q.

3.3. Design of a new voice coil to increase Q

In order to evade lead wire rubbing from the voice coil, a new feedback actuator was designed at Nikhef, which does not have the coil attached to the moving proof mass, but to the frame. This design is pictured in Figure 3.7b. A second permanent magnet with opposite polarity was placed at the opposite coil edge (see Figure 3.8). The advantages of this configuration are twofold:

- Looking at this configuration from a nearby perspective, the second magnet of equal strength approximately doubles the coil's force.
- Moreover, looking from faraway, the two oppositely oriented magnets cancel each other out. They form a magnetic dipole-dipole couple that can be considered analogous to the Helmholtz Anti-Coil, which are two equal rings on a shared axis with current flowing in opposite directions [57]. This moment translates into magnetic field terms that depend on d and r as $\mathbf{B} \propto d^{-4} r^{-3}$, whereas that of a magnetic dipole as $\mathbf{B} \propto r^{-3}$ [58]. Thus, the relatively small distance between the magnets ($d \ll r$) leads to a substantial reduction of the magnetic field as compared with the field coming

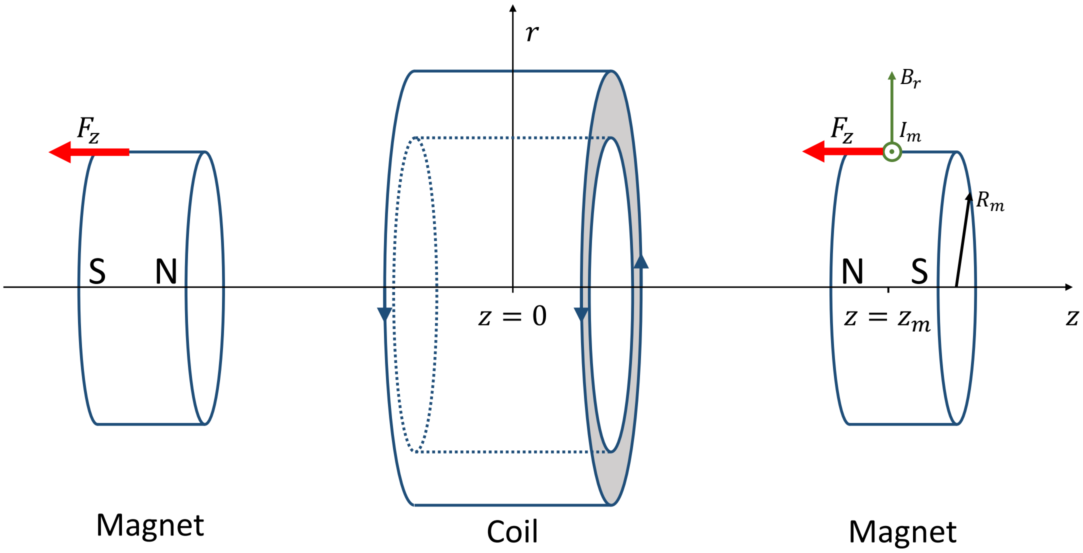

Figure 3.8: Sketch of the coil and two oppositely aligned magnets. The radial magnetic field of the coil B_r couples on the magnet edge (R_m) where hypothetical current I_m flows, to generate a Lorentz force F_z. The distance between magnet and coil is denoted z_m.

from a one-magnet dipole. Nonetheless, the fields do not cancel out each other entirely, so magnetic coupling with environmental stray fields, however small, might still be possible. The extent of this effect is not researched and is recommended to be studied in future experiments.

These advantages led to the effort to model and design a new feedback actuator. In the following section the force of the feedback actuator is calculated and the optimal distance between the coil and the magnets is determined. Subsequently, the physical properties of the new feedback actuator are mapped in Section 3.3.2, and the force requirement of the feedback actuator is described in 3.3.3. A disadvantage of the reversed construction is that the magnets are not surrounded by a ferromagnetic case that absorbs the B field, and diminishes eddy current effects. Therefore, the extent of damping from eddy currents is investigated experimentally, see Section 3.3.4, and it was determined that it does not significantly deteriorate Q for both the titanium and aluminum accelerometer. Finally, in 3.3.5 the mechanical improvement of this design as compared with the old feedback actuator is specified, and the implications of this improvement for the thermal noise of the accelerometer are interpreted.

3.3.1. A model to calculate the force of the feedback actuator

In the situation depicted in Figure 3.8, the two magnets have equal dimensions and are placed at equal distance from the coil center, making the system symmetric around the center of the coil. In this approach, both the coil and magnet are represented as a collection of current loops. This unconventional approach takes advantage of the fact that the magnet can be represented as a collection of magnetic dipole moments, generating a net hypothetical current loop around the magnet. Here, the radial component of the magnetic field from the coil, $B_r(z, r)$, is regarded as the magnetic field generator. In this situation, $B(z_m, R_m)$ is to be calculated because the radial field acts on the edge of the magnet ($r = R_m$), and the magnet is located at $z = z_m$. The current loop of the magnet with current I_m on which $B_r(z_m, R_m)$ acts is considered the field receptor. The Lorentz force from the coil acting on the magnet is:

$$F_z(z_m) = B_r(z_m, R_m) \cdot I_m \cdot (2\pi R_m) \tag{3.30}$$

This equation denotes an axial force that is variable with the distance between the coil and the magnet (and, of course, the physical parameters of the coil and magnets). In order to calculate $F_z(z_m)$, first, the radial magnetic field of the coil $B_r(z,r)$ is resolved, and secondly, the current I_m around a magnet is calculated.

To calculate $B_r(z,r)$, the off-axis radial field of a single loop is first defined. Then, this field is integrated over the length L_c and thickness ΔR_c of the coil, resulting in the total field from a solenoid.

The radial magnetic field in any point P generated by a loop of radius R is calculated by the use of the Biot-Savart law:

$$\mathbf{B}(\mathbf{r}) = \oint_l \frac{\mu_0 I}{4\pi|\mathbf{r}-\mathbf{R}|^3}\, dl \times (\mathbf{r}-\mathbf{R}) \tag{3.31}$$

Here, the loop is centered at the z_0 plane, and a line element dl on the ring is connected to P by the vector **r** – **R**. The magnetic field on the z axis is straightforward to derive due to symmetry concerns, but also the fields in off-axis points P are determinable, and these are desired for this problem. To determine off-axis values of **B**(**r**), first note that the radial component of the vector $dl \times (\mathbf{r}-\mathbf{R})$ is given by:

$$dl \times (\mathbf{r}-\mathbf{R})\big|_r = (z-z_0)R\cos\varphi d\varphi \tag{3.32}$$

where φ is the azimuthal difference between **R** and **r**. Moreover, R is the radial component of **R** - the radius of the coil - and $Rd\varphi = dl$. Furthermore, the norm of the vector **r** – **R** is given by:

$$|\mathbf{r}-\mathbf{R}|^2 = R^2 + r^2 + (z-z_0)^2 - 2rR\cos\varphi \tag{3.33}$$

And like R, r is the radial component of **r**. Filling Equations (3.32) and (3.33) in the Biot-Savart integral (Equation (3.31)), the following is obtained:

$$B_r(z,r) = \frac{\mu_0 I(z-z_0)R}{4\pi}\int_0^{2\pi} \frac{\cos\varphi}{[R^2+r^2+(z-z_0)^2-2rR\cos\varphi]^{\frac{3}{2}}}d\varphi \tag{3.34}$$

This integral can be expressed as a combination of complete elliptic integrals of the first and second kind, $K(x)$ and $E(x)$ respectively.[1] This provides the final expression for the off-axis radial magnetic field from a current loop:

$$B_r(z,r) = \frac{-\mu_0 I(z-z_0)}{2\pi\sqrt{C}}\left[K\Big(\frac{\pi rR}{C}\Big) - \frac{B}{A}E\Big(\frac{\pi rR}{C}\Big)\right] \tag{3.35}$$

Where

- $A = (R-r)^2 + (z-z_0)^2$
- $B = R^2 + r^2 + (z-z_0)^2$
- $C = (R+r)^2 + (z-z_0)^2$

The derivation of Equation (3.35) from (3.34) is portrayed by Babic and Akyel [59]. Equation (3.35) describes the off-axis radial B field generated by a single current ring. To find the total field from a complete coil with N windings, length L_c and thickness $\Delta R_c = R_{out} - R_{in}$, consider an infinitesimal current element dI_c going through a surface element $dz_c dr_c$ in the coil:

$$dI_c = NI_c\frac{dz_c}{L_c}\frac{dr_c}{\Delta R_c} \tag{3.36}$$

Where dz_c and dR_c are integration variables corresponding respectively to variables z_0 and R from Equation (3.35). The current element generates an infinitesimal radial field $dB_r(z,r)$. Integrating this over the coil dimensions gives:

$$B_r(z,r) = \frac{NI_c}{L_c\Delta R_c}\int_{L_c}\int_{\Delta R_c} B_r(z,r)dR_c dz_c \tag{3.37}$$

---

[1] $K(x) = \int_0^{\frac{\pi}{2}} \frac{1}{\sqrt{1-x^2\sin^2\varphi}}d\varphi$ and $E(x) = \int_0^{\frac{\pi}{2}} \sqrt{1-x^2\sin^2\varphi d\varphi}$

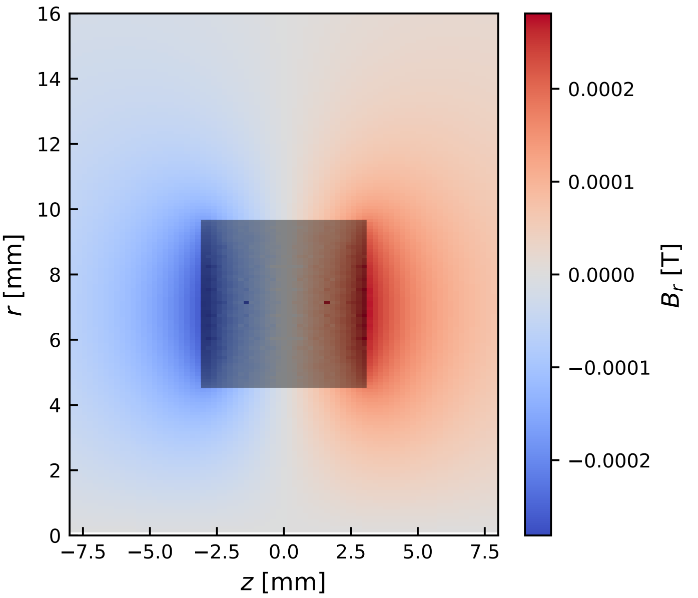

Figure 3.9: Radial B field from the coil as a function of axial distance z and radial distance r. The black rectangle represents the coil (intersected).

After substituting all parameters and variables and setting correct boundaries, the final expression becomes rather large and complex:

$$B_r(z,r) = \frac{\mu_0 N I_c}{2\pi r L_c \Delta R_c} \int_{\frac{-L_c}{2}}^{\frac{L_c}{2}} \int_{R_{in}}^{R_{out}} \frac{(z - z_c)}{\sqrt{C}} \left[K\left(\frac{\pi r R_c}{C}\right) - \frac{B}{A} E\left(\frac{\pi r R_c}{C}\right) \right] dR_c dz_c \tag{3.38}$$

which is best solved using numerical methods. This is done in Python by the use of the *ellipE* and *ellipK* packages from scipy.special, and the multiple *quad* packages from scipy.integrate. The dimensions of the new feedback actuator are displayed in table 3.4a. The result of the modelled radial magnetic field is displayed in a colour scale plot of $B_r(z,r)$ in Figure 3.9. $B_r(z,r)$ can now be substituted into Equation (3.30), with $r = R_m$ and $z = z_m$.

Finally, I_m - representing the theoretical current of the magnet - needs to be determined for solving Equation (3.30). This is done by acknowledging the equivalence of a permanent magnet with magnetic dipole moment $\mathbf{m} = \frac{1}{\mu_0}\mathbf{B}_{rem}\mathbf{V}$ and a current loop with dipole moment $\mathbf{m} = I\mathbf{A}$ [57]. Equating the two and solving for I yields a hypothetical magnetic current of:

$$I_m = \frac{B_{rem} L_m}{\mu_0} \tag{3.39}$$

With B_{rem} the magnetic remanence of the magnet, μ_0 the magnetic permeability in vacuum and L_m the magnet length. This, however, only represents a current around a magnet at one location z. To find the total force acting on the magnet it is necessary to integrate $F_z(z_m)$ along its length L_m. Accordingly, consider an infinitesimal part of the current along the length of a magnet:

$$dI = \frac{B_{rem}}{\mu_0} dl \tag{3.40}$$

If the magnet is centered at $z = z_m$, Equation (3.40) results in an infinitesimal force element $dF_z(z_m)$. Then, plugging this into Equation (3.30) and integrating over the length of the magnet yields the final formula for the force:

$$F_z(z_m) = \frac{B_{rem}}{\mu_0}(2\pi R_m) \int_{z_m - \frac{L_m}{2}}^{z_m - \frac{L_m}{2}} B_r(z_m, R_m) dz_m \tag{3.41}$$

which is actually a triple integral as $B_r(z_m, R_m)$ is a double integral itself (see Equation (3.38)). From Equations (3.38) and (3.41) it is seen that F_z changes linearly with varying I_c. For a coil and magnet with

Table 3.4: Parameters used for modelling the axial force from a coil on a magnet.

(a) Coil parameters

Parameter	Symbol	Value
Length	L_c	6 mm
Inner radius	R_{in}	4.6 mm
Outer radius	R_{out}	9.6 mm
Windings	N	506
Current	I_c	1 mA

(b) Magnet parameters

Parameter	Symbol	Value
Length	L_m	5 mm
Radius	R_m	2.5 mm
Inter-magnet distance	$2z_m$	8 mm
Magnetic remanence	B_{rem}	1.32-1.37 T[a]

---

[a] Magnet made of NdFeB, Article ID: S-05-05-N

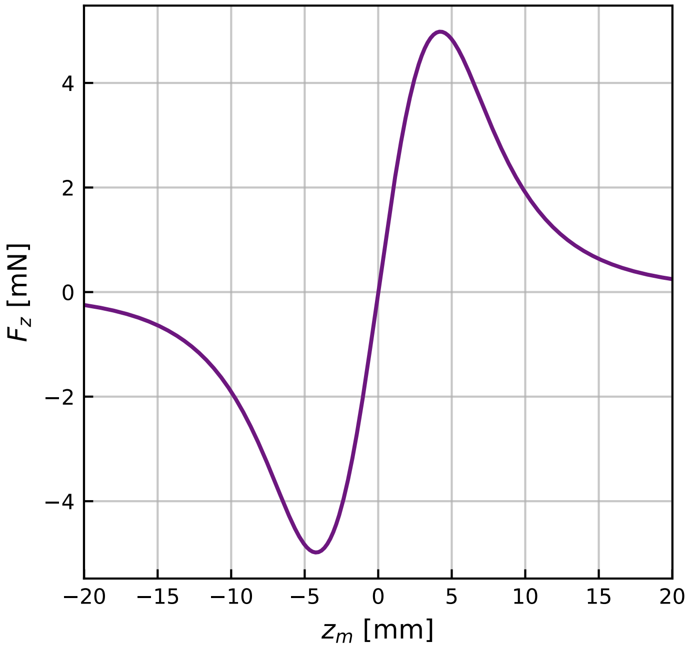

Figure 3.10: Lorentz force from the coil centered at $z = 0$ mm on a single magnet at varying positions z_m.

parameters listed in Table 3.4, this equation gives a concluding value for a Lorentz force at a specified coil-magnet distance z_m.

Now that the force acting on the magnet is modelled, the optimal distance between the coil and one magnet can be specified. This is done by calculating $F_z(z_m)$ for an array of z_m values. The result of this calculation is depicted in Figure 3.10.

Figure 3.10 displays a clear optimum. The maximal force is 4.98 mN at a optimal magnet distance of $z_m = 4.32$ mm. In the maximum region, force scales approximately linear with distance z_m, which is a requirement for a linearly actuating voice coil. Therefore, it is important that the magnet is located near this maximum. In the design of the new feedback actuator magnets are placed in a hollow tube, and they can be separated from each other with cylindrical fillings with the same radius R_m. In this way, by customizing filling sizes, the magnets can be placed at desired locations. In the first such arrangement $z_m = 4$ mm, and the force on one magnet is calculated to be $F_z(z_m = 4) = 4.97$ mN. This is 0.2% away from the maximum. However, the linearity of the total system with two magnets should be regarded. There, magnet 2 displays a similar force profile as magnet 1 (presented in Figure 3.10), but then inverted due to its opposite orientation. The total force is calculated by translating this plot to the location of magnet 1 (thus $2z_m = 8$ mm to the right) and summing it with the force of magnet 1. The total feedback actuator force profile around $z_m = 4$ mm is depicted in Figure 3.11. It has a maximum of $F_z = 9.94$ mN from a current of $I_c = 10$ mA, thus the systems modelled force response is 0.994 N/A.

The accelerometer design allows the magnets to displace maximally with a distance of 0.5 mm in either direction. With such a displacement, the force changes maximally with 1.6%, see Figure 3.11. However, when the feedback actuator is operated in a closed loop, this order of deviation would never

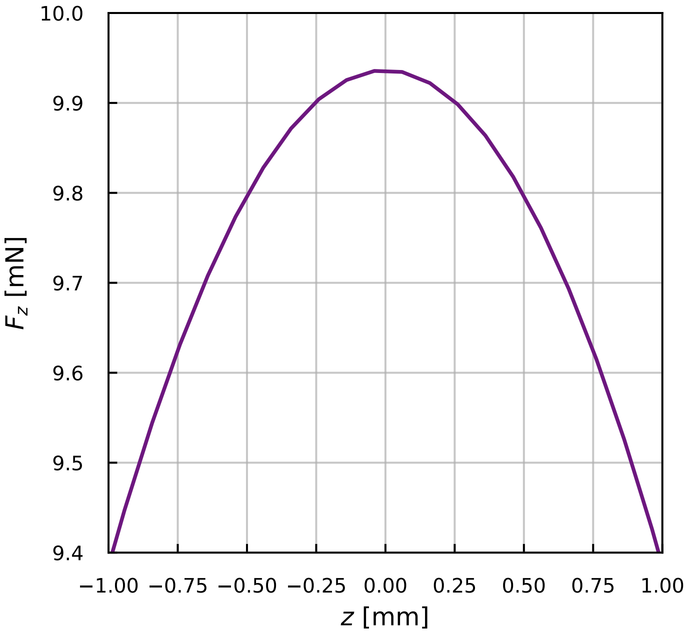

Figure 3.11: Force linearity of the two-magnet feedback actuator when the magnets are 8 mm apart. z is the distance variable along which the center point of the two magnets moves with respect to the coil center. z cannot be more than 0.5 mm away from the calibration point, due to the mechanical design of the accelerometer.

occur - then displacement is in the order nanometers, see Section 3.5.1, resulting in insignificant force deviations. To conclude, the novel feedback actuator is modelled to generate a force of 9.94 mN. And, more importantly, it is modelled to behave as a linear actuator in magnet movement along z.

In this model, the optimal distance between the coil and magnet is calculated. To maximize the new feedback actuator's performance it is recommended that this model is extended with an optimization procedure that incorporates also other physical parameters of the coil and the magnet. A new design of the feedback actuator, based on the calculated optimal parameters can be created. Moreover, it is recommended that the effect of stray magnetic fields on the new feedback actuator are investigated. As the magnets are oppositely aligned this effect is expected to be insignificant, but the extent to which the accelerometer couples with stray magnetic fields should nonetheless be mapped in order to prove the effect indeed is negligible.

3.3.2. Physical properties of the feedback actuator

Pictures of the novel feedback actuator are displayed in Figure 3.12. The feedback actuator is modelled to generate a force of $F/I = 0.994$ N/A. In order to verify this model with experiment, the force output of the feedback actuator was mounted to a scale with double sided scotch and the tube with magnets was placed inside it, being kept in place with a tripod. The tube was placed at such a height that the magnets were at same distance from the coil center as when the feedback actuator is mounted horizontally to an accelerometer, namely 4 mm. Then, the coil was driven at increasing current, ranging from 0 to 10 mA, pushing the coil downwards, away from the immovable tube with magnets. The scale depicted increasing weights as output, which were multiplied with g to find the force. Then, at $I = 10$ mA the scale was gauged at 0. Now current input was decreased from $I = 10$ to 0 mA, and the scale displayed increasingly negative weights. The results of this measurement are shown in Figure 3.3.2. Looking at Figure 3.3.2 it is immediately seen that the F/I slope modelled in Section 3.3.1 intersects the errorbars of the measurements, proving the correctness of the model.

What is more, other physical parameters of the feedback actuator can be measured and calculated. Start with the feedback actuator's resistance. The wire of the coil is made from copper, with $\rho_{copper} = 1.7 \cdot 10^{-8}$ Ωm. Its radius is $r_{wire} = 0.1$ mm and its length is approximately $2\pi N$ times the mean radius of the coil $R_{in} + \Delta R_c/2$. Filling in gives $l_{wire} = 22.6$ m. Now the total resistance can be calculated:

$$R = \frac{\rho_{copper} l_{wire}}{\pi R_{wire}^2} \tag{3.42}$$

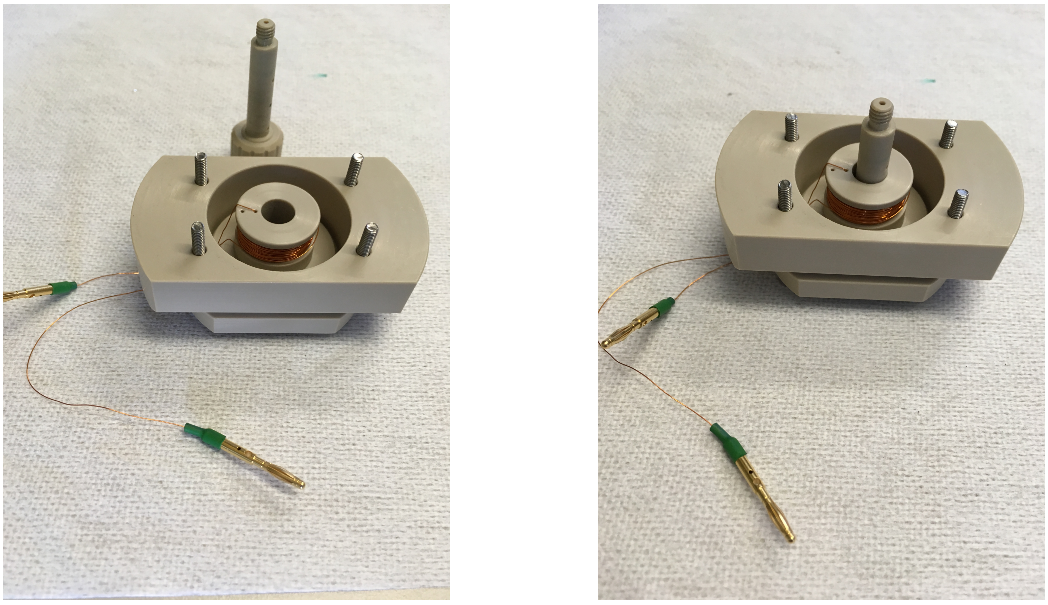

(a) The magnet holder is outside the coil

(b) The magnet holder is inside the coil

Figure 3.12: Pictures of the new feedback actuator. Here, the feedback actuator is displayed laying horizontally, but it is mounted to the accelerometer vertically.

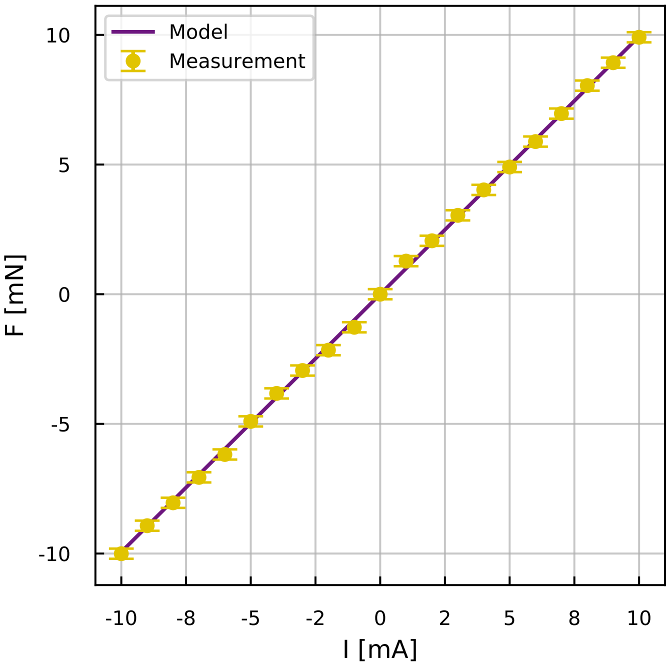

Figure 3.13: Measured force generated by the feedback actuator driven at varying current I_c. The measurements' error bars fall within the modelled F/I slope, calculated in Section 3.3.1.

Table 3.5: Measured and calculated properties of the coil in the feedback actuator

Parameter	Symbol	Measured	Calculated
Resistance	R_{coil}	11.7 Ω	12.2 Ω
Inductance	L	2.8 mH	3.6 mH
Impedance	$\lvert Z(\omega = 628)\rvert$	11.9 Ω	12.4 Ω

which yields a resistance of $R = 12.2\ \Omega$. Next, the inductance of the coil is of importance. This can be calculated by using

$$L = \frac{N\Phi}{I} \tag{3.43}$$

and plugging in

$$\Phi = BA \qquad\qquad B = (\mu_0 \frac{NI}{L}) \tag{3.44}$$

where $A = \pi R_{in}^2$ is the surface of a slice inside the coil. The B field is calculated from Ampere's Law. Plugging Equation (3.44) in (3.43) results finally in:

$$L = \mu_0 \frac{N^2}{l} (\pi R_{in}^2) \tag{3.45}$$

Inserting all values yields an inductance of $L = 3.6$ mH. Now, with the resistance and inductance calculated, the impedance of the system is also known through:

$$Z(\omega) = R + i\omega L \tag{3.46}$$

being a complex function of ω, the angular AC frequency through the coil. The real part of $Z(\omega)$ is the resistance R and the imaginary part, ωL, is called the reactance. The absolute value of $Z(\omega)$ at for instance $\omega = 628$ Hz ($f = 100$ Hz) is $|Z(628)| = 12.4\ \Omega$. Measured and calculated values of R, L and Z are displayed in Table 3.4b.

The magnitude of the impedance, $|Z(\omega)|$, is the ratio of the voltage amplitude to the current amplitude. Therefore, a requirement for a feedback actuator to actuate equally at varying frequency is that this value should remain constant. From Equation (3.46) it can be seen that for small ω this is indeed the case, here $|Z(\omega)| \simeq R$. However, for larger ω's, $|Z(\omega)|$ becomes increasingly large, meaning that the current through the coil is in effect decreasing, resulting in a less forceful actuator than at low frequencies. To only consider a region where the actuator is somewhat independent of ω, a threshold frequency is chosen above which the generated force is not more than 10% less than at $\omega = 0$. This condition is expressed as or $R > 0.9|Z(\omega)|$ and the threshold frequency is calculated to be $\omega = 2044$ rad/s, or $f = 325$ Hz. Values above a few hundred Hz are not of interest anyway, as the accelerometer will be used for LF measurements.

3.3.3. Force requirement of the feedback actuator

The new feedback actuator is required to be capable of providing a certain amount of force: it needs to balance the accelerometer as well as provide feedback signals in the order of magnitude of environmental rms vibrations.

Manual centering of the proof mass has a (pessimistically estimated) tilt error of about $\pm 150\ \mu$rad, resulting in a total possible angle error of $\boldsymbol{\theta} \approx 300\ \mu$rad. To counteract this manual balancing error, a DC force is required to keep the mass centered. This force is proportional to the error angle as:

$$F_{DC} = mg\boldsymbol{\theta} \tag{3.47}$$

which yields about 2 mN for the titanium accelerometer. Then, on top of this DC force, another force is needed that can account for seismic rms accelerations that the device is subject to. The environmental rms acceleration is given by:

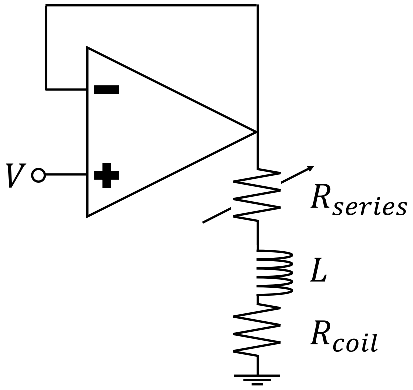

Figure 3.14: Circuit driving the coil with varying series resistance R_{series}. The measured value of R_{coil} is displayed in Table 3.5

$$a_{rms} = \tilde{\sigma}\sqrt{\Delta f} \tag{3.48}$$

$\tilde{\sigma}$ maximally has a value in the order of magnitude 10^{-4} ms^{-2}/√Hz. Δf is the bandwidth of the control loop. This is the frequency range in which the feedback loop operates safely, a property resulting from the design of the PID controller. In Section 3.5.1 the bandwidth was measured to be $\Delta f = 150$ Hz.

These values result in a maximal rms acceleration of $a_{rms} \approx 10^{-3}$ ms^{-2}. From Newton's second law this acceleration demands a maximal force of $F_{rms} \approx 0.7$ mN (for the titanium device). However, this is only the rms force. To cover the full rms noise range, the real force needed is a peak-to-peak force, which is about 3 times the rms value: $F_{pp} \approx 2$ mN.

All in all, the maximal force that the feedback actuator should be capable of delivering is $F_{tot} = F_{DC} + F_{pp} \approx 4$ mN. Especially at low frequencies, where seismic vibrations have the largest amplitude, the required force might approach this upper limit. Comparing the force that the feedback actuator should be capable of delivering, $F \approx 4$ mN, with the measured force presented in Figure 3.3.2, it can be concluded that a current of 5 mA would be enough to drive the accelerometer.

3.3.4. Q and eddy current damping

After the new feedback actuator was modelled and its properties characterized, the quality factor performance of the accelerometer actuated with the new feedback actuator was mapped. The major damping source comes from current induction by the moving magnets in the coil windings. This current dissipates energy through the output resistance of the driving circuit, thereby eating into the kinetic energy of the moving mass. As the dissipation is proportional to the relative velocity between proof mass (with magnets) and frame (with the coil), this is a viscous damping process. In Figure 3.14, a schematic of the driving circuit of the coil is drawn. For such a circuit, the relation between the quality factor and the resistance is approached by Boulaenko [60] as:

$$Q_{coil} = M\omega_0 \frac{R_{coil} + R_{series}}{G^2} \tag{3.49}$$

where G is the response of the voice coil in [N/A] - it is 1 in the case of this feedback actuator (see Figure 3.3.2). From Equation (3.49) it is clear that the larger the series resistance, the higher the quality factor becomes. Infinite resistance in the circuit gives an infinite Q_{coil}, so zero damping - this situation is analogous to the coil being in an open circuit. Otherwise, with no resistance in series, Q_{coil} is smallest and thus damping is largest. The quality factor from induction in the coil adds to the total quality factor likewise as Equation (3.11):

$$\frac{1}{Q_{total}} = \frac{1}{Q_{coil}} + \frac{1}{Q_{viscous}} + \frac{1}{Q_{structural}} \tag{3.50}$$

where it should be noted that Q_{coil} is actually also a viscous term. Besides, the experiment is performed only at very low pressure, so $Q_{viscous}$ comprises virtually no air related damping, but only local eddy current damping, which has been found to be insignificant for titanium (Section 3.2.4). Q_{total} can be expressed as:

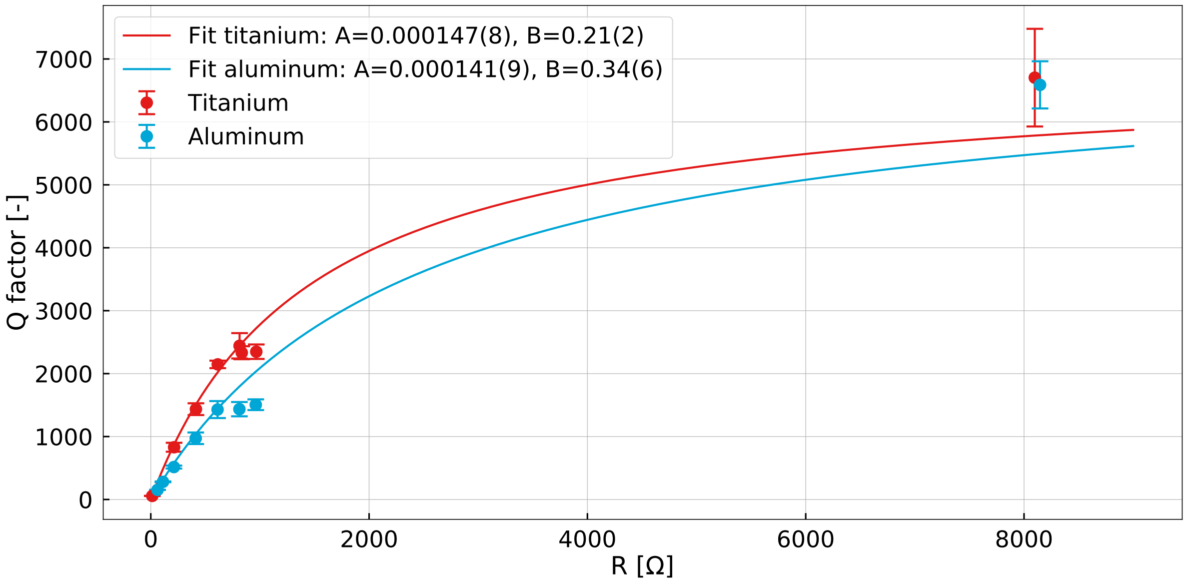

Figure 3.15: The quality factor of both accelerometers with different resistances in series with the coil. The measurements were performed at $P = 2.0(3) \cdot 10^{-5}$ mbar. The two points at the far right were taken with $R = 8150$ kΩ in series. Results of measurements taken at open circuit ($R = \infty$) are not included in the Figure, but listed in Table 3.6.

Table 3.6: Measured quality factors at open coil circuit

Material	Quality factor
Titanium	6300(500)
Aluminum	6300(600)

$$\frac{1}{Q_{total}} = A + \frac{B}{R} \tag{3.51}$$

Or,

$$Q_{total} = \frac{R}{AR + B} \tag{3.52}$$

where A and B are constants, and R is the total resistance in the circuit: $R_{coil} + R_{series}$.

To investigate the influence of the resistance in series with the coil, the novel feedback actuator was mounted to both accelerometers and quality factors were measured for different series resistances. The setup of this experiment was similar to setup described in Section 3.2.3, but here the feedback actuator was used to swing the proof mass instead of the parallel plate capacitor. Moreover, the measurements were only performed in the low pressure region, at $P = 2.0(3) \cdot 10^{-5}$ mbar. The results are depicted in Figure 3.15. In this figure, Equation (3.52) is fitted through the data points, providing fit parameters A and B. Measurements at open circuit ($R = \infty$) are not displayed in the figure as plotting infinity would not make sense, but they are nonetheless taken into account for calculation of the fit. Their values are depicted in table 3.6.

From Figure 3.15, it can be concluded that at resistances below $R_{tot} \approx 4000\ \Omega$, the titanium accelerometer outperforms the aluminum one in terms of Q. This can be explained by the larger proof mass of the titanium accelerometer ($m_{titanium} = 0.76$ kg and $m_{aluminum} = 0.49$ kg), which results in a higher Q_{coil} through (3.49).

Eddy current damping At high resistance the induction damping from the coil is negligible. The data points in this region (at $R = 8160\ \Omega$ and $R = \infty$ - see Figure 3.15 and Table 3.6) show comparable results as for the naked configuration quality factors (determined in Section 3.2.3), for both the titanium

Table 3.7: Quality factors at low pressure (below 10^{-3}). For the feedback actuator configurations, only datapoints from $R_{series} = 8150$ kΩ and open circuit were considered, as to not include induction damping effects.)

Material	Configuration	Q	# Measurements
Titanium	Naked	6900(2200)	19
	Voice Coil	6500(900)	5
Aluminum	Naked	6900(1000)	4
	Voice Coil	6500(700)	5

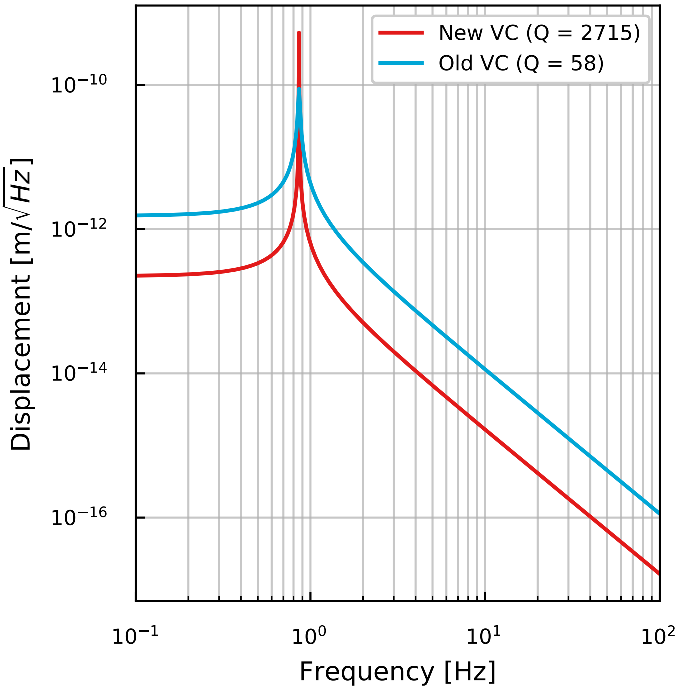

Figure 3.16: Modelled thermal noise of a viscously damped accelerometer, with the old feedback actuator configuration in cyan and the new feedback actuator in red. The natural frequency and the effective proof mass are $f_0 = 0.86$ Hz and $M = 0.76$ kg, for both cases.

and aluminum accelerometer. The measurements from this experiment are within the error bars of the measurements from the naked configurations experiment, see Table 3.7.

It is obvious that eddy currents could only be produced in the new feedback actuator Q-factor experiment, as here there are magnets moving near the conducting frame, whereas in the naked configuration experiments no magnets were present. The fact that these results are comparable for both experiments, means that the precision of the measurements is too low to determine with significance the size of Q from eddy current damping. Quality factor measurements at low pressure are a delicate and challenging task, as is described in Section 3.2.3. Therefore, to find a more precise experimental value of Q_{eddy} and Q_{naked} it is desired to redo the quality factor measurements in a far quieter area.

3.3.5. Thermal noise reduction from a higher Q

When the accelerometer is used for displacement sensing, the feedback actuator will be operated as actuator in closed loop. The coil is connected to the PID via a resistance of $R = 950\Omega$ is series, see Section 3.5.1. The quality factor at this resistance will be around 2715 for the titanium accelerometer.

To conclude, using a titanium accelerometer driven with the novel feedback actuator, the quality factor improved from $Q = 58$ to $Q \simeq 2715$, a factor ~ 47. In terms of suspension thermal noise this means a factor of $\sqrt{47} \sim 6.8$ reduction, see Figure 3.16. As suspension thermal noise is limiting the overall sensitivity of the sensor at low frequency (See Figure 3.20 in Section 3.4.2), actuating the accelerometer with the new feedback actuator would translate into a direct sensitivity improvement of more than a factor 7 in that region.

3.4. The double interferometer readout sensor

The movement of the accelerometer's proof mass must be read out with an extremely sensitive sensor in order to sense movement in the femtometer region. Therefore, Heijningen [2] designed an optical readout scheme based on the double arm interferometer proposed by Gray et al. [61]. The main improvement of this design is the possibility to cancel out intensity fluctuations in the laser power, called *relative intensity noise* (RIN). The signals from both photodiodes (PDs) are matched in size and subtracted to diminish this noise. In this way, the readout board should be able to sense at its shot noise limit.

3.4.1. The interferometer and its readout electronics

The double PD setup, designed by Heijningen [2] and based on Gray's principle, is displayed in Figure 3.17. Before entering the interferometer, the $\lambda = 1550$ nm laser source, The Rock$^{\text{TM}}$ from NP Photonics, is aligned in polarization orientation by beam rotators, and subsequently attenuated. Entering the interferometer, the laser is focused by a collimator lens and inside the interferometer it is split twice by beamsplitters (Thorlabs BS004), see Figure 3.17. One corner reflector mirror is attached to the frame, and for calibration efforts it is mounted on a piezo actuator (HPCh 150/12-6/2 by Piezomechanik). The other corner reflector mirror is attached to the moving proof mass. If this mirror moves, the outgoing light will show interference fringes. These fringes are measured by photodiodes (Thorlabs FGA21). In this configuration $\frac{1}{8}^{th}$ of the light falls on PD1 and $\frac{1}{4}^{th}$ of the light falls on PD2 (the rest is reflected to a non reflective spot or back to the laser). Signals of both photodiodes are equalized in magnitude and subtracted in order to cancel out the common mode RIN of the laser.

In order to characterize the PDs, DC signals and noise levels, one of the two mirrors was darkened to remove interference. For a given laser input power P_{in}, the expected DC voltages are:

$$V_1 = R_{\text{A}}\eta\frac{P_{\text{in}}}{16} \qquad\qquad V_2 = R_{\text{A}}\eta\frac{P_{\text{in}}}{8} \tag{3.53}$$

Where $R_{\text{A}} = (20\ \text{k}\Omega)$ are the transimpedance amplifiers that, in combination with a OPA827 op-amp, convert photocurrent to a voltage for each photodiode. The efficiency of the photodiodes, η, is considered 1. Measuring the PD1 and PD2 output voltages gave $V_1 = 2.1(1)$ V and $V_2 = 4.2(1)$ V. Both yield a similar laser input power of about $P_{\text{in}} = 1.7 \cdot 10^{-3}$ W.

The signals of the photodiodes are lead to a balanced differential amplifier, using a AD8597 op-amp. In 3.18a the electric circuit of this differential amplifier is shown, with a simplified version depicted in 3.18b. As can be seen in 3.18b, the signal V_2 going to the balanced amplifier can be trimmed with a potentiometer resistance. As RIN is common in both PDs, the differential DC output V_{diff} should be trimmed to zero to cancel it. Trimming of V_{diff} is done with one of the interferometer arms darkened. When V_{diff} drifts away from zero, intensity noise will be imparted in the signal. These effects are investigated in Section 3.4.3.

When the board is operating in the regular intereferometer setup, the power levels on both PDs are:

$$P_1 = \frac{P_{\text{in}}}{8}\left(1 + \cos\left(\frac{4\pi\Delta L}{\lambda}\right)\right) \qquad\qquad P_2 = \frac{P_{\text{in}}}{4}\left(1 - \cos\left(\frac{4\pi\Delta L}{\lambda}\right)\right) \tag{3.54}$$

with ΔL the proof mass mirror's positional deviation from a central position corresponding to mid-fringe. From this it can be inferred that the differential voltage output is:

$$V_{\text{diff}} = R_{\text{A}}\eta\frac{P_{\text{in}}}{4}\cos\left(\frac{4\pi\Delta L}{\lambda}\right) \tag{3.55}$$

With the null condition being $\Delta L_n = (n + \frac{1}{2})\frac{\lambda}{4}$. Around one of these values, thus at the center of a fringe, the system is locked in the feedback loop by the voice coil. This is advantageous for two reasons: the voltage response to a proof mass displacement is both maximal and approximately linear at this spot. At the lock point, the interferometer voltage response to proof mass displacement Γ is (in [V/m]):

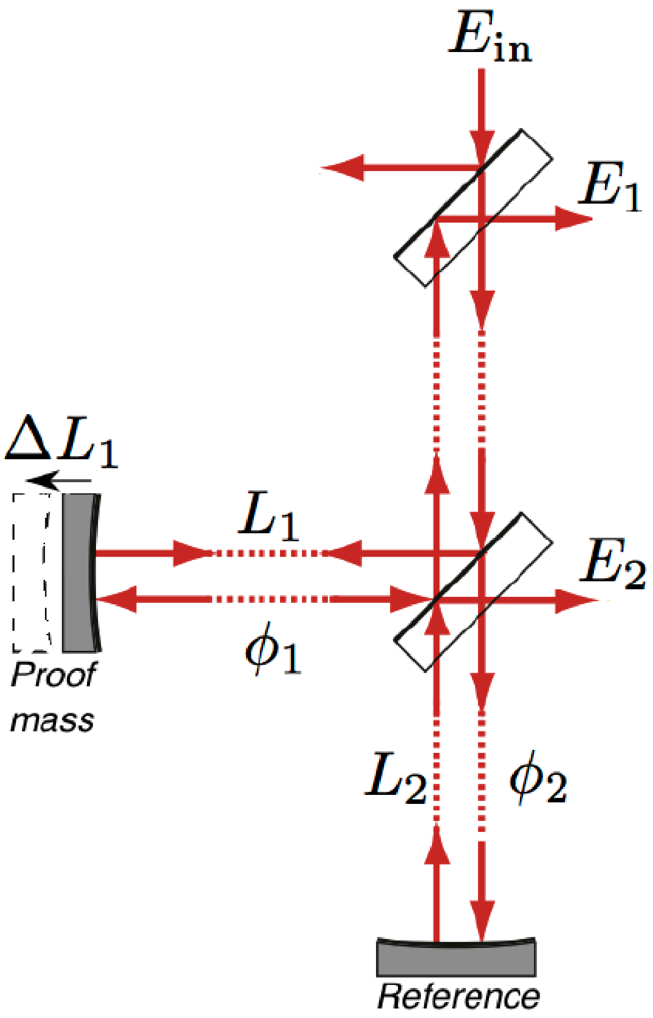

Figure 3.17: The double PD interferometer scheme. With beam splitter (BS) convention where halve the beam is reflected rightward when hitting a BS, this configuration yields, $E_1 = 1/8E_{\text{in}}$ and $E_2 = 1/4E_{\text{in}}$. The remaining light is reflected back to the laser (1/8) or to a dark surface (1/2). From: [2].

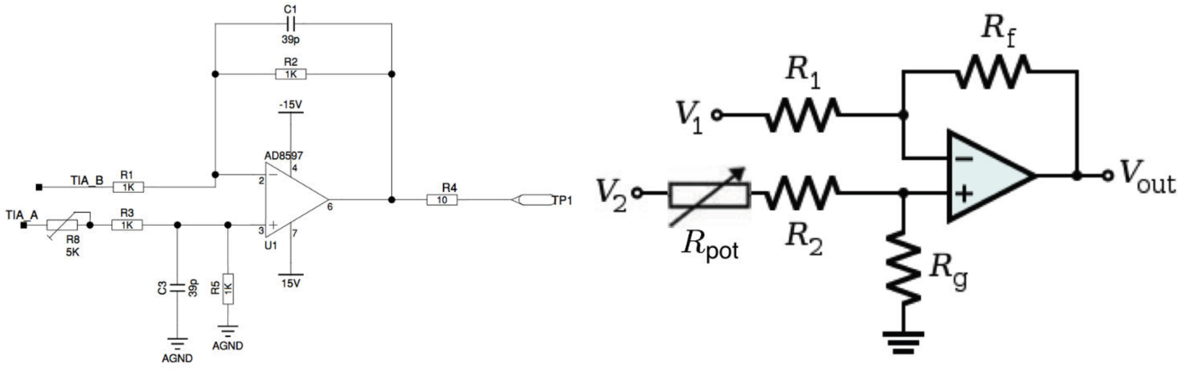

(a) Electric circuit

(b) Schematic

Figure 3.18: Electric circuit (a) and its schematic (b) of the photodiode board. The PDs are loaded with TIA resistors. V_2 is attenuated with the potentiometer resistance to match the signal amplitude of V_1, as only then full suppression of laser power fluctuations is enabled.

$$\frac{\Delta V_{\mathrm{diff}}}{\Delta x} = \Gamma = R_{\mathrm{A}} \eta \pi \frac{P_{\mathrm{in}}}{\lambda} \tag{3.56}$$

In this setup, the interferometer response is modelled to be: $\Gamma = 69$ V/μm.

3.4.2. Noise contributions

Ideally, the accelerometer self noise is governed by thermal noise from viscous damping in the coil until $\sim$ 10 Hz, above which the photon shot noise on the photodiodes becomes the limiting factor. However, the shot noise displacement sensitivities are extremely low and other sources could easily prevent the accelerometer from reaching this fundamental noise limit. Two such sources are non perfect RIN cancellation and frequency noise.

Thermal noise For frequencies below 10 Hz, thermal noise from a viscously damped resonator is the most relevant noise source. The power spectrum of this noise on the proof mass is given by Equation (3.26) in Section 3.2.2. In Section 3.3.5 the thermal noise spectrum of the accelerometer using the new voice coil is calculated for $Q = 2715$. To obtain the sensor's thermal noise displacement sensitivity, the frame acceleration is simply equated to the thermal force, and integrated twice (i.e. multiplied with ω^{-2} in Fourier space):

$$\tilde{x}_{\mathrm{TN}} = \omega^{-2} \sqrt{\frac{4 k_B T \omega_0}{M Q}} = 1.6 \cdot 10^{-13} f^{-2} \tag{3.57}$$

Thermal noise of the accelerometer is typically not visible when it is operated at the seismically isolated bench at Nikhef, as it is lower than the noise of the test-bench at LF.

Photon shot noise on the photodiodes is determined from P_{in}. The current shot noises from the PDs are given by:

$$i_1 = \sqrt{2 e \eta P_1} \qquad\qquad i_2 = \sqrt{2 e \eta P_2} \tag{3.58}$$

where $P_1 = \frac{P_{\mathrm{in}}}{8}$ and $P_2 = \frac{P_{\mathrm{in}}}{4}$ at the working point of the interferometer. Then, to obtain voltage noises, the currents are multiplied with the transimpedance amplifiers R_{A}. As the power is not evenly distributed among and incoherent between the two diodes, the voltage noises are summed in quadrature, with the signal of PD2 halved:

$$\tilde{V}_{\mathrm{sn}} = R_{\mathrm{A}} \sqrt{\frac{3 e \eta}{8} P_{\mathrm{in}}} \tag{3.59}$$

This is the total voltage shot noise in [V/√Hz]. To obtain the interferometer displacement noise, this value is multiplied with Γ^{-1} and a mechanical response term:

$$\tilde{x}_{\mathrm{SN}} = \frac{\tilde{V}_{\mathrm{sn}}}{\Gamma} \frac{1}{f^2} \sqrt{(f_0^2 - f^2)^2 + \left(\frac{f_0 f}{Q}\right)^2} \tag{3.60}$$

Non optimal RIN cancellation Fluctuations in the laser output power are called *relative intensity noise* (RIN). This noise source will limit the interferometer noise above a few Hz when it is not completely subtracted in Gray's double arm scheme, i.e. when V_2 is not perfectly attenuated to match V_1. To have a reference signal containing RIN, a fiberoptic splitter was installed that picked off 1% of the laser light before entering the vacuum vessel. This tabbed signal, coined V_{tab}, was measured with the same PD (Thorlabs FGA21) as in the interferometer. From the pick-off, RIN of the laser was quantified by measuring the noise spectrum $\tilde{V}_{\mathrm{n}}$ of V_{tab}, with DC level V_{DC}:

$$\mathrm{RIN} = \frac{\tilde{V}_{\mathrm{n}}}{V_{\mathrm{DC}}} \tag{3.61}$$

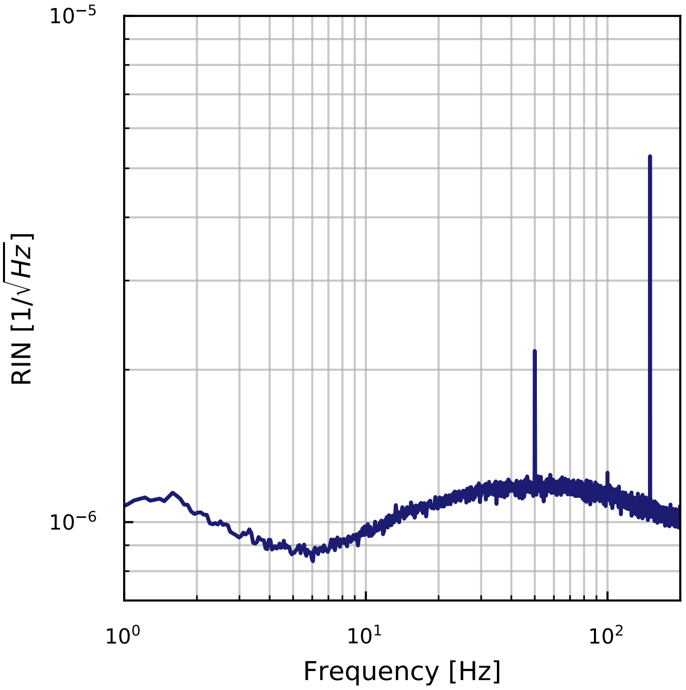

Figure 3.19: RIN measurement. RIN = $\tilde{V}_\mathrm{n}/V_\mathrm{DC}$, with $\tilde{V}_\mathrm{n}$ the measured spectrum.

which is in units of [1/$\sqrt{\mathrm{Hz}}$]. The RIN spectrum is displayed in Figure 3.19. The residual voltage RIN due to a factor α mismatch in the power on the interferometer PDs is:

$$\tilde{V}_\mathrm{RIN} = \frac{\alpha\eta R_\mathrm{A} P_\mathrm{in}}{16}\mathrm{RIN} \tag{3.62}$$

Dividing this voltage spectrum with the interferometer displacement response Γ gives the modelled RIN displacement noise:

$$\tilde{x}_\mathrm{RIN} = \frac{\alpha\lambda}{8\pi}\mathrm{RIN} \tag{3.63}$$

Different values of the subtraction parameter α show what RIN noise levels they correspond to. For instance, with $\alpha = 0.1$, 90% cancellation takes place and with $\alpha = 0.01$, 99% is cancelled. It was calculated that with about 98% cancellation, residual RIN should have about the same noise level as shot noise. RIN is found to be partly limiting the accelerometer to reach its shot noise performance, and this noise source is treated extensively in Section 3.4.3.

Laser frequency noise A third relevant noise source is the frequency noise from the laser, that creates a phase noise on the PDs when the beams in both interferometer arms do not travel exactly the same distance. The arm length mismatch ΔL_0 introduces a frequency dependent noise. For the interferometer used in this research, ΔL_0 was determined to be as large as about 3 mm. This is due to a redesign of the mechanics with respect to the previous experiment of Heijningen [2].

From Bennetts et al. [62], who measured the frequency noise of the PN Photonics The Rock$^\mathrm{TM}$ laser, a power slope of $-2/3$ and a multiplication factor of 5000 was crudely estimated for the frequencies up till $f = 200$ Hz. The frequency noise is then: $5000 f^{-2/3}$ Hz$^{-2/3}$ $\sqrt{\mathrm{Hz}}$. It is converted to displacement through:

$$\tilde{x}_f = \frac{\nu_L}{\nu_0}\Delta L_0 \tag{3.64}$$

which is then multiplied with the same mechanical response term as in Equation (3.60). Here, ν_L is the laser frequency noise and $\nu_0 = \frac{c}{\lambda}$ is the central laser frequency. However, the circumstances in which this laser was operated might be different from the measurement done by Bennetts et al. [62], and therefore this model is a crude estimation reality. From this model it was calculated that $\Delta L_0 = 3$

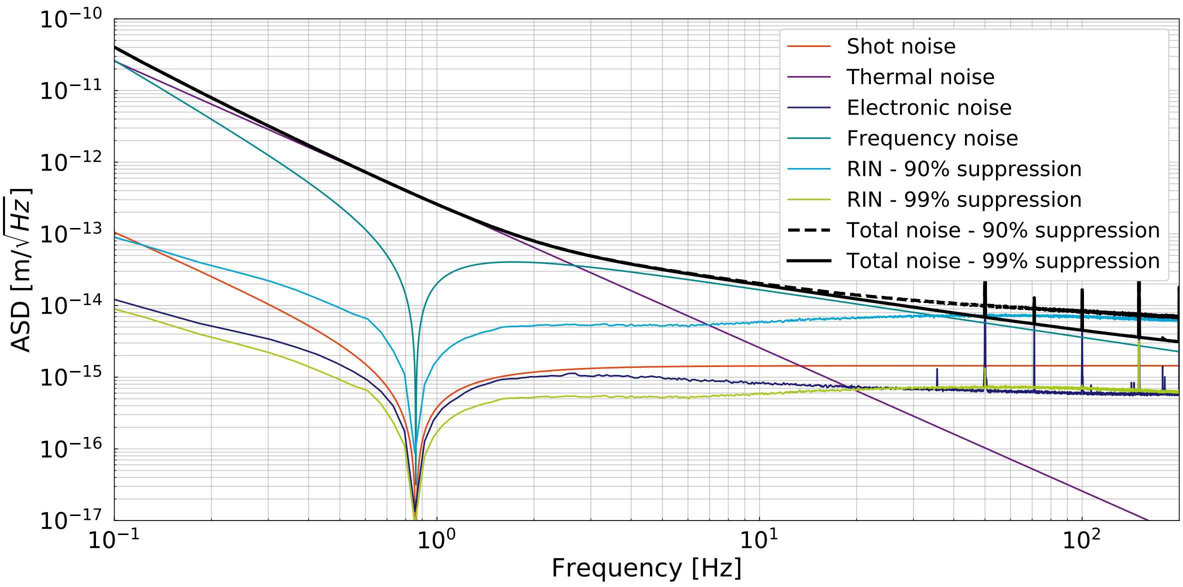

Figure 3.20: Noise budget of the accelerometer. From the measured spectrum of the laser, two cases of RIN suppression are displayed, for 90% and 99% cancellation.

mm results in maximal displacement sensitivities of around 10^{-14} m/$\sqrt{\text{Hz}}$ above 30 Hz, obstructing the acceleromer to reach the shot noise limit. The static arm length difference should be less than 0.5 mm for frequency noise to fall below SN.

The discrepancy of the previous experiment of Heijningen [2], where a noise floor of 8 fm/$\sqrt{\text{Hz}}$ was measured instead of the modelled 3 fm/$\sqrt{\text{Hz}}$, might be explained by a too optimistic model for the laser frequency noise ($500f^{-2}$ Hz^{-2} $\sqrt{\text{Hz}}$).

Electronic noise The total electronic noise, both from the electric circuits of the accelerometer and from the readout, was measured by taking a spectrum of V_{diff} while the setup was placed in a dark environment and the laser light switched off. What is more, the combined noise from the ADC and preamplifier was measured by terminating the input with a 50Ω resistor. The readout noise was determined to be insignificant with respect to the electronic noise from the PID and PD boards.

Signal contrast Contrast of the signal is the ratio of a measured amplitude of the PD fringes, and their maximum possible amplitudes: $(V_{\text{max}} - V_{\text{min}})/(V_{\text{max}})$ - meaning there is maximal contrast when $V_{\text{min}} = 0$. Contrast should be maximal because low contrast implies low SNR, which results in a lower sensitivity curve of the accelerometer. Typically, contrasts of 70% - 90% were measured for both PDs.

From the noise contributions discussed in this Section, a noise budget is modelled for the accelerometer with a quality factor of $Q = 2715$ and natural frequency $f_0 = 0.86$ Hz, see Figure 3.20. In this Figure, it is seen that laser frequency, as estimated, limits the accelerometer to reach SN. What is more, also RIN is a limiting factor when it is not fully suppressed.

3.4.3. RIN suppression

The splitting ratio of the two beam splitters depends on the polarization of the input light. Only if polarization of the incoming light is perfectly aligned with that of the BS, the 50%-50% reflection-transmission will occur. With non-optimal alignment between the input beam and BS, other non-equal splitting ratios arise. This results in an offset in the balanced signals, and the subtracted DC signal V_{diff} will not yield zero anymore. The larger the misalignment between laser beam and BSs, the farther away V_{diff} DC will be from zero, and the more RIN it will contain (thus the larger α in Equation (3.63)). Misalignment between laser beam and BS is caused by polarization drifts, due to thermal variations in the environment. Thermal variations cause the laser fibers to slightly bend, causing a rotation of the polarization of the input beam. The fiber link from the laser to the sensor was about 10 m long and made from PM-fiber,

Table 3.8: Optomechanical and readout electronics parameters of the non-PM and PM fiber setup.

Parameter	Symbol	non-PM fiber	PM fiber
Proof mass	M	0.76 kg	
Natural frequency	f_0	0.86 Hz	
Quality factor	Q	2715	
Thermal noise	$\tilde{x}_{\mathrm{TN}}$	$1.6 \cdot 10^{-13} f^{-2}$ m Hz^{-2}/$\sqrt{\mathrm{Hz}}$	
Laser wavelength	λ	1550 nm	
Transimpedance amplifier	R_{A}	20 kΩ	2.2 kΩ
Input power	P_{in}	1.7 mW	7 mW
Interferometer response	Γ	$6.9 \cdot 10^7$ V/m	$3.1 \cdot 10^7$ V/m
Shot noise	$\tilde{V}_{\mathrm{SN}}$	202 nV/$\sqrt{\mathrm{Hz}}$	32 nV/$\sqrt{\mathrm{Hz}}$
	$\tilde{x}_{\mathrm{SN}}$	2.9 fm/$\sqrt{\mathrm{Hz}}$	1.4 fm/$\sqrt{\mathrm{Hz}}$

which limits polarization drifts to a certain extent, but is extra exposed to thermal effects due to its long length.

Drifting also affects contrast, as contrast is also dependent on the amount of light transmitted throught the BSs. Contrasts were observed to vary with ~5% for both PDs.

In the first experiment, the final parts of the optical setup - the attenuator, the beam rotator, the collimator and connecting fibers - were made from non-PM material, making this setup is highly susceptible to thermally induced polarization angle drifting. What is more, the laser link to the setup totallled about 10 m. The drifting behaviour of V_{diff} DC was indeed visible, resulting in fruitless calibration efforts; after having trimmed the potentiometer resistance to get V_{diff} to zero, it would rapidly obtain offsets of $> 10\%$, whereas it should remain close to 1% for this source to remain below shot noise.

Therefore, to gain control over the polarization angle drifting, the non-PM parts in the setup were replaced with a PM fiber. As the beam rotators were non-PM, polarization alignment of the laser with the beam splitters was now performed by directly rotating the collimator until optimal alignment is reached. Next to the beam rotators, the attenuator was also bypassed, increasing the incoming laser power significantly. In fact, the P_{in} became so large that the PD signals were clipping (i.e. output signals trespassed maximum output voltages of the PDs). To cope with this effect, the transimpedance amplifiers were changed from $R_{\mathrm{A}} = 20$ kΩ to $R_{\mathrm{A}} = 2.2$ kΩ, changing the output signals V_1 and V_2 due to different input power and R_{A} resistances (see Equation (3.53)). The readout circuit characteristics and optomechanical parameters of both the non-PM and PM fiber setup are listed in Table 3.8. Importantly, the modelled shot noise was lowered by increasing P_{in}.

The PM fiber replacement setup improved the stability of static polarization angle drifting, but the effect was still not fully diminished. This is explained by the fact that the setup was not placed in a temperature controlled laboratory, but in an environment where temperature varies with several degrees during the day. What is more, as the laser fiber was over 10 m long, it was heavily exposed to thermally induced polarization angle drifting. By contrast, the measured 8 fm/$\sqrt{\mathrm{Hz}}$ noise floor from 30 Hz onwards of previous research by Heijningen [2], was obtained in a thermally stable environment and with only a ~ 1.5 m long laser fiber.

To gain the possibility to measure coherence between V_{diff} and the laser beam, 1% of the laser beam signal was tabbed, V_{tab}, before entering the vacuum vessel. When the coherence between V_{diff} and V_{tab} is high, RIN is still present in the system. For a time period of about 5 hours, the DC value of V_{diff} was measured in order to observe its time-varying behaviour. In order to only observe intensity fluctuations, the mechanics were blocked and one mirror was darkened, so there was no interference. The level of RIN suppression is given in dB with $V_{\mathrm{diff}}/(V_1 + \frac{V_2}{2})$ as logarthmic argument. In parallel, the coherence between V_{diff} and V_{tab} was measured each ten seconds in the 5 hours time period. Investigating this data, observing a time period where RIN suppression is high, the coherence should be low. Contrarily, when V_{diff} drifts away, the coherence should increase. The results are displayed in Figure 3.21.

The RIN suppression and time-coherence plots of Figure 3.21 satisfy expectations: low coherence

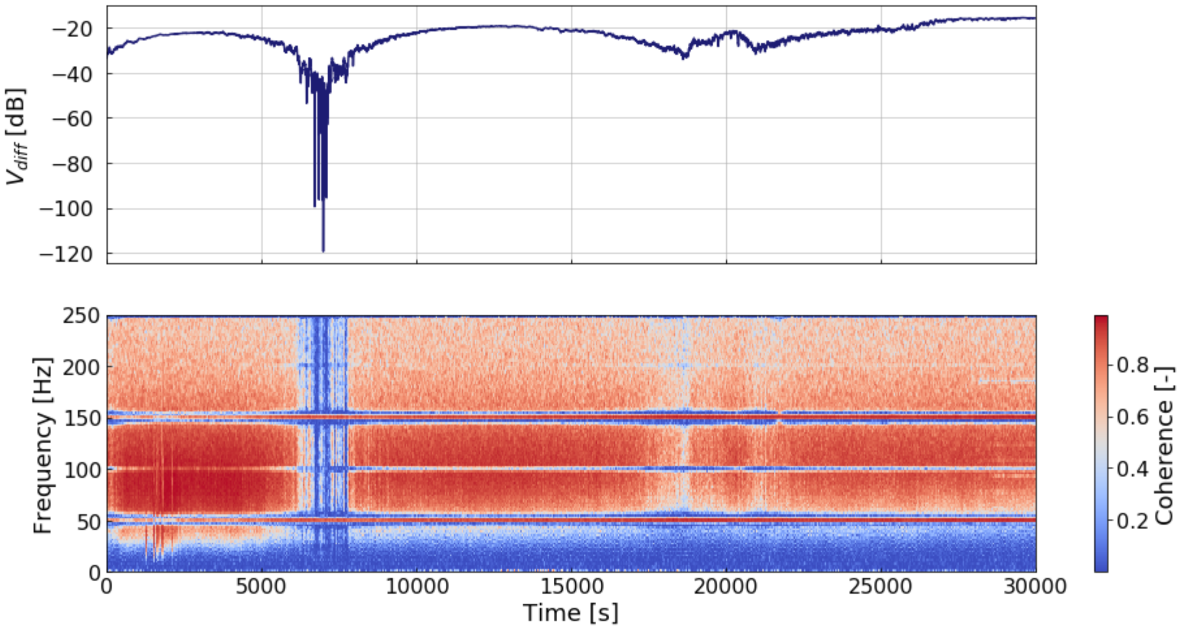

Figure 3.21: RIN suppression of V_{diff} DC and a 2D time-coherence plot. Due to beam polarization angle drifting, V_{diff} drifts away from zero, resulting in non-suppressed RIN and thus high coherence levels with V_{tab}.

is recorded at time ranges when RIN suppression is high (i.e. below -40 dB: within 1% cancellation). However, the DC level of V_{diff} cannot be measured when the accelerometer is in closed loop, and therefore this is an important result. Now, the coherence data can be used as a proxy to see at which time periods high levels of RIN cancellation are achieved. Over that timespan one should expect the accelerometer to reach the best performance.

3.5. Performance measurements

3.5.1. Feedback loop characterization

The accelerometer will eventually operate as vibration sensor. It will operate in closed loop, keeping the proof mass locked at the middle of a fringe, allowing for maximal and linear displacement-to-voltage response. What is more, using this feedback system increases the dynamic range of the accelerometer significantly. In open loop the dynamic range is about $\lambda/4$. Only at the micro-seismic peak, seismic noise is larger than $\lambda/4$; the ground excitation is amplified significantly at the natural frequency of the accelerometer due to the large quality factor. This makes it impossible to stay within a single fringe, resulting in the need for operating the accelerometer in a feedback loop. In this feedback system, the accelerometer's proof mass is the system to be controlled, or the *plant*, the double interferometer readout is the *sensor*, the feedback actuator acts as *actuator* and there is a PID controller, the *servo*, whose filter creates the error signal to the feedback actuator. This signal is used as the accelerometer output.

In Figure 3.22 a scheme of the control loop is displayed, with also the measured reference points V_1 (the error signal) and V_2 (the interferometer signal) and the controllable input noise V_e. The latter is build to introduce noise that is common in V_1 and V_2, allowing the transfer of this noise V_2/V_1 to be determinable. From the block scheme in Figure 3.22 the values of the two reference voltages can be calculated - going anti-clockwise, the block contributions are multiplied. The acceleration of the ground, displayed as $\tilde{a}_f$, introduces extra signal to the circuit and should be added. The same holds for the introduced noise V_e. The force response $\frac{\beta}{M}$ is always negative compared with $\tilde{a}_f$ and should be subtracted. Following these rules V_1, is expressed as:

$$V_1 = V_e + F\alpha H\big(\tilde{a}_p - \frac{\beta}{M}V_1\big) \tag{3.65}$$

Where F and H are frequency dependent responses of the filter and the mechanics respectively. The

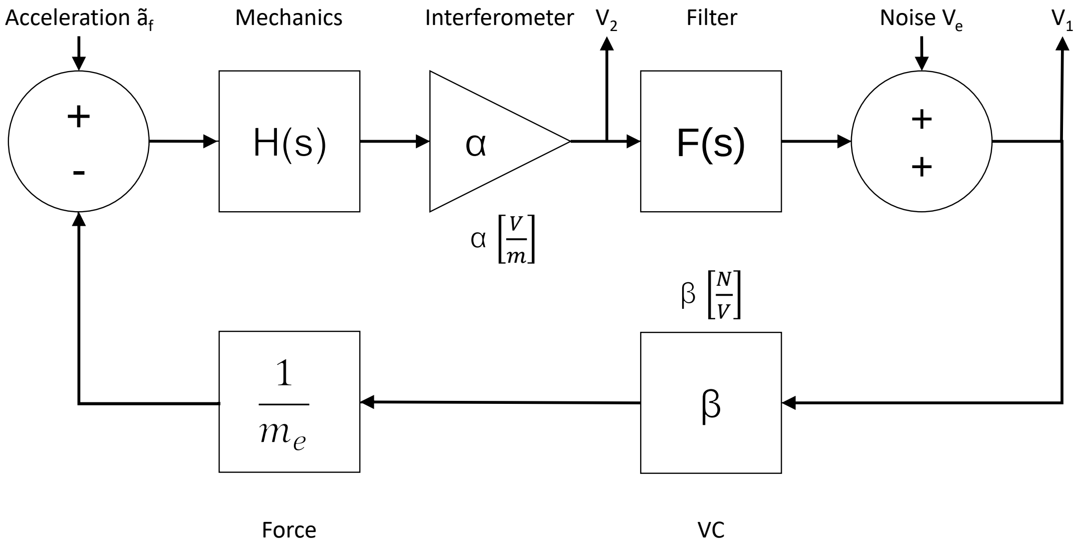

Figure 3.22: Block scheme of the accelerometer feedback loop.

filter response function F is modelled based on the electric circuit design characteristics of each stage in the PID. The mechanical response H of a suspended system to a force, is treated in the Introduction Chapter (see Equation (1.15) in Section 1.3. Recall that H is:

$$H = \frac{1}{M\left((\omega_0^2 - \omega^2) + i\frac{\omega\omega_0}{Q}\right)} \tag{3.66}$$

α in Equation (3.65) is the response from the interferometer readout and $\frac{\beta}{M}$ is the force response from the feedback actuator on the proof mass. They are flat responses (not depending on frequency ω).

As $\tilde{a}_f$ is unknown, characterizing the circuit requires the introduction of a noise V_e to to be thus large that $\tilde{a}_f$ becomes negligible. Solving for V_1 this equation then yields:

$$V_1 = \frac{V_e}{1 + \frac{\alpha\beta}{M}HF} \tag{3.67}$$

And by the same method V_2 is obtained:

$$V_2 = \frac{-\frac{\alpha\beta H}{M}V_e}{1 + \frac{\alpha\beta}{M}HF} \tag{3.68}$$

Here, $\frac{\alpha\beta}{M}HF$ is recognized as the open loop response (OL). This function is determined by measuring the response of V_2/V_1, which is mathematically represented as:

$$\frac{V_2}{V_1} = -\alpha\frac{\beta}{M}H \tag{3.69}$$

And OL is obtained by multiplying this with the modelled filter function F. The magnitude and phase of the response V_2/V_1 are measured with a spectrum analyzer (Keysight 3567-A). Besides, the coherence of their signals are measured to check the cleanness of the measurement. If coherence is low it means that V_e cannot overrule noise from the environment ($\tilde{a}_f$ is not negligible anymore). The results of this experiment are displayed in Figure 3.23.

Looking at the coherence in Figure 3.23, it is clear that at some frequencies the measurement was indeed disturbed by ground vibrations, but overall the experiment is deemed clean. The response line

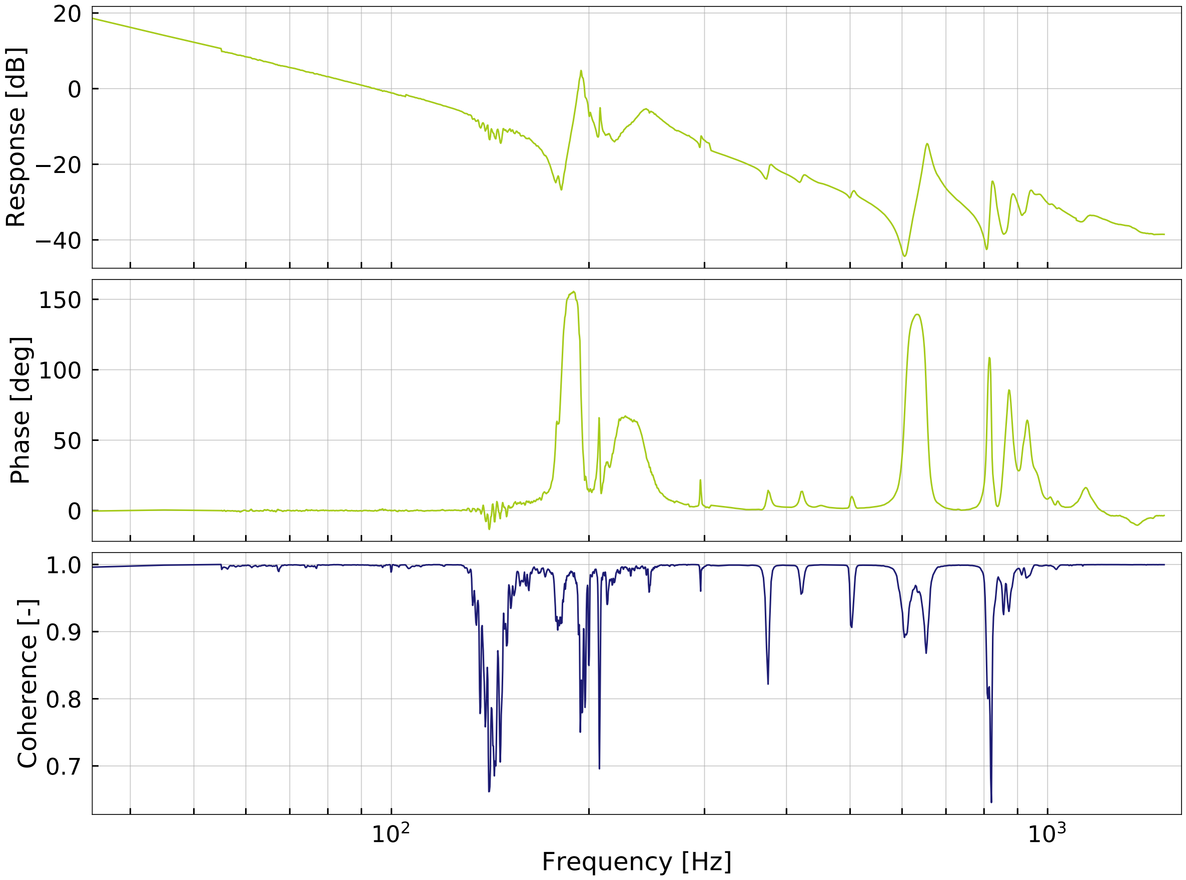

Figure 3.23: Measured mechanical response $(-\alpha \frac{\beta}{M} H)$. The wiggles around $f = 200$ Hz are a result of pendulum leg modes. The structures above $f = 500\text{-}9000$ Hz were not identified.

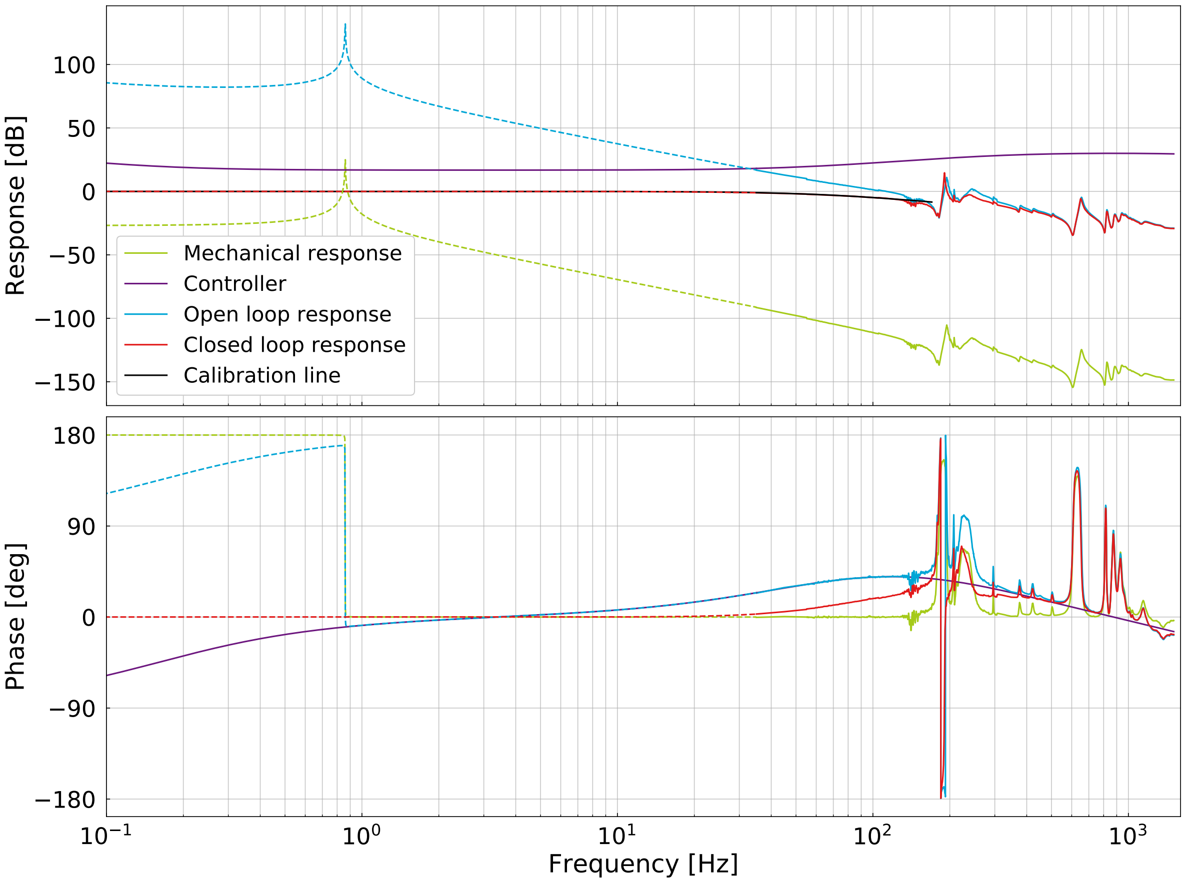

Figure 3.24: The feedback loop responses. The dashed lines are responses calculated from the modelled mechanical response. The $-\alpha\frac{\beta}{M}H$ response was measured with the old experimental setup, so the solid light green line was matched to the model in order to obtain H for higher frequencies. The solid black curve is a low-pass filter fit to the accelerometer response (see Equation (3.72)), required for correction of measured data.

exhibits the expected $1/f^2$ decay. Due to internal pendulum modes of the accelerometer suspension legs, wiggles are shown at $f = 200$ Hz. In this respect the accelerometer mechanics have improved compared with previous experiments, where the heavier pendulum legs produced frequency disturbances already at $f = 100$ Hz [2].

Having measured the mechanical response, the open loop response of the system is derived as:

$$\mathrm{OL} = \alpha\frac{\beta}{M}HF \tag{3.70}$$

And the closed loop response is given as:

$$\mathrm{CL} = \frac{\mathrm{OL}}{1+\mathrm{OL}} \tag{3.71}$$

The feedback system is now completely characterized. The results of the measurement of the mechanical response, the modelled controller, and the OL and CL responses are depicted in Figure 3.24. The estimated parameters of the circuit are displayed in Table 3.9.

Calibration To obtain displacement noise from accelerometer voltage output, its [V/$\sqrt{\mathrm{Hz}}$] signals were calibrated through division with the frequency dependent function $C(f)$:

$$C(f) = \frac{M}{\beta}\frac{f_c}{\sqrt{f_c^2+f^2}} \tag{3.72}$$

Table 3.9: Estimated properties of the feedback loop.

Parameter	Symbol	Value
Interferometer response	Γ	$3.1 \cdot 10^{7}$ V/m
feedback actuator response	β	$1.0 \cdot 10^{-3}$ N/V
Effective proof mass	M	0.76 kg
Unity gain frequency	UGF	110 Hz
Phase margin	ϕ_{UGF}	$37°$
Bandwidth	Δf	150 Hz

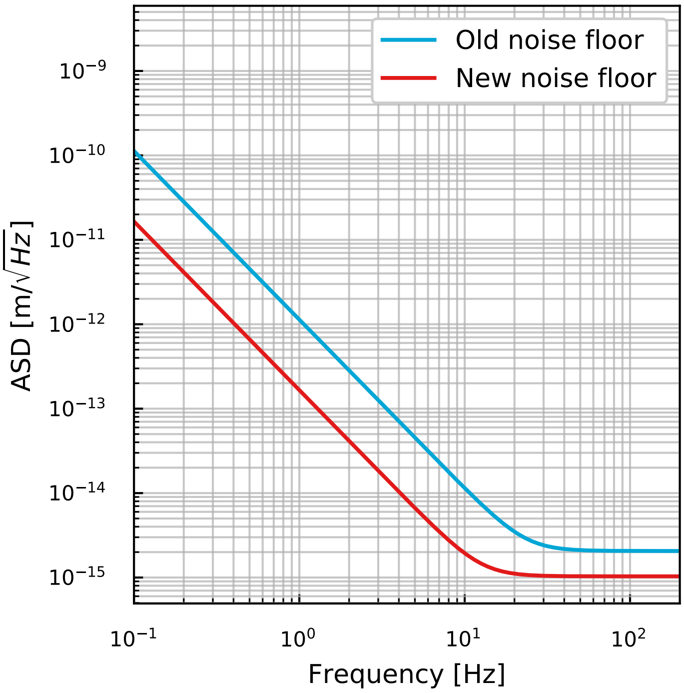

Figure 3.25: Theoretical perforamance improvement of the accelerometer due to the novel feedback actuator (thermal noise, below 10 Hz) and new PM fiber setup (shot noise, above 10 Hz).

where the low-pass term is obtained from the fit to CL in Figure 3.24, with parameter $f_c = 70$. The calibration factor $\frac{M}{\beta}$ is 760 V/(ms^{-2}). The function $C(f)$ is in [V/m].

3.5.2. Sensitivity curves

The monolithic FP accelerometer saw two improvements during this research, due to which the noise limits of thermal noise and shot noise were lowered. The theoretical improvements due to the new feedback actuator and new PM fiber setup are depicted in Figure 3.25.

At the low-noise optical bench at Nikhef, noise measurements were done for different coherence levels between accelerometer signal and the input laser signal (see Figure 3.21). For this, the time-coherence data was recorded for a few days and subsequently scanned for periods of high and low coherence (ares of red and blue in Figure 3.21). As the low coherence period lasted for only a few minutes, this noise spectrum was taken from shorter time samples, reducing resolution at low frequencies. A coinciding measurement of the adjacent, calibrated geophone is plotted as well for reference. Observing $f = 1.6$ Hz resonance peak heigths, as measured by the accelerometer and the pre-calibrated geophone that was situated close to and parallel with the accelerometer, the modelled voltage-to-displacement calibration factor was determined to be correct. Results of the final sensitivity measurements are displayed in Figure 3.26. A picture of the accelerometer in feedback setup is displayed in Figure 3.27.

Firstly, it is obvious that the thermal noise limit was not reached by far. The not fully-filtered low frequency seismic noise of the bench suspension is too high for the thermal noise to reveal itself. Detecting

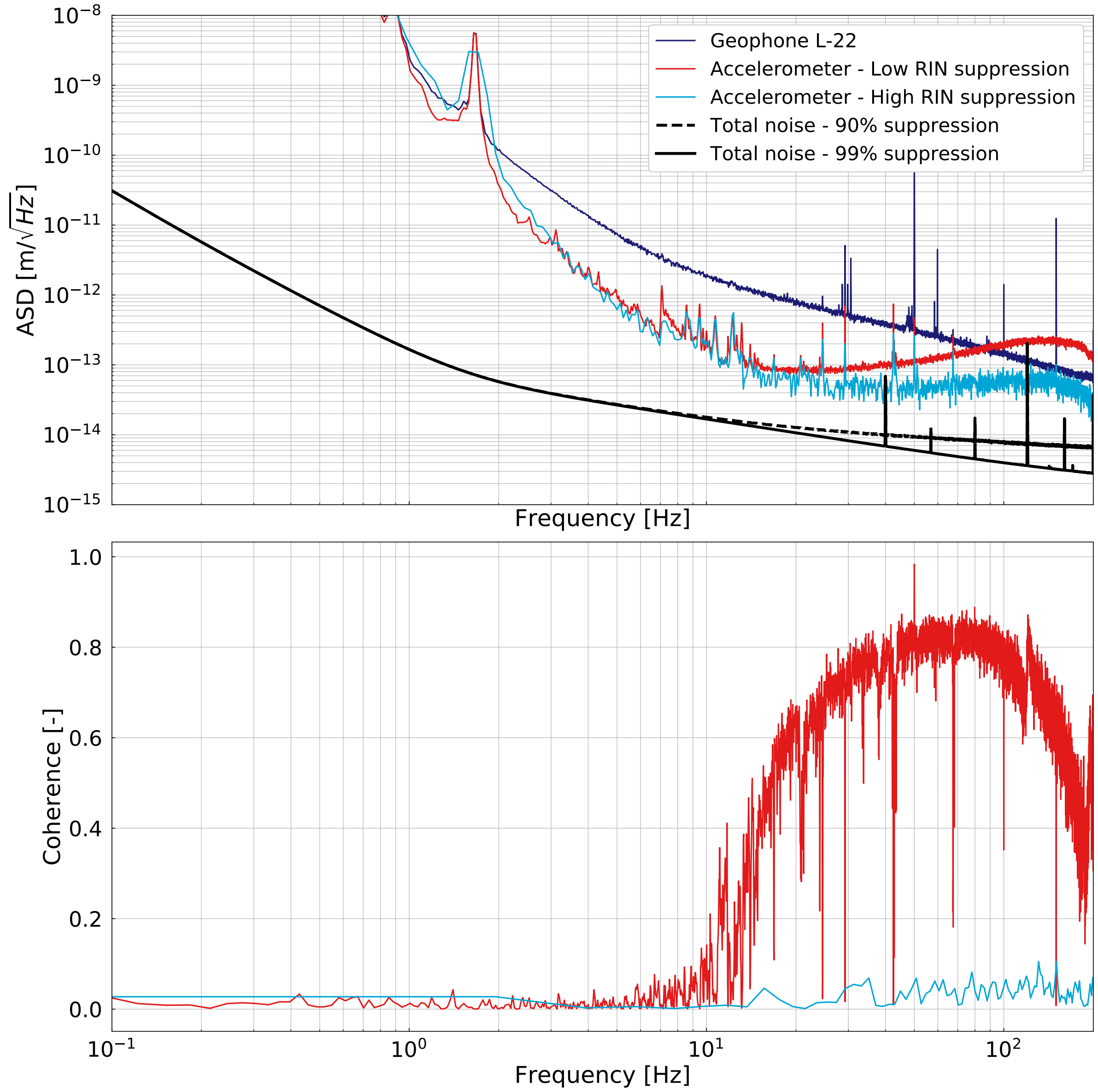

Figure 3.26: Noise measurement at the low-noise test bench, for two levels of RIN suppression.

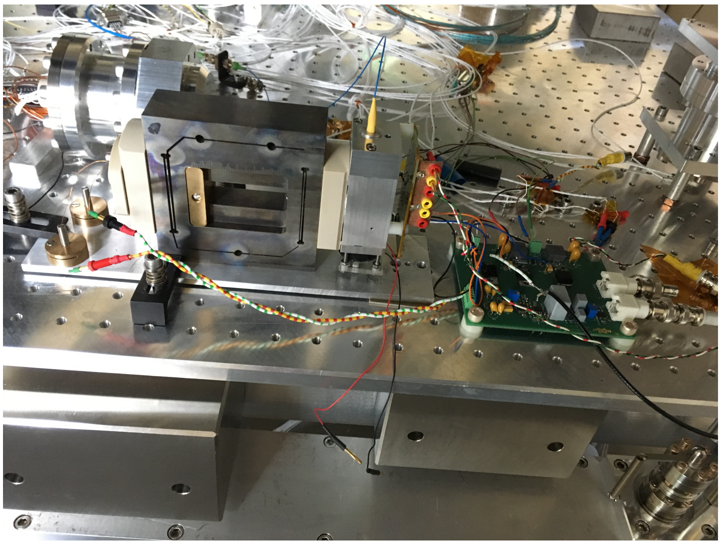

Figure 3.27: Sideview on the titanium accelerometer operated in feedback loop at the ultra-low noise test bench. The novel feedback actuator is mounted on the left side of the accelerometer, force-balancing the proof mass. Right, the interferometeric readout is attached, with the laser fiber entering from above. The PID board, with the interferometer signal as input and the feedback actuator signal as output, is situated next to the interferometer. On the left, behind the accelerometer, one sees the aligned geophone for reference measurements.

thermal noise for the monolithic FP accelerometer would require an ultra-low noise test bench at low frequencies, which presumably does not exist.

Secondly, it is seen that the shot noise floor of a few fm/$\sqrt{\mathrm{Hz}}$ was not reached, as expected. However, the modelled laser frequency noise floor of around 10^{-14} m/$\sqrt{\mathrm{Hz}}$ was also not measured. The low RIN suppresion measurement, presented in red, reached a noise floor of 90 fm/$\sqrt{\mathrm{Hz}}$ and increasing from 20 Hz, and the high RIN suppresion measurement reached displacement noise of 50 fm/$\sqrt{\mathrm{Hz}}$. This difference between the displacement noise measurements indicates that RIN is limiting the performance of the accelerometer at this level of sensitivity. The level or RIN suppression cannot be retrieved exactly from the displacement noise measurements and it might be that, although coherence was low, the accelerometer's sensitivity was still partly limited by RIN in the interferometer. The two modelled total noise scenarios plotted in black, for 90% and 99% RIN suppression, were expected to be of similar levels as the measured noises. Therefore, it seems that an unknown effect remains present in this setup, and this requires further investigation. The measured displacement sensitivity of 50 fm/$\sqrt{\mathrm{Hz}}$ is an approximately flat line above $f = 20$ Hz, indicating the remaining noise originates from the laser interferometer.

The 50 fm/$\sqrt{\mathrm{Hz}}$ measured noise floor is a factor 6 higher than the 8 fm/$\sqrt{\mathrm{Hz}}$ obtained in previous research with the same instrument [2]. This discrepancy could be explained by the fact that the static arm length difference of this interferometer was larger than 3 mm, about a factor 3 more than in the previous experiment, introducing a significant amount of laser frequency nosie. What is more, the 8 fm/$\sqrt{\mathrm{Hz}}$ noise floor was obtained with a laser fiber length of about 2 m inside a temperature controlled environment, whereas this setup, with a > 10 m laser link, was heavily exposed to beam polarization angle drifting as a result of thermal variations in the lab. Replacing the non-PM laser fibers with PM fibers was not sufficient to gain control of the polarization drifts.

3.6. Conclusions

A sizeable part of this research consisted of mapping the mechanics of the monolithic FP accelerometer with quality factor measurements, and improving Q by modelling and creating a novel feedback actuator design, after having established that Q was being deteriorated by the old feedback actuator. Then, the accelerometer's performance in closed loop was mapped. After a noise budget was assembled, and it was concluded that non-cancelled RIN was limiting, non-PM fibers in the setup were replaced with PM fibers. Lastly, the open and closed loop performance as a result of the PID were charachterizedl.

Thermal noise was improved from Q = 58 to Q = 2715 due to a novel feedback actuator design that discarded lead wires to the proof mass. The force per magnet-coil distance was modelled and optimized for this new feedback actuator, and it was measured that the model was in correspondance with experiment. Thermal displacement noise could not be measured, as it was well below the non-filtered seismic noise at LF of the optical test bench.

The shot noise floor of 1.4 fm/$\sqrt{\mathrm{Hz}}$ could not be reached. An optimal level of 50 fm/$\sqrt{\mathrm{Hz}}$ was reached, via a detour of scanning datasets of a few days long for time periods of low coherence between the accelerometer signal and the input laser. From this, it was concluded that thermally induced polarization angle drifting of the input beam was a limiting factor. Moreover, laser frequency noise due to a too large static arm length difference of $\Delta L_0 = 3$ mm was a main limiting factor. In fact, the difference between model and measurement of the previous experiment by Heijningen [2], which was a central question when starting this research, could be well explained by the laser frequency noise modelled too optimistically. Finally, the mismatch between measured noise levels and modelled RIN spectra is is unclear, and this should be investigated further.

The monolithic FP accelerometer with a double-arm interferometer as readout has the potential to be thermal noise limited below 10 Hz (with $1.6 \cdot 10^{-13} f^{-2}$ m Hz^{-2}/$\sqrt{\mathrm{Hz}}$) and shot noise limited above 10 Hz (with 1.4 fm/$\sqrt{\mathrm{Hz}}$). It might be that an accelerometer with low ΔL_0 would function properly on LIGO and Virgo test mass suspensions, as they are in temperature controlled environments, but R&D on the prototype is not possible there. In fact, globally, the only ultra-low noise optical bench research facility is the one at Nikhef used for this research. Therefore, it is adviced to

1. Create a more robust mechanical design of the interferometer with a arm lenth difference of $\Delta L_0 < 0.5$ mm. The redesigned mechanics should also allow for more effortless mirror alignment.
2. Use a laser directly placed on top of the interferometer, without optical fibers. In this way, thermally induced polarization angle drifting cannot occur. The quality of the laser will not be as high though as the one used in this research, presumably resulting in a higher frequency noise.

4

Conclusions and recommendations

Rasnik as displacement sensor The Rasnik system is measured to have a resolution of about 270 pm/$\sqrt{\mathrm{Hz}}$ above 1 Hz with nm scale deviations from linearity. With more advanced CCD pixel image sensors, resolutions of below 100 pm/$\sqrt{\mathrm{Hz}}$ are not an unrealistic prospect. The posibility to further improve the resolution with high-magnification microscopic objectives indicate a pm/$\sqrt{\mathrm{Hz}}$ noise floor should be achievable. Already with the highly linear and 270 pm/$\sqrt{\mathrm{Hz}}$ resolution Rasnik is more precise than currently employed displacement sensors in GW experiments.

With a sub nm resolution, Rasnik is comparable in performance to the OSEM, but it has the high dynamic range as advantage. With respect to the Optical Levers, the current 270 pm/$\sqrt{\mathrm{Hz}}$ resolution Rasnik would be an improvement of more than an order of magnitude, and adding it's large dynamic range makes it specifically highly attractive. Then, Rasnik with pm/$\sqrt{\mathrm{Hz}}$ resolution is deemed very suitable for the readout of a seismic tiltmeter, being much less complex than the interferometer readouts suggested in other research [44].

Therefore, it is recommended that a Rasnik with high-performance CCD cam will be developed, and enhanced with the replacement of a strong microscopic objective for the lens. When resolution is improved drastically, promising applications for displacement sensors should be developed, which will be highly competitive in cost and performance with respect to current relative position sensors for alignment and control in GW experiments.

The monolithic FP accelerometer as inertial sensor Due to improvements made in this research, the monolithic FP accelerometer saw its theoretical performance increase to a $1.6{\cdot}10^{-13}f^{-2}$ m Hz^{-2}/$\sqrt{\mathrm{Hz}}$ thermal noise limit below 10 Hz, and to a $1.4 \cdot 10^{-15}$ m/$\sqrt{\mathrm{Hz}}$ shot noise limit above 10 Hz. However, theoretical noise performances were not revealed in this research. Thermal noise is below the LF noise of the ultra-low vibration isolation platform at Nikhef. Shot noise was not reached due to laser frequency noise from a too large static arm length difference of the interferometer, and due to non-optimal RIN cancellation, and possibly due to other noise sources. A noise floor of 50 fm/$\sqrt{\mathrm{Hz}}$ was measured, a factor 30 above the modelled shot noise.

As the monolithic FP accelerometer has the potential to be orders of magnitude more sensitive than the best performing geophones, it is suggested to continue research, but with a more stable setup. Therefore, it is suggested to replace the laser fiber setup to the interferometer with a laser placed directly on the interferometer, bypassing all fibers in which thermal polarity angle drifting could occur. The mechanics facilitating Gray's double-arm interferometer should be redesigned to a more robust system with arm length difference $\Delta L_0 < 0.5$ mm that also allows for effortless alignment. The setback of such a setup would be a reduced laser quality.

A

Pixel intensity, pixel noise and the Cramér-Rao Lower Bound analysis

```
import imageio
import glob
import numpy as np
import matplotlib.pyplot as plt

def load_images(path):
    ''' Load a list of images from a specified directory (path). '''

    ''' Input: the directory path in which the images are located. '''
    ''' Output: an array of the sequence of images. '''

    image_list = []
    for im_path in glob.glob(path):
        im = imageio.imread(im_path)
        image_list.append(im)
    image_array = np.asarray(image_list)

    return image_array

def plot_image(image, pixel1, pixel2):
    ''' Plot an image with two annotated pixels. '''

    ''' Input: an image and two pixel locations [x,y]. '''
    ''' Output: plotted RasNik image. '''

    fig = plt.figure(figsize=(4,4))
    ax = fig.add_axes([0,0,1,1])
    cmap = plt.cm.gray
    norm = plt.Normalize(vmin=image.min(), vmax=image.max())
    image_norm = cmap(norm(image))
    ax.imshow(image_norm)
    ax.plot(pixel1[0],pixel1[1],marker='o',markersize=5,color='r')
    ax.plot(pixel2[0],pixel2[1],marker='o',markersize=5,color='r')
    ax.annotate('Pixel1', (pixel1[0],pixel1[1]), (pixel1[0]-40, pixel1[1]-20),\
                fontsize=label4x4+3, weight='bold',color='r')
    ax.annotate('Pixel2', (pixel2[0],pixel2[1]), (pixel2[0]-40, pixel2[1]-20),\
                fontsize=label4x4+3, weight='bold',color='r')
```

```
    ax.set_xlabel("x pixel", fontsize=label4x4)
    ax.set_ylabel("y pixel", fontsize=label4x4)
    ax.tick_params(labelsize=tick4x4)
    print('Pixel1 value = ', image[pixel1[0],pixel1[1]])
    print('Pixel2 value = ', image[pixel2[0],pixel2[1]])
    plt.show()

    return

def pixel_noise(image_list,pixel):
    ''' Calculate pixel intensity and noise at a specified pixel location. '''

    ''' Input: a sequence of images, and the pixel location in [x,y]. '''
    ''' Output: the pixel intensity and pixel noise at the pixel [x,y]. '''

    y_pix = pixel[1]
    x_pix = pixel[0]
    I_pixel_list = []
    for i in range(len(image_list)):
        im = image_list[i]
        I_pixel_list.append(im[y_pix,x_pix])
    sigma = np.std(I_pixel_list)
    mu = np.average(I_pixel_list)

    return mu, sigma

def CRLB(image_array, d_pix= 9.6 * 10**(-6)):
    ''' Calculate the Cramer-Rao lower bound for a sequence of RasNik images. The
    mean intensity value of each image is taken to calculate the overall pixel
    noise from.'''

    ''' Input: a sequence of RasNik images. Pixel size default is 9.6 mum. '''
    ''' Output: CRLB in x and y in [m]. '''

    mean_pixel_value_array = np.mean(image_array,axis=(1,2))
    sigma_mean = np.std(mean_pixel_value_array)
    mean_image_array = np.mean(image_array, axis=0)
    image = mean_image_array

    I1 = np.gradient(image, d_pix)
    I1_x = I1[1]
    I1_y = I1[0]

    Sum_Ix_sq = (I1_x**2).sum()
    Sum_Iy_sq = (I1_y**2).sum()

    plot_image(mean_image_array, pixel1,pixel2, save_fig=False)
    Cross_term = (I1_x*I1_y).sum()**2
    det_T = (Sum_Ix_sq*Sum_Iy_sq - Cross_term)

    var_vx = (sigma_mean**2*Sum_Iy_sq)/det_T
    var_vy = (sigma_mean**2*Sum_Ix_sq)/det_T

    sigma_CRLB_x = np.sqrt(var_vx)
    sigma_CRLB_y = np.sqrt(var_vy)
```

```
    return sigma_CRLB_x,sigma_CRLB_y

''' Pixels used for calculations '''
x1 = 432−10
y1 = 276 +35
x2 = 170 −10
y2 = 276 +35
pixel1= [x1,y1] # Binning = 1
pixel2= [x2,y2]
pixel1 = [int(x1/2),int(y1/2)] # Binning = 2
pixel2 = [int(x2/2),int(y2/2)]

'''Figure fontsizes and colors '''
label4x4 = 10
legend4x4 = 8
tick4x4 = 8
colors = {"Black":"#000000","Red":"#E21A1A","Cyan":"#00A6D6","BrightGreen":"#A5CA1A",\
          "Purple":"#1D1C73","Yellow":"#E1C400","SkyBlue":"#6EBBD5",\
          "WarmPurple":"#6D177F","Orange":"#E64616","Green":"#008891",\
          "GreyGreen":"#6B8689"}
```

B

RasNik data acquisition and analysis

```python
import scipy as sp
import numpy as np
import pandas as pd
from scipy import signal
from numpy import loadtxt
from datetime import datetime


def ReadDataEfficient(datafile):
    ''' Load RasNik measurement data in a memory efficient way. Without the time data
    of the first column. '''

    ''' Input: the directory path of the datafile. '''
    ''' Output: RasNik response array (4,N), and the length of the array N. '''

    data = loadtxt(datafile,usecols = (2,3,4,5), delimiter=”;”,unpack=False)
    size = int(data[:,0].size)

    return data,size

def ReadDataWithTime(datafile):
    ''' Load a RasNik measurement in a memory inefficient way, but with time data
    included and converted to a datetime list. '''

    ''' Input: the directory path of the datafile. '''
    ''' Output: RasNik datetime list, RasNik responses array (4,N), the length
    of measurement points N. '''

    dataimport =            pd.read_csv(datafile, header=None)
    dataimport.columns =    ['A']
    dataimport =            dataimport[~dataimport['A'].astype(str).str.startswith('/')]
    dataimport =            dataimport[~dataimport['A'].astype(str).str.startswith('C')]
    dataimport =            np.array(dataimport)

    N =                     dataimport.size
    y =                     np.zeros(6)
    datelist =              [None] * N
    timelist =              [None] * N
    date_and_time =         [None] * N
```

```
    for i in range(N):
        x = dataimport[i,0].split(';')
        x = np.asarray(x)
        y = np.vstack((y,x))
        datelist[i] = datetime.strptime(x[0], '%d/%m/%Y')
        timelist[i] = datetime.strptime(x[1], '%H:%M:%S.%f')
        timelist[i] = timelist[i].time()
        date_and_time[i] = datetime.combine(datelist[i],timelist[i])

    dataimport = np.delete(y,0,0)
    data = dataimport[:,2:5].astype(float)

    return date_and_time, data, N

def FourierTransform(sample_data, fs, Npersegments,i_noisefloor):
    ''' Calculate the FFT from a RasNik measurement using Welch's method.'''

    ''' Input: RasNik data array (1D), sampling frequency fs [Hz], length of the
    segments over which is averaged, cutoff index from which to calculate
    the noise floor An'''
    ''' Output: an array of (Detrended RasNik data, frequencies,
    calculated An per f). The noise floor A_n as calculated from values above
    index i_noisefloor. The RMS as integrated ASD over all frequencies, which
    should be the same as the stdev from the time data sample.'''

    Noverlap = Npersegments/2
    detrend_data = signal.detrend(sample_data)
    f, PSD = sp.signal.welch(detrend_data,fs,nperseg=Npersegments,noverlap=Noverlap)
    ASD = np.sqrt(PSD)
    RMS = np.sqrt(np.trapz(abs(ASD)**2,x=f))
    i_noisefloor=50
    An = np.mean(ASD[i_noisefloor:-1])

    return np.asarray((detrend_data,f,ASD)),An,RMS
```

C

Accelerometer Q-factor data acquisition and analysis

```
import numpy as np
import matplotlib.pyplot as plt
import scipy
from scipy import fftpack
import pandas as pd

def data_import(data):
    ''' Load Q-factor data from DataDisplay. '''

    ''' Input: the directory path of the datafile. '''
    ''' Output: time data x in [s], measurement data y in [V],
    the name allocated to the measurement - data. '''
    measurement = pd.read_csv(data, sep = '□', header = None)
    measurement = np.asarray(measurement)
    y = measurement[:,2]
    y = np.trim_zeros(y)
    x = np.linspace(0,y.size/100,y.size)
    return x, y, data

def amplitude_exponent(time, A, tau):
    '''The fit function for the exponential decay of the signal amplitude'''
    return A * np.exp(-time/tau)

def damped_sine(time, A, tau, omega_0, phi):
    '''The fit function for the damped sine wave signal'''
    return A * np.exp(-time/tau) * np.sin(omega_0 * time + phi)

def select_fit_plot(y, name, A_guess, tau_guess, phi_guess, begin=0, end=-1, f_s=100,\
                    f_0_acc=0.86):
    '''Q is calculated with this function, by first selecting manually a range of
    datapoints and second to perform fits from two functions over this data'''

    '''Input: y data in [V], guess amplitude A_guess in [V], guess decay time
    tau_guess in [s], guess phase in [rad], manually set begin datapoint,
    manually set eind datapoint, sampling rate f_s in [Hz], natural frequency of the
    accelerometer f_0_acc in [Hz]'''
    '''Output: Q1 and Q2 as [Value,Error]'''
```

```
’’’Calculate the natural frequency of the input signal’’’
X = fftpack.fft(y)
X = np.delete(X,0)
freqs = fftpack.fftfreq(len(y))*f_s
f_0 = freqs[abs(X).argmax()]
omega_0 = 2*np.pi*f_0

’’’Center the data around zero’’’
y = y[begin:end]
mean_y = np.mean(y)
y = y - mean_y
x = np.linspace(0,y.size/f_s,y.size)

’’’’Fit exponential decay function to amplitude envelope of the data.
Calculate Q and fit error’’’
analytic_signal = scipy.signal.hilbert(y)
amplitude_envelope = np.abs(analytic_signal)
popt1, pcov1 = scipy.optimize.curve_fit(amplitude_exponent,x,amplitude_envelope)
tau1 = popt1[1]
stdev_tau1 = np.sqrt(np.diag(pcov1))[1]
Q1 = np.zeros(2)
Q1[0] = np.pi * f_0_acc * tau1
Q1[1] = Q1[0] * stdev_tau1/tau1

’’’Fit a damped sine to the data. Calculate Q and fit error’’’
guess = np.array([A_guess,tau_guess,omega_0,phi_guess])
popt2, pcov2 = scipy.optimize.curve_fit(damped_sine,x,y,guess)
tau2 = popt2[1]
stdev_tau2 = np.sqrt(np.diag(pcov2))[1]
Q2 = np.zeros(2)
Q2[0] = np.pi * f_0_acc * tau2
Q2[1] = Q1[0] * stdev_tau2/tau2

’’’Plot measurement data and two fit lines’’’
fig, ax = plt.subplots()
ax.plot(x, y, label=’Measurement’, color=colors[”Yellow”])
ax.plot(x, amplitude_exponent(x, *popt1), \
        label=’Envelope□fit,□$tau□=□%.0f$□s’%(tau1), color=colors[”Red”])
ax.plot(x, damped_sine(x,*popt2), \
        label=’Sine□fit,□$tau□=□%.0f$□s’%(tau2), color=colors[”Purple”])
ax.set_xlabel(’Time□[s]’,fontsize=labels)
ax.set_ylabel(’Signal□[V]’,fontsize=labels)
ax.set_xlim(x.min(),x.max())
ax.grid(b=True, which=’both’, axis=’both’, alpha=0.7)
ax.tick_params(direction=’in’,which=’both’, pad=10,labelsize=ticks)
ax.legend(fontsize=legend, fancybox=True, framealpha=1)
fig = plt.gcf()
fig.set_size_inches(16, 8)
fig.tight_layout()
plt.savefig(r’C:\MasterThesis\Report\fig\Accelerometer\Q_measurement{}.pdf’\
            .format(name),dpi=1000)
plt.show()

return Q1, Q2
```

D

A model to calculate $B(z,r)$ from a coil and find the optimal magnet-to-coil distance

```
import numpy as np
import matplotlib.pyplot as plt
from matplotlib.cm import coolwarm
from matplotlib.patches import Rectangle
from scipy.special import ellipe, ellipk
from scipy.integrate import dblquad, tplquad

'''Input parameters'''
mu_0 = 4*np.pi*10**(-7) # T m/A
resistivity_copper = 1.7 * 10**(-8) # Ohm m

N_coil = 506 # windings
Ri_coil = 0.0046 # m
Coil_thicknes = 0.005 # m
Ro_coil = Ri_coil + Coil_thicknes # m
R_coil = Ri_coil + Coil_thicknes/2 # m
dR = Coil_thicknes/2

L_coil = 0.006 # m
Z_coil = 0.0 # m
I_coil = -0.01 # A
t_wire = 0.0002 # m
R_wire = t_wire/2 # m

R_magnet = 0.0025 # m
L_magnet = 0.005 # m
B_rem_magnet = 1.345 # T
I_magnet = (B_rem_magnet/mu_0) * L_magnet # A - hypothetical current around magnet


'''(z,r) arrays'''
N = 200
z_min = -0.02
z_max = 0.02
r_min = 0.0001
```

```
r_max = 0.02
z_list = np.linspace(z_min,z_max,N)
r_list = np.linspace(r_min,r_max,N)
r_list = np.reshape(r_list,((-1,1)))


def B_ring(z_c, R_c, z_m, R_m, I_c):
    ''' Calculate the magnetic field from a current ring'''

    ''' Input: ring center z_c in [m], ring radius R_c in [m], cyllindrical location
    of calculated B (z_m,R_m) in [m], current through coil I_c in [A]'''
    ''' Output: B field at (z_m,R_m)'''

    A = (R_c-R_m)**2 + (z_m-z_c)**2
    B = R_c**2 + R_m**2 + (z_m-z_c)**2
    C = (R_c+R_m)**2 + (z_m-z_c)**2

    elliptic_term = (4*R_m*R_c) / C

    ellipsK = ellipk(elliptic_term)
    ellipsE = ellipe(elliptic_term)

    Term = mu_0 * I_c / (2*np.pi*R_m*A*np.sqrt(C))
    B = Term * (z_m-z_c) * (A*ellipsK - B*ellipsE)

    return B

def F_z(z_c, R_c, z_m, R_m, L_c, L_m, I_c, I_m, N_c, dR):
    ''' Calculate the integrated force from a coil on a magnet
    at location (z_m,R_m) '''

    ''' Input: same input as function B_field'''
    ''' Output: the force experienced by a magnet at (z_m,R_m) '''

    R_in = R_c - dR
    R_out = R_c + dR
    L_m_wire = 2*np.pi*R_m

    TripleIntegral = tplquad(B_ring, z_m-L_m/2, z_m+L_m/2, lambda z_m:R_in,\
                             lambda z_m:R_out, lambda z_m, R_c:-L_c/2,\
                             lambda z_m, R_c:L_c/2, args = (R_m,I_c))
    B_TripleIntegral = TripleIntegral[0] * N_c / (L_c * (R_out-R_in))
    F3 = B_TripleIntegral * (B_rem_magnet/mu_0) * L_m_wire

    return F3

def force_list(coil_to_magnet_distance):
    ''' Create arrays of forces from the coil on both magnets, and create
    the combined force array. '''

    ''' Input: the coil-to-magnet distance. '''
    ''' Output: Fmagnet1 gives an array of forces from the coil on one magnet,
    at varying positions z_m. Fmagnet2 gives the force on the other magnet
    (the distance between them is coil_to_magnet_distance*2).
    Ftotal is the combined force on the two magnets. All forces are in [N]'''
```

```
    Fmagnet1 = np.empty((N))
    Fmagnet2 = np.empty((N))

    for i in range(N):
        F_1 = F_z(0, R_coil, z_list[i], R_magnet, L_coil, L_magnet, I_coil, I_magnet,\
                  N_coil, dR)
        F_2 = F_z(0, R_coil, z_list[i] + coil_to_magnet_distance*2, R_magnet, L_coil,\
                  L_magnet, \
                  I_coil, I_magnet, N_coil, dR)
        Fmagnet1[i] = F_1
        Fmagnet2[(N-1)-i] = F_2
        Ftotal = Fmagnet1 + Fmagnet2

    return Fmagnet1, Fmagnet2, Ftotal

def find_force(z, z_list, Ftot):
    ''' Find the force at a certain location z. '''

    ''' Input: the location of interest z in [m], the list of possible magnet distances
    z_list in [m], and the total force list Ftot in [N]. '''
    ''' Output: The force F in [N] at the specified location z in [m].'''

    z_list = np.asarray(z_list)
    index = (np.abs(z_list - z)).argmin()
    F = Ftot[index]

    return F

def B_field(z_c, R_c, z_m, R_m, L_c, L_m, I_c, I_m, N_c, dR):
    ''' Calculate the integrated radial magnetic field from a coil at the
    location (z_m, R_m) '''

    ''' Input: coil center z_c in [m], coil radius R_c in [m], cyllindrical location
    of calculated B (z_m,R_m) in [m], coil and magnet length L_c and L_m in [m],
    coil and magnet current I_c and I_m in [A], # coil windings N_c and coil
    width dR from center R_c in [m] '''
    ''' Output: B field at (z_m,R_m) '''

    R_in = R_c - dR
    R_out = R_c + dR

    DoubleIntegral = dblquad(B_ring, R_in, R_out, lambda z_c:-L_c/2, lambda z_c: L_c/2,\
                             args = (z_m,R_m,I_c))
    B_DoubleIntegral = DoubleIntegral[0] * N_c / (L_c * (R_out-R_in))

    return B_DoubleIntegral

def calculate_and_plot_radBfield_fromcoil(radialBfield):
    ''' Plot the radial B field from the coil in 2D. '''

    ''' Input: The function to calculate the radial B field: B_field in [T]. '''
    ''' Output: A 2D plot and a 2D array of radial magnetic field strengths, B2 in [T].''

    B_double = np.empty((N,N))
    for i in range(N):
        for j in range(N):
```

```
            B2 = radialBfield(0, R_coil, z_list[j], r_list[i], L_coil, L_magnet,\
                              I_coil,I_magnet, N_coil, dR)
            B_double[i,j] = B2
            print(i,j)

    zz, rr = np.meshgrid(z_list*1000, r_list*1000)
    fig, ax = plt.subplots()
    s = ax.pcolor(zz, rr, B_double, cmap = coolwarm)
    cbar = plt.colorbar(s)
    cbar.set_label('$B_r$ [T]',fontsize=labels4x4)
    cbar.ax.tick_params(labelsize=tick4x4)
    ax.set_xlabel('$z$ [mm]', fontsize=labels4x4)
    ax.set_ylabel('$r$ [mm]', fontsize=labels4x4)
    AX = 15
    ax.set_xlim(-AX,AX)
    ax.set_ylim(0,2*AX)
    ax.tick_params(direction='in',which='both', labelsize=tick4x4)
    currentAxis = plt.gca()
    currentAxis.add_patch(Rectangle((-L_coil*1000/2, Ri_coil*1000),\
                                    L_coil*1000, Coil_thicknes*1000,\
                                    alpha=0.4, linewidth=2, color="k"))
    fig.set_size_inches(4,4)
    plt.show()

    return B2
```

E

Electric circuit drawings of the PID controller

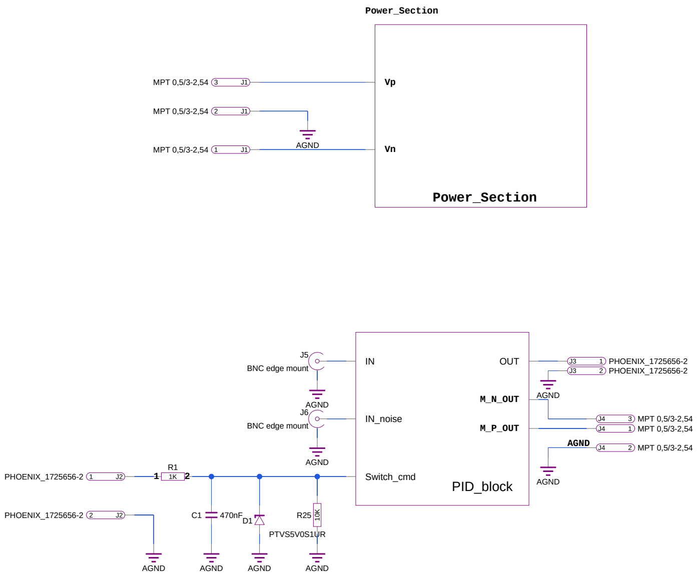

rev. by notes

PID_CONTROLLER

Project : VIRGO

Sheetname: Schematic1

45400.22.01.0

Designed by
Alessandro Bertolini

Drawn by
J.P. Fransen

Size 420 x 297mm

Sheet A3

Date 2016-07-18

Nikhef Amsterdam

Science Park 105 1098XG Amsterdam
+31-(0)20-5922000 www.nikhef.nl

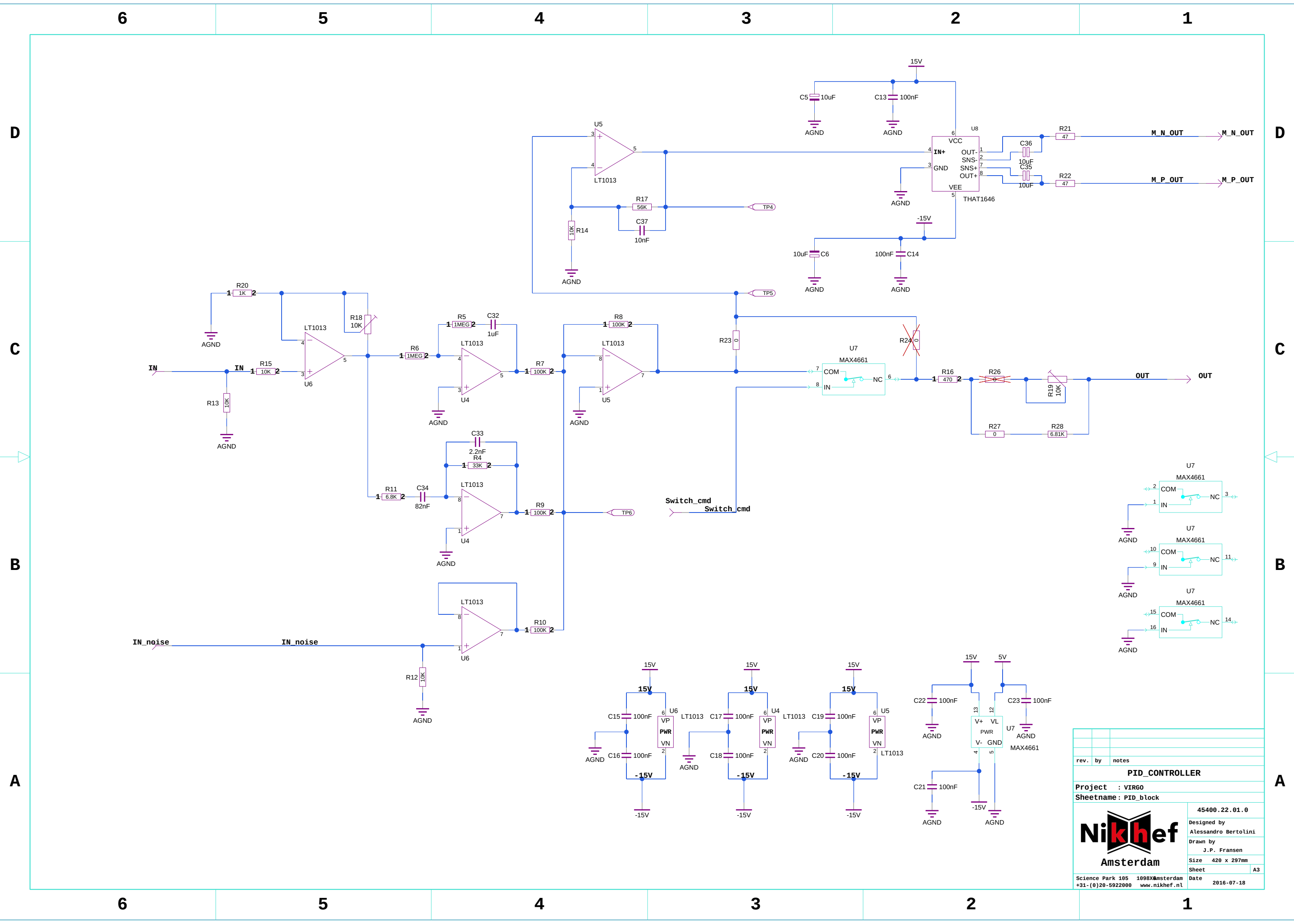

rev.	by	notes

PID_CONTROLLER

Project : VIRGO

Sheetname : PID_block

Nikhef
Amsterdam

Science Park 105 1098XG Amsterdam
+31-(0)20-5922000 www.nikhef.nl

45400.22.01.0

Designed by
Alessandro Bertolini

Drawn by
J.P. Fransen

Size 420 x 297mm

Sheet A3

Date 2016-07-18

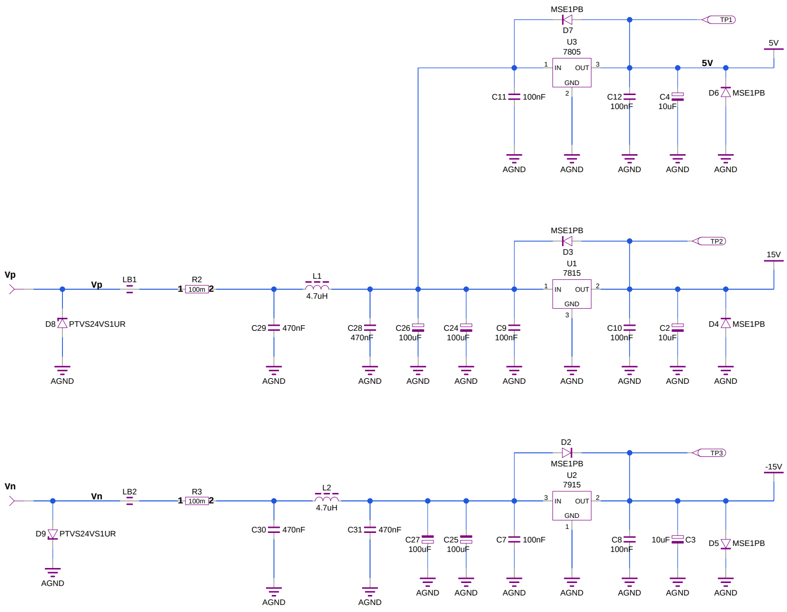

rev.	by	notes

PID_CONTROLLER

Project : VIRGO

Sheetname: Power_Section

Nikhef
Amsterdam

45400.22.01.0

Designed by
Alessandro Bertolini

Drawn by
J.P. Fransen

Size 420 x 297mm

Sheet A3

Science Park 105 1098XGAmsterdam
+31-(0)20-5922000 www.nikhef.nl

Date 2016-07-18

Bibliography

[1] M. Beker, G. Bobbink, B. Bouwens, N. Deelen, P. Duinker, J. van Eldik, N. de Gaay Fortman, R. van der Geer, Harry van der Graaf, H. Groenstege, R. Hart, K. Hashemi, J. van Heijningen, M. Kea, J. Koopstra, X. Leijtens, F. Linde, J.A. Paradiso, H. Tolsma, and M. Woudstra. The rasnik 3-point optical alignment system. *Journal of Instrumentation*, 14(08), 8 2019. ISSN 1748-0221. doi: 10.1088/1748-0221/14/08/P08010.

[2] Joris Vincent van Heijningen. *Turn up the bass! Low-frequency performance improvement of seismic attenuation systems and vibration sensors for next generation gravitational wave detectors*. PhD thesis, Vrije U., Amsterdam, 2018. URL `http://www.nikhef.nl/pub/services/biblio/theses_pdf/thesis_J_van_Heijningen.pdf`.

[3] Sir Isaac Newton. *Philosophiae Naturalis Principia Mathematica*. 1687. URL `http://cudl.lib.cam.ac.uk/view/PR-ADV-B-00039-00001/162`.

[4] A. A. Michelson and E. W. Morley. On the relative motion of the Earth and the luminiferous ether. *American Journal of Science*, 34:333–345, November 1887. doi: 10.2475/ajs.s3-34.203.333.

[5] A. Einstein. Zur elektrodynamik bewegter k orper. *Annalen der Physik*, 322(10):891–921, 1905. doi: 10.1002/andp.19053221004. URL `https://onlinelibrary.wiley.com/doi/abs/10.1002/andp.19053221004`.

[6] A. Einstein. Die grundlage der allgemeinen relativitätstheorie. *Annalen der Physik*, 354(7):769–822, 1916. doi: 10.1002/andp.19163540702. URL `https://onlinelibrary.wiley.com/doi/abs/10.1002/andp.19163540702`.

[7] A. Einstein. Über Gravitationswellen. *Sitzungsberichte der Königlich Preußischen Akademie der Wissenschaften (Berlin), Seite 154-167.*, 1918.

[8] A. Einstein. Erklärung der Perihelbewegung des Merkur aus der allgemeinen Relativitätstheorie. *Sitzungsberichte der Königlich Preußischen Akademie der Wissenschaften (Berlin), Seite 831-839.*, 1915.

[9] F. W. Dyson, A. S. Eddington, and C. Davidson. A determination of the deflection of light by the sun's gravitational field, from observations made at the total eclipse of may 29, 1919. *Philosophical Transactions of the Royal Society of London*, 220:291–333, 1920. URL `https://www.jstor.org/stable/91137`.

[10] Jorge L. Cervantes-Cota, S. Galindo-Uribarri, and G-F. Smoot. A Brief History of Gravitational Waves. *Universe*, 2(3):22, 2016. doi: 10.3390/universe2030022.

[11] J. Weber. Detection and generation of gravitational waves. *Phys. Rev.*, 117:306–313, Jan 1960. doi: 10.1103/PhysRev.117.306. URL `https://link.aps.org/doi/10.1103/PhysRev.117.306`.

[12] J. Weber. Evidence for discovery of gravitational radiation. *Phys. Rev. Lett.*, 22:1320–1324, Jun 1969. doi: 10.1103/PhysRevLett.22.1320. URL `https://link.aps.org/doi/10.1103/PhysRevLett.22.1320`.

[13] P. Astone, D. Babusci, L. Baggio, M. Bassan, M. Bignotto, M. Bonaldi, M. Camarda, P. Carelli, G. Cavallari, M. Cerdonio, A. Chincarini, E. Coccia, L. Conti, S. D'Antonio, M. De Rosa, M. di Paolo Emilio, M. Drago, F. Dubath, V. Fafone, P. Falferi, S. Foffa, P. Fortini, S. Frasca, G. Gemme, G. Giordano, G. Giusfredi, W. O. Hamilton, J. Hanson, M. Inguscio, W. W. Johnson,

N. Liguori, S. Longo, M. Maggiore, F. Marin, A. Marini, M. P. McHugh, R. Mezzena, P. Miller, Y. Minenkov, A. Mion, G. Modestino, A. Moleti, D. Nettles, A. Ortolan, G. V. Pallottino, R. Parodi, G. Piano Mortari, S. Poggi, G. A. Prodi, L. Quintieri, V. Re, A. Rocchi, F. Ronga, F. Salemi, G. Soranzo, R. Sturani, L. Taffarello, R. Terenzi, G. Torrioli, R. Vaccarone, G. Vandoni, G. Vedovato, A. Vinante, M. Visco, S. Vitale, J. Weaver, J. P. Zendri, and P. Zhang. Results of the igec-2 search for gravitational wave bursts during 2005. *Phys. Rev. D*, 76:102001, Nov 2007. doi: 10.1103/PhysRevD.76.102001. URL `https://link.aps.org/doi/10.1103/PhysRevD.76.102001`.

[14] T. Akutsu et al. KAGRA: 2.5 Generation Interferometric Gravitational Wave Detector. *Nat. Astron.*, 3(1):35–40, 2019. doi: 10.1038/s41550-018-0658-y.

[15] M Punturo, M Abernathy, F Acernese, B Allen, N Andersson, K Arun, F Barone, B Barr, M Barsuglia, M Beker, N Beveridge, S Birindelli, S Bose, L Bosi, S Braccini, C Bradaschia, T Bulik, E Calloni, G Cella, E Chassande Mottin, S Chelkowski, A Chincarini, J Clark, E Coccia, C Colacino, J Colas, A Cumming, L Cunningham, E Cuoco, S Danilishin, K Danzmann, G De Luca, R De Salvo, T Dent, R De Rosa, L Di Fiore, A Di Virgilio, M Doets, V Fafone, P Falferi, R Flaminio, J Franc, F Frasconi, A Freise, P Fulda, J Gair, G Gemme, A Gennai, A Giazotto, K Glampedakis, M Granata, H Grote, G Guidi, G Hammond, M Hannam, J Harms, D Heinert, M Hendry, I Heng, E Hennes, S Hild, J Hough, S Husa, S Huttner, G Jones, F Khalili, K Kokeyama, K Kokkotas, B Krishnan, M Lorenzini, H Luck, E Majorana, I Mandel, V Mandic, I Martin, C Michel, Y Minenkov, N Morgado, S Mosca, B Mours, H MullerEbhardt, P Murray, R Nawrodt, J Nelson, R Oshaughnessy, C D Ott, C Palomba, A Paoli, G Parguez, A Pasqualetti, R Passaquieti, D Passuello, L Pinard, R Poggiani, P Popolizio, M Prato, P Puppo, D Rabeling, P Rapagnani, J Read, T Regimbau, H Rehbein, S Reid, L Rezzolla, F Ricci, F Richard, A Rocchi, S Rowan, A Rudiger, B Sassolas, B Sathyaprakash, R Schnabel, C Schwarz, P Seidel, A Sintes, K Somiya, F Speirits, K Strain, S Strigin, P Sutton, S Tarabrin, A Thuring, J van den Brand, C van Leewen, M van Veggel, C van den Broeck, A Vecchio, J Veitch, F Vetrano, A Vicere, S Vyatchanin, B Willke, G Woan, P Wolfango, and K Yamamoto. The einstein telescope: a third-generation gravitational wave observatory. *Classical and Quantum Gravity*, 27 (19):194002, sep 2010. doi: 10.1088/0264-9381/27/19/194002.

[16] Pau Amaro-Seoane, Nils Andersson, K.G. Arun, Sukanta Bose, Leone Bosi, Tomasz Bulik, James Clark, Thomas Dent, Jonathan Gair, Kostas Glampedakis, Mark Hannam, Siong Heng, Sascha Husa, Ilya Mandel, Gareth Jones, Badri Krishnan, Ilya Mandel, Richard O'Shaughnessy, Christian Ott, Jocelyn Read, Tania Regimbau, Luciano Rezzolla, B.S. Sathyaprakash, Chris Van Den Broeck, Alberto Vecchio, and John Veitch. Einstein telescope design study: Vision document. 2009. URL `https://workarea.et?gw.eu/et/wg4?astrophysics/visdoc/`.

[17] A. Einstein. Näherungsweise Integration der Feldgleichungen der Gravitation. *Sitzungsberichte der Königlich Preußischen Akademie der Wissenschaften (Berlin), Seite 688-696.*, 1916.

[18] P.R. Saulson. *Fundamentals of Interferometric Gravitational Wave Detectors*. World Scientific, 2017. ISBN 9789813143074. URL `https://books.google.nl/books?id=5QVGDQEACAAJ`.

[19] Andrzej Krolak and Mandar Patil. The first detection of gravitational waves. *Universe*, 3:59, 07 2017. doi: 10.3390/universe3030059.

[20] Alexandre Le Tiec and Jérome Novak. Theory of Gravitational Waves. In Gerard Auger and Eric Plagnol, editors, *An Overview of Gravitational Waves: Theory, Sources and Detection*, pages 1–41. 2017. doi: 10.1142/9789813141766_0001.

[21] C. J. Moore, R. H. Cole, and C. P. L. Berry. Gravitational-wave sensitivity curves. *Class. Quant. Grav.*, 32(1):015014, 2015. doi: 10.1088/0264-9381/32/1/015014.

[22] Tania Regimbau et al. A Mock Data Challenge for the Einstein Gravitational-Wave Telescope. *Phys. Rev.*, D86:122001, 2012. doi: 10.1103/PhysRevD.86.122001.

[23] Fiodor Sorrentino. The advanced virgo interferometer. *2016 IEEE Metrology for Aerospace (MetroAeroSpace)*, pages 251–254, 2016.

[24] B. P. Abbott et al. Multi-messenger Observations of a Binary Neutron Star Merger. *Astrophys. J.*, 848(2):L12, 2017. doi: 10.3847/2041-8213/aa91c9.

[25] S. Gomez et al. A Galaxy-Targeted Search for the Optical Counterpart of the Candidate NS-BH Merger S190814bv with Magellan. 2019.

[26] J. P. W. Verbiest, L. Lentati, G. Hobbs, R. van Haasteren, P. B. Demorest, G. H. Janssen, J. B. Wang, G. Desvignes, R. N. Caballero, M. J. Keith, D. J. Champion, Z. Arzoumanian, S. Babak, C. G. Bassa, N. D. R. Bhat, A. Brazier, P. Brem, M. Burgay, S. Burke-Spolaor, S. J. Chamberlin, S. Chatterjee, B. Christy, I. Cognard, J. M. Cordes, S. Dai, T. Dolch, J. A. Ellis, R. D. Ferdman, E. Fonseca, J. R. Gair, N. E. Garver-Daniels, P. Gentile, M. E. Gonzalez, E. Graikou, L. Guillemot, J. W. T. Hessels, G. Jones, R. Karuppusamy, M. Kerr, M. Kramer, M. T. Lam, P. D. Lasky, A. Lassus, P. Lazarus, T. J. W. Lazio, K. J. Lee, L. Levin, K. Liu, R. S. Lynch, A. G. Lyne, J. Mckee, M. A. McLaughlin, S. T. McWilliams, D. R. Madison, R. N. Manchester, C. M. F. Mingarelli, D. J. Nice, S. Osłowski, N. T. Palliyaguru, T. T. Pennucci, B. B. P. Perera, D. Perrodin, A. Possenti, A. Petiteau, S. M. Ransom, D. Reardon, P. A. Rosado, S. A. Sanidas, A. Sesana, G. Shaifullah, R. M. Shannon, X. Siemens, J. Simon, R. Smits, R. Spiewak, I. H. Stairs, B. W. Stappers, D. R. Stinebring, K. Stovall, J. K. Swiggum, S. R. Taylor, G. Theureau, C. Tiburzi, L. Toomey, M. Vallisneri, W. van Straten, A. Vecchio, Y. Wang, L. Wen, X. P. You, W. W. Zhu, and X. J. Zhu. The International Pulsar Timing Array: First data release. *Montly Notices of the Royal Astronomical Society*, 458(2):1267–1288, May 2016. doi: 10.1093/mnras/stw347.

[27] Michele Punturo et al. Einstein gravitational wave telescope - conceptual design study. 2011. URL `http://www.et-gw.eu/index.php/etdsdocument`.

[28] Pau Amaro-Seoane, Heather Audley, Stanislav Babak, John Baker, Enrico Barausse, Peter Bender, Emanuele Berti, Pierre Binetruy, Michael Born, Daniele Bortoluzzi, Jordan Camp, Chiara Caprini, Vitor Cardoso, Monica Colpi, John Conklin, Neil Cornish, Curt Cutler, Karsten Danzmann, Rita Dolesi, Luigi Ferraioli, Valerio Ferroni, Ewan Fitzsimons, Jonathan Gair, Lluis Gesa Bote, Domenico Giardini, Ferran Gibert, Catia Grimani, Hubert Halloin, Gerhard Heinzel, Thomas Hertog, Martin Hewitson, Kelly Holley-Bockelmann, Daniel Hollington, Mauro Hueller, Henri Inchauspe, Philippe Jetzer, Nikos Karnesis, Christian Killow, Antoine Klein, Bill Klipstein, Natalia Korsakova, Shane L Larson, Jeffrey Livas, Ivan Lloro, Nary Man, Davor Mance, Joseph Martino, Ignacio Mateos, Kirk McKenzie, Sean T McWilliams, Cole Miller, Guido Mueller, Germano Nardini, Gijs Nelemans, Miquel Nofrarias, Antoine Petiteau, Paolo Pivato, Eric Plagnol, Ed Porter, Jens Reiche, David Robertson, Norna Robertson, Elena Rossi, Giuliana Russano, Bernard Schutz, Alberto Sesana, David Shoemaker, Jacob Slutsky, Carlos F. Sopuerta, Tim Sumner, Nicola Tamanini, Ira Thorpe, Michael Troebs, Michele Vallisneri, Alberto Vecchio, Daniele Vetrugno, Stefano Vitale, Marta Volonteri, Gudrun Wanner, Harry Ward, Peter Wass, William Weber, John Ziemer, and Peter Zweifel. Laser Interferometer Space Antenna. *arXiv e-prints*, art. arXiv:1702.00786, Feb 2017.

[29] Mitsuru Musha. Space gravitational wave detector decigo/pre-decigo. 10562, 2017. doi: 10.1117/12.2296050. URL `https://doi.org/10.1117/12.2296050`.

[30] M.G. Beker. *Low-frequency sensitivity of next generation gravitational wave detectors*. PhD thesis, Vrije Universiteit Amsterdam, 2013. Naam instelling promotie: VU Vrije Universiteit Naam instelling onderzoek: VU Vrije Universiteit.

[31] M G Beker, J F J van den Brand, E Hennes, and D S Rabeling. Newtonian noise and ambient ground motion for gravitational wave detectors. *Journal of Physics: Conference Series*, 363: 012004, jun 2012. doi: 10.1088/1742-6596/363/1/012004. URL `https://doi.org/10.1088%2F1742-6596%2F363%2F1%2F012004`.

[32] Fabrice Matichard, B. Lantz, Richard Mittleman, Kenneth Mason, J. Kissel, J. McIver, B. Abbott, R. Abbott, S. Abbott, E. Allwine, Sam Barnum, Jessica Birch, Sebastien Biscans, C. Celerier, D. Clark, Dennis Coyne, Dan Debra, R. DeRosa, Matthew Evans, and Shiping Wen. Seismic isolation of advanced ligo: Review of strategy, instrumentation and performance. *Classical and Quantum Gravity*, 32, 02 2015. doi: 10.1088/0264-9381/32/18/185003.

[33] Hareem Tariq, Akiteru Takamori, Flavio Vetrano, Chenyang Wang, Alessandro Bertolini, Giovanni Calamai, Riccardo DeSalvo, Alberto Gennai, Lee Holloway, Giovanni Losurdo, Szabolcs Marka,

Massimo Mazzoni, Federico Paoletti, Diego Passuello, Virginio Sannibale, and Ruggero Stanga. The linear variable differential transformer (lvdt) position sensor for gravitational wave interferometer low-frequency controls. *Nuclear Instruments and Methods in Physics Research Section A: Accelerators, Spectrometers, Detectors and Associated Equipment*, 489(1):570 – 576, 2002. ISSN 0168-9002. doi: https://doi.org/10.1016/S0168-9002(02)00802-1. URL `http://www.sciencedirect.com/science/article/pii/S0168900202008021`.

[34] Mark Barton. Calculation and measurement of the osem actuator sweet spot position, 2010.

[35] Joris van Heijningen. Precision improvement in optical alignment systems of linear colliders. Master's thesis, Delft University of Technology, 2011.

[36] Martin Jacob Woudstra. *Precision of the ATLAS Muon Spectrometer*. PhD thesis, Amsterdam U., 2002. URL `http://www.nikhef.nl/pub/services/biblio/theses_pdf/thesis_MJ_Woudstra.pdf`.

[37] Mark Kea. Foam: An image analysis routine for the atlas barrel muon spectrometer alignment system, 2007.

[38] Katarzyna Klemm, Krzysztof Pieszynski, and Rozniakowski Kazimierz. Examination of air density fluctuations with the aid of laser beam. *Optica Applicata*, 37, 01 2007.

[39] David X. D. Yang and Abbas El Gamal. Comparative analysis of SNR for image sensors with enhanced dynamic range. In Morley M. Blouke and George M. Williams Jr., editors, *Sensors, Cameras, and Systems for Scientific/Industrial Applications*, volume 3649, pages 197 – 211. International Society for Optics and Photonics, SPIE, 1999. doi: 10.1117/12.347075. URL `https://doi.org/10.1117/12.347075`.

[40] Tuan Q. Pham, Marijn Bezuijen, Lucas J. van Vliet, Klamer Schutte, and Cris L. Luengo Hendriks. Performance of optimal registration estimators. In *Visual Information Processing*, 2005.

[41] M.G. Beker. Rasclic, a long base, low frequency, high precision seismograph. Master's thesis, Delft University of Technology, 2008.

[42] P. Welch. The use of fast fourier transform for the estimation of power spectra: A method based on time averaging over short, modified periodograms. *IEEE Transactions on Audio and Electroacoustics*, 15(2):70–73, June 1967. doi: 10.1109/TAU.1967.1161901.

[43] Bruce H. Pillman. Impact of ccd size, pixel pitch, and anti-aliasing filter design on sharpness of digital camera print. In *PICS*, 2000.

[44] Jan Harms and Krishna Venkateswara. Newtonian-noise cancellation in large-scale interferometric GW detectors using seismic tiltmeters. *Classical and Quantum Gravity*, 33(23):234001, oct 2016. doi: 10.1088/0264-9381/33/23/234001. URL `https://doi.org/10.1088%2F0264-9381%2F33%2F23%2F234001`.

[45] Alessandro Bertolini, Riccardo DeSalvo, Francesco Fidecaro, Mario Francesconi, Szabolcs Marka, Virginio Sannibale, Duccio Simonetti, Akiteru Takamori, and Hareem Tariq. Mechanical design of a single-axis monolithic accelerometer for advanced seismic attenuation systems. *Nuclear Instruments and Methods in Physics Research Section A: Accelerators, Spectrometers, Detectors and Associated Equipment*, 556(2):616 – 623, 2006. ISSN 0168-9002. doi: https://doi.org/10.1016/j.nima.2005.10.117. URL `http://www.sciencedirect.com/science/article/pii/S0168900205020930`.

[46] David G. Blair, Jiangfeng Liu, Ehsan F. Moghaddam, and Li Ju. Performance of an ultra low-frequency folded pendulum. *Physics Letters A*, 193(3):223 – 226, 1994. ISSN 0375-9601. doi: https://doi.org/10.1016/0375-9601(94)90587-8. URL `http://www.sciencedirect.com/science/article/pii/0375960194905878`.

[47] Brian Spear. James watt: The steam engine and the commercialization of patents. *World Patent Information*, 30(1):53 – 58, 2008. ISSN 0172-2190. doi: https://doi.org/10.1016/j.wpi.2007.05.009. URL `http://www.sciencedirect.com/science/article/pii/S0172219007000932`.

[48] Fausto Acernese, Gerardo Giordano, Rocco Romano, Rosario De Rosa, and Fabrizio Barone. Mechanical monolithic horizontal sensor for low frequency seismic noise measurement. *Review of Scientific Instruments*, 79(7):074501, 2008. doi: 10.1063/1.2943415. URL `https://doi.org/10.1063/1.2943415`.

[49] Joris van Heijningen, Alessandro Bertolini, E. Hennes, Menno Beker, M Doets, Henk Bulten, K Agatsuma, and T Sekiguchi. A multistage vibration isolation system for advanced virgo suspended optical benches. *Classical and Quantum Gravity*, 02 2019. doi: 10.1088/1361-6382.

[50] Jiangfeng Liu, Li Ju, and David G. Blair. Vibration isolation performance of an ultra-low frequency folded pendulum resonator. *Physics Letters A*, 228(4):243 – 249, 1997. ISSN 0375-9601. doi: https://doi.org/10.1016/S0375-9601(97)00105-9. URL `http://www.sciencedirect.com/science/article/pii/S0375960197001059`.

[51] Timo Veijola, Heikki Kuisma, Juha Lahdenperä, and Tapani Ryh́anen. Equivalent-circuit model of the squeezed gas film in a silicon accelerometer. *Sensors and Actuators A: Physical*, 48(3):239 – 248, 1995. ISSN 0924-4247. doi: https://doi.org/10.1016/0924-4247(95)00995-7. URL `http://www.sciencedirect.com/science/article/pii/0924424795009957`.

[52] G. Cagnoli, J. Hough, D. DeBra, M. M. Fejer, E. Gustafson, S. Rowan, and V. Mitrofanov. Damping dilution factor for a pendulum in an interferometric gravitational waves detector. *Physics Letters A*, 272:39–45, July 2000. doi: 10.1016/S0375-9601(00)00411-4.

[53] C. Zener. *Elasticity and Anelasticity of Metals*. University of Chicago Press, 1948. URL `https://books.google.nl/books?id=FKcZAAAAIAAJ`.

[54] Peter R. Saulson. Thermal noise in mechanical experiments. *Phys. Rev. D*, 42:2437–2445, Oct 1990. doi: 10.1103/PhysRevD.42.2437. URL `https://link.aps.org/doi/10.1103/PhysRevD.42.2437`.

[55] Herbert B. Callen and Theodore A. Welton. Irreversibility and generalized noise. *Phys. Rev.*, 83: 34–40, Jul 1951. doi: 10.1103/PhysRev.83.34. URL `https://link.aps.org/doi/10.1103/PhysRev.83.34`.

[56] Friedrich Paschen. Ueber die zum funkenübergang in luft, wasserstoff und kohlensäure bei verschiedenen drucken erforderliche potentialdifferenz. *Annalen der Physik*, 273(5):69–96, 1889. doi: 10.1002/andp.18892730505. URL `https://onlinelibrary.wiley.com/doi/abs/10.1002/andp.18892730505`.

[57] Andrew Zangwill. *Modern electrodynamics*. Cambridge Univ. Press, Cambridge, 2013. URL `https://cds.cern.ch/record/1507229`.

[58] J. Pérez-Ríos and A. S. Sanz. How does a magnetic trap work? *American Journal of Physics*, 81 (11):836–843, Nov 2013. ISSN 1943-2909. doi: 10.1119/1.4819167. URL `http://dx.doi.org/10.1119/1.4819167`.

[59] S. I. Babic and C. Akyel. Magnetic force calculation between thin coaxial circular coils in air. *IEEE Transactions on Magnetics*, 44(4):445–452, April 2008. doi: 10.1109/TMAG.2007.915292.

[60] Mickhail E. Boulaenko. Novel tools for research and education is seismology. Master's thesis, University of Bergen, 2002.

[61] Malcolm B. Gray, David E. McCLELLAND, Mark Barton, and Seiji Kawamura. A simple high-sensitivity interferometric position sensor for test mass control on an advanced ligo interferometer. *Optical and Quantum Electronics*, 31(5):571–582, Jul 1999. ISSN 1572-817X. doi: 10.1023/A:1006991717589. URL `https://doi.org/10.1023/A:1006991717589`.

[62] Shayne Bennetts, Gordon McDonald, Kyle Hardman, John Debs, Carlos claiton Noschang kuhn, John Close, and N. Robins. External cavity diode lasers with 5khz linewidth and 200nm tuning range at 155um and methods for linewidth measurement. *Optics express*, 22:10642–10654, 05 2014. doi: 10.1364/OE.22.010642.